

**EFFECT OF SPECIMEN GEOMETRY ON ULTRASOUND
DIFFUSION IN CEMENT-BASED AGGREGATES**

A Thesis
Presented to
The Academic Faculty

by

Anandraj Sengupta

In Partial Fulfillment
of the Requirements for the Degree
Master of Science in Mechanical Engineering in the
School of MECHANICAL ENGINEERING

Georgia Institute of Technology
MAY 2008

**EFFECT OF SPECIMEN GEOMETRY ON ULTRASOUND
DIFFUSION IN CEMENT-BASED AGGREGATES**

Approved by:

Dr. Laurence Jacobs, Advisor
School of Mechanical Engineering
Georgia Institute of Technology

Dr. Jianmin Qu, Co-advisor
School of Mechanical Engineering
Georgia Institute of Technology

Dr. Reginald Desroches
School of Civil and Environmental Engineering
Georgia Institute of Technology

Date Approved: March 28, 2008

To my parents for helping me fulfill my dreams
And to my wife Deepti, for being my biggest motivator and best friend

ACKNOWLEDGEMENTS

Firstly, I wish to thank Dr.Laurence Jacobs, my advisor, and Dr.Jianmin Qu, co-advisor, for being great mentors and guides – and being nothing less than a great friend at the same time. They have been understanding and very inspiring in every manner possible, giving me the freedom to explore new and creative options for solving this problem and develop a deep appreciation of the topic through this research work.

I also wish to thank the Student Services Office, especially Ms.Glenda Johnson and Dr.Wayne Whiteman, for showing the patience to deal every single issue with promptness and smile. I am especially thankful to Ms.Johnson for her relentless and un-tiring efforts towards making life easier for all the students.

This thesis has been made possible through the generous decision of GE management to sponsor my graduate education, and I am thankful to everyone involved in the decision making process to make this happen. I also wish to thank my mentors at GE, Dr. Gopichand Katragadda, Dr.Prabha Chatterji and Dr.Vinod Kumar for helping me balance out my academic and professional lives throughout this period. My one-year transition to Atlanta has been instrumental in letting me work directly at Georgia Tech to speed up my research, as well as experience first-hand an exciting campus life. I wish to thank Mr.Steve Hartman at GE Atlanta for giving me the opportunity and making this transition happen.

At a personal level, I wish to especially thank my parents for everything they have done, and even sacrificed, to help me reach this point. It is because of the months and years of interesting talks with my dad that I have developed a deep interest towards

science and engineering, and I am glad to be still as curious and excited to explore everything that is physics and technology. I also wish to thank my mom for her endearing love that helped me develop self-confidence, and which goes a long way to empower me to take up bigger challenges in life, including this.

And most importantly, I wish to mention a special thanks to Deepti, my wife, for inspiring me, helping me with every single facet of this effort and showing constant patience throughout this journey. Without her love, support and motivation, I am sure this thesis would not have seen the light of this day.

TABLE OF CONTENTS

| | Page |
|--|----------|
| ACKNOWLEDGEMENTS..... | iv |
| LIST OF TABLES..... | xi |
| LIST OF FIGURES..... | xii |
| SUMMARY..... | xv |
| CHAPTERS | |
| 1 INTRODUCTION..... | 1 |
| 1.1 Motivation..... | 1 |
| 1.2 Nondestructive evaluation methods | 2 |
| 1.2.1 Materials | 4 |
| 1.2.2 Energy | 5 |
| 1.2.3 Signal analysis | 6 |
| 1.2.4 Emerging technologies..... | 6 |
| 1.3 Ultrasonic investigation methods..... | 8 |
| 1.3.1 Principles..... | 8 |
| 1.3.2 Energy sources | 9 |
| Signal sources and receivers | 9 |
| Important contact attributes | 10 |

| | |
|---|-----------|
| 1.3.3 Energy interaction | 11 |
| Acoustic propagation and wave modes..... | 11 |
| Energy losses | 12 |
| Acoustic impedance and flaw detection | 12 |
| Material property estimation..... | 13 |
| 1.4 Inspection of concrete infrastructure..... | 13 |
| 1.4.1 Cement-based materials | 13 |
| 1.4.2 Flaws and failure mechanisms | 15 |
| 1.4.3 Common inspection methods..... | 15 |
| 1.4.4 Summary | 19 |
| 2 LITERATURE SURVEY | 21 |
| 2.1 Introduction..... | 21 |
| 2.2 Attenuation measurements | 21 |
| 2.3 Diffuse field measurements | 23 |
| 2.4 Phase and velocity measurements | 25 |
| 2.5 Diffusion modeling..... | 26 |
| 3 THEORETICAL BACKGROUND | 29 |
| 3.1 Wave propagation..... | 29 |

| | |
|---|-----------|
| 3.1.1 Linear elasticity and equation of motion | 29 |
| 3.1.2 Wave phenomenon..... | 32 |
| 3.1.3 Reflections of P and SV-waves | 33 |
| 3.2 Attenuation | 35 |
| 3.2.1 Viscoelastic media..... | 36 |
| 3.2.2 Geometric spreading | 36 |
| 3.2.3 Scattering | 37 |
| 3.3 Short-time Fourier transformation (STFT) | 38 |
| 4 ULTRASOUND DIFFUSION APPROXIMATION | 40 |
| 4.1 Introduction..... | 40 |
| 4.2 Diffusion approximation | 41 |
| 4.3 Basic equation..... | 42 |
| 4.3.1 Definitions..... | 44 |
| 4.3.2 Identification of the coefficients | 44 |
| 4.3.3 Special solutions of the diffusion equation | 45 |
| One-dimensional bar | 46 |
| Two-dimensional plate..... | 46 |
| Circular disc of radius R | 47 |
| 4.3.4 Diffusion in infinite and finite discs | 50 |

| | |
|--|-----------|
| 4.4 Effects of Specimen Geometry on Ultrasound Diffusion | 53 |
| 5 EXPERIMENTAL PROCEDURE AND SIGNAL ANALYSIS | 55 |
| 5.1 Signal generation and amplification..... | 55 |
| 5.1.1 Function generator | 55 |
| 5.1.2 Pulse generator..... | 56 |
| 5.2 Received signal amplification..... | 56 |
| 5.3 Source/receiver selection | 57 |
| 5.4 Source/receiver configuration..... | 59 |
| 5.5 Waveform acquisition..... | 60 |
| 5.5.1 Signal-to-noise ratio (SNR) and averaging..... | 60 |
| 5.5.2 Sampling rate and record length | 61 |
| 5.6 Cement-based aggregate specimens | 62 |
| 5.6.1 Description..... | 62 |
| 5.6.2 Impedance mismatch | 63 |
| 5.6.3 Microscopic examination of the specimen | 64 |
| 6 EXPERIMENTAL RESULTS..... | 66 |
| 6.1 Introduction..... | 66 |
| 6.2 Signal processing and data analysis | 66 |

| | |
|--|-----------|
| 6.2.1 Signal pre-processing..... | 69 |
| 6.2.2 Spectral Energy Density | 70 |
| 6.2.3 Spectral energy density evolution..... | 71 |
| 6.3 Observations..... | 75 |
| 6.3.1 Model quality and comparison of fits | 76 |
| 6.3.2 Specimen averaged models..... | 79 |
| 6.3.3 Geometry and material trends..... | 89 |
| 6.4 Summary..... | 92 |
| 7 CONCLUSIONS AND OUTLOOK..... | 93 |
| REFERENCES..... | 98 |

LIST OF TABLES

| | Page |
|--|------|
| Table 1.1: A guide to selection of NDT methods for various materials and discontinuities [4] | 5 |
| Table 1.2: Typical properties of concrete material | 14 |
| Table 3.1: Angle relation for reflections on a stress-free surface | 34 |
| Table 5.1: Results of microscopic examination of the specimens | 64 |
| Table 6.1: Details of specimens used in the experiments | 67 |

LIST OF FIGURES

| | Page |
|--|----------|
| Figure 1.1: Evolving value creation with non-destructive inspection and monitoring [4]. | 1 |
| Figure 1.2: Summary of material properties of interest for non-destructive inspection [6] | 2 |
| Figure 1.3: Summary of NDE methods [6]..... | 3 |
| Figure 1.4: Schematic explanation of Probability of Detection (PoD) curve | 7 |
| Figure 1.5: Fundamental schematic of ultrasonic inspection method..... | 9 |
| Figure 1.6: Typical cross-section of concrete, illustrating the distribution of both coarse and fine aggregates [18]..... | 14 |
| Figure 1.7: Cracked mortar specimen [2] | 16 |
| Figure 2.1: Peak energy time difference across the crack and at un-cracked region..... (Lag time) vs crack-depth for a separation distance of 6 cm..... | 24 24 |
| Figure 2.2: Elastic diffusivity as a function of frequency in concrete specimens, solid line indicates theoretical estimate and symbols correspond to experimental data..... | 25 |
| Figure 3.1 Wave reflections | 33 |
| Figure 4.1: Cylindrical coordinate system and boundary conditions on circular disc..... | 48 |
| Figure 4.2: Curve fit for 3mm loose specimen with expected deviation as bars [2] | 50 |
| Figure 4.3: Predicted and observed variation of spectral energy density with time..... | 51 |
| Figure 4.4: Theoretical plot showing the higher residual energy in a finite disc, as compared to an infinite plate of same negligible thickness | 51 |
| Figure 4.5: Theoretical estimate of decay of spectral energy density with time | 52 |

Figure 4.6: Comparative estimates of spectral energy density at $t=5 \times 10^{-6}$ s (left) and at $t=30 \times 10^{-6}$ s (right) for assumed value of R (Infinite disc – red. Finite disc – blue)..... 52

Figure 4.7: Theoretical estimate of decay of $\ln \langle E(r, t, z) \rangle$ with time for infinite disc (red) and semi-infinite disc (blue) 52

Figure 4.8: Theoretical estimate of residual spectral energy density at near steady-state time ($t=5 \times 10^{-2}$ s) vs. radius of disc..... 53

Figure 5.1: Experimental setup design by Becker et al [2]..... 59

Figure 5.2: Matrix/bead interface cracks in 3 mm dense specimen..... 65

Figure 5.3: Surface cracks in 1 mm medium specimen 65

Figure 6.1: Number of waveforms analyzed for various specimens 67

Figure 6.2: Typical response waveform – raw and cropped (1 mm dense specimen)..... 68

Figure 6.3 (a) to (f): Spectral energy density (green dots) and diffusion approximation fits using finite (blue line) and infinite (red line) disc approximations for 1mm dense specimen at various frequencies. 71

Figure 6.4: Summary of diffusion approximation fits with finite disc approximation for 1mm dense specimen 75

Figure 6.5: (a) Initial and extended diffusion periods schematically shown on waveform with (b) associated spectral energy density fit showing change in slope during transition 78

Figure 6.6: Plots showing comparative dissipation curve fits for specimens with different levels of damage. Plots (a) to (f) are for cement paste and 1 mm bead specimens. Plots (g) to (l) are for cement paste and 3 mm bead specimens. Plots (m) to (r) are for cement paste, 1mm and 3mm bead specimens shown together. 80

| | |
|--|----|
| Figure 6.7: 3mm dense plot graphically depicting $t_{\overline{E}_{\min \sigma}}$ | 90 |
| Figure 6.8: 1mm dense plot showing similarity in behavior | 90 |
| Figure 6.9: Plot showing variation of $\overline{E(f)_{\min}}$ with specimen thickness | 91 |
| Figure 6.10: Plot showing time to reach energy minima against volume fraction | 91 |
| Figure 7.1: Scatter plot showing variation of energy minima | 95 |
| Figure 7.2: Scatter plot showing time to reach energy minima | 95 |
| Figure 7.3: Scatter plot showing energy value at lowest variation zone | 96 |
| Figure 7.4: Scatter plot showing time to reach energy point to tightest scatter..... | 96 |

SUMMARY

Following Carslaw [1] and as discussed by Becker et al [2, 3], the diffusion of ultrasonic energy in cement-based aggregates follow the heat diffusion equation. However, due to the finite size of the discs used in experiments by Becker, ultrasound energy is contained within the body for a longer period of time, as compared to [2]. Though the energy content of the disc in reality would eventually decay to zero, due to leaks and other mechanisms, a theoretical study of perfectly adiabatic case is useful to compare the residual energy values to material properties. As a particular example, the input energy sees multiple phenomena inside the material during propagation. The residual energy is this a combined effect of the multiple scattering, dissipative and diffusive processes.

This objective of this thesis is to study the relationship between the residual spectral density and specimen geometry. The effort further aims to attribute the difference in the residual spectral energy density values in materials of similar geometry to the varying material properties of the heterogeneous materials. Finally, a study of the error propagation in the estimation is presented, along-with an analytical relationship showing the value of spectral energy density for discs of finite radius and height.

CHAPTER 1

INTRODUCTION

1.1 Motivation

The enormous scale of infrastructural development that supports our everyday life measures much of our world's technological progress and economic advancement. It is thus very critical to maintain such infrastructure in good health, for reasons of public safety and beyond. While it is impossible to regularly disassemble airplanes and bridges for inspection, nondestructive testing (NDT) methods provide easier and practical means to achieve the same. Especially, as the infrastructure ages and becomes more prone to damages and flaws, easy, informative and accurate inspection methods gain much prominence to solve these problems through preventive and predictive maintenance (figure 1.1).

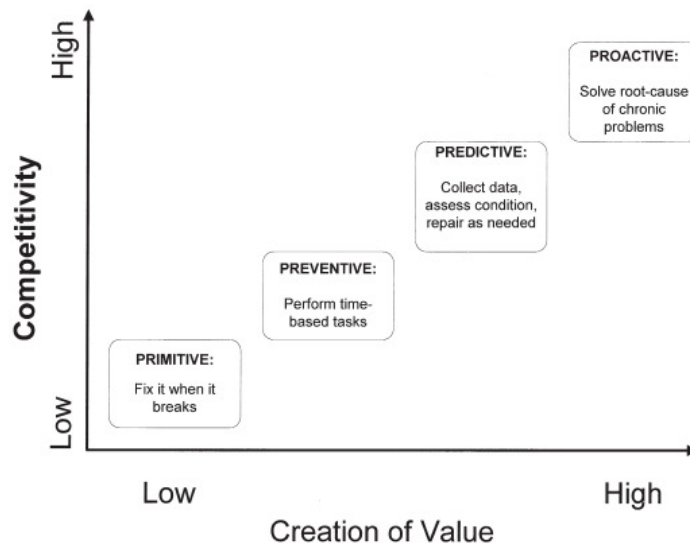


Figure 1.1: Evolving value creation with non-destructive inspection and monitoring [4]

1.2 Nondestructive evaluation methods

In today's world, there exists a plethora of nondestructive testing methods and it is very easy to get lost in their maze. This section aims to provide a perspective on the fundamental physical foundation of such methods. In the most basic form, NDT refers to “the determination of the physical condition of an object without affecting that object's ability to fulfill its intended function. NDT techniques typically use a probing energy form to determine material properties or to indicate the presence of material discontinuities (surface, internal or concealed)” [5]. It is thus the interrogation of materials with energy; such as to understand the changing properties or behavior of the material, thereby infer important information about the health of the overall system or sub-system in question.

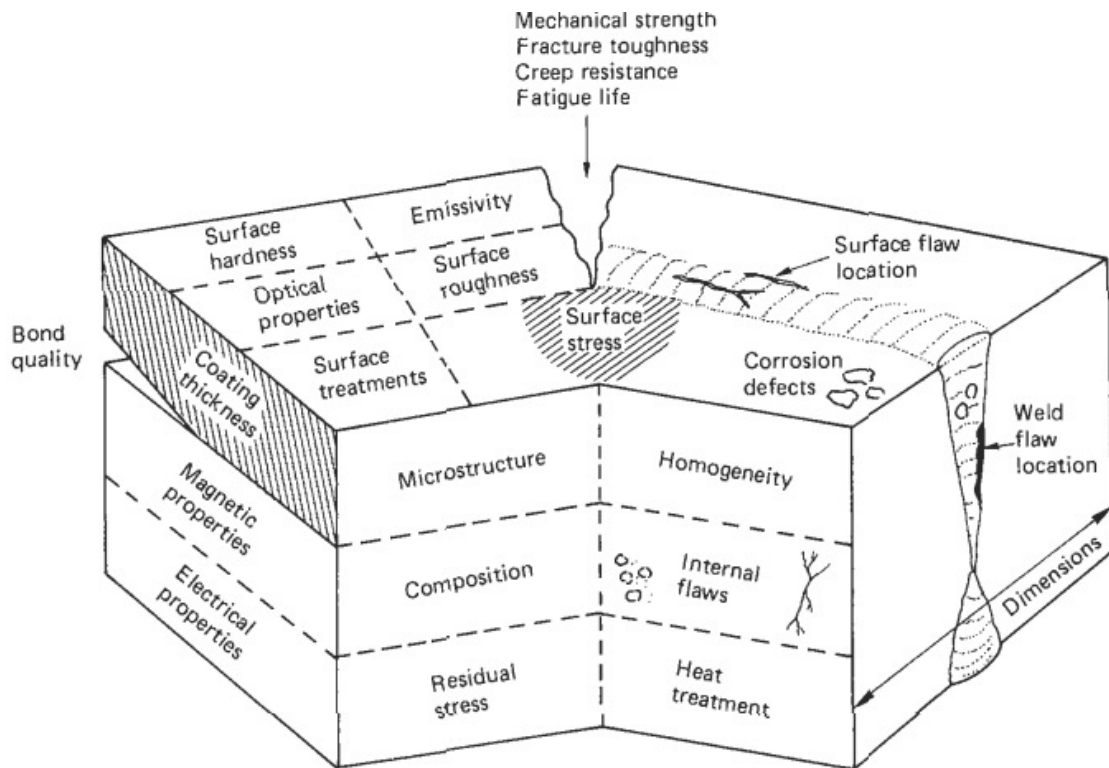
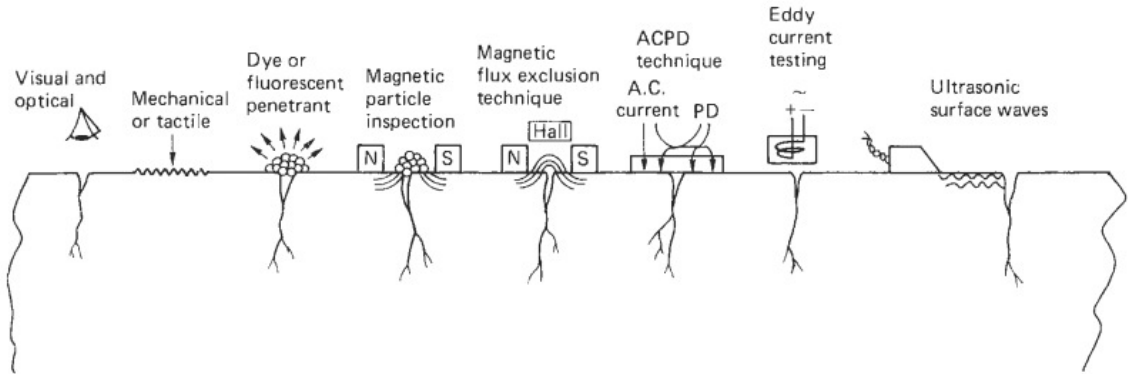
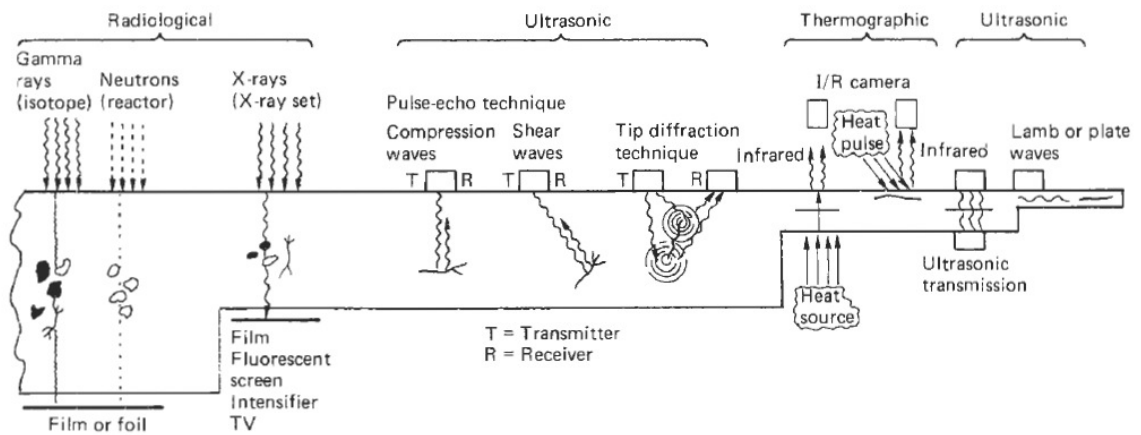


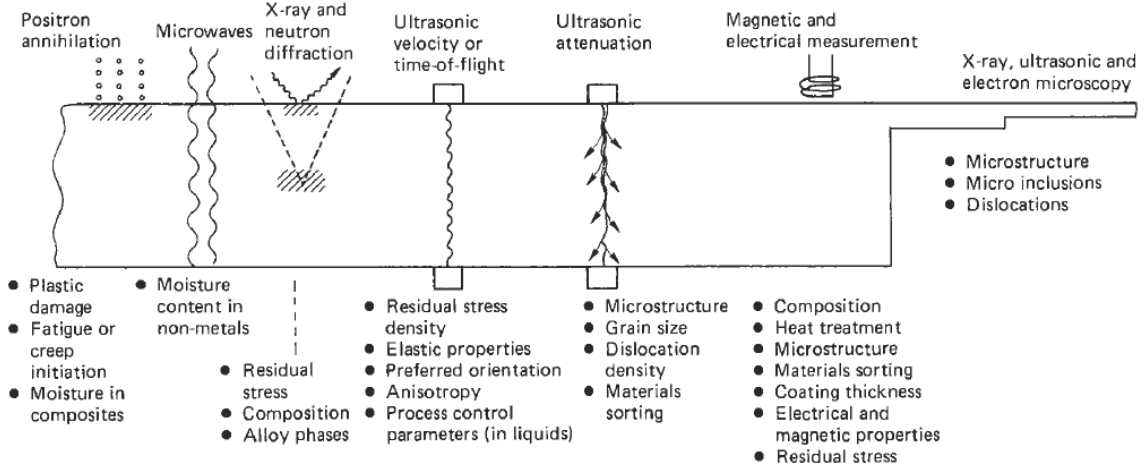
Figure 1.2: Summary of material properties of interest for non-destructive inspection [6]



Surface flaw detection



Internal flaw detection



Monitoring structural variability

Figure 1.3: Summary of NDE methods [6]

1.2.1 Materials

Understanding the material type that needs to be inspected is very important for selection of the appropriate NDT process and further on, for signal analysis. For example, while eddy current is suitable method for turbine blade inspection, it does not work for inspection of any polymer-based or cement composites. Material properties such as conductivity, attenuation etc plays an important role on energy propagation inside the material, and subsequent signal pickup by a receiver. Table 1.1 provides a comparison of the various common material types, their properties and the most suitable energy form used for flaw detection.

Apart from the selection of the energy type for inspection, it is important to understand the interaction of the energy with the flaw or volume of interest. Inspections generally try to optimize energy parameters to maximize the flaw contrast for higher probability of detection. There are multiple parameters, such as angle of incidence, area of sensor, nature of surface etc that govern the contrast and detection probability, and it is important to know them for various sensing methods before inspecting.

Table 1.1: A guide to selection of NDT methods for various materials and discontinuities [7]

| Test Object Material | Discontinuity Type | Visual and Optical | Radiography | Electromagnetic | Ultrasonic | Liquid Penetrant | Magnetic Particle | Acoustic Emission | Infrared and Thermal |
|--------------------------|------------------------------------|--------------------|-------------|-----------------|------------|------------------|-------------------|-------------------|----------------------|
| Ferromagnetic metal | Surface-breaking cracks | X | X | X | X | X | X | X | |
| | Non-surface-breaking cracks | | X | X | X | | X | X | X |
| Non-ferromagnetic metal | Surface-breaking cracks | X | X | X | X | X | | X | |
| | Non-surface-breaking cracks | | X | X | X | | | X | X |
| Metal (generic) | Corrosion pitting (hidden surface) | | X | X | X | | | | |
| | Stress corrosion cracking* | | | | | | | | |
| | Welds - lack of penetration | | X | X | X | | | | |
| | Welds - porosity | | X | X | X | | | | |
| Polymer-matrix composite | Delamination/disbonding | | | | X | | | X | X |
| | Porosity | | X | | X | | | | X |
| | Impact Damage | X | | | X | | | X | X |
| Polymers | Cure | | | | X | | | | |
| | Disbonds | | X | | X | | | | X |
| | Voids/Porosity | | X | | X | | | | X |
| Ceramics | Density | | X | | X | | | | |
| | Voids/Porosity | | X | | X | | | | X |
| | Surface-breaking cracks | X | X | | X | X | | | |
| | Non-surface-breaking cracks | | X | | X | X | | X | |

1.2.2 Energy

Today there is a wide variety of energy sources that are used for interrogating materials. These sources can be broadly classified for the purposes of understanding into the following few broad categories.

- Electromagnetic (Optical, X-ray, UV, IR, Microwave, Gamma Rays)
- Pressure Wave (Acoustic emission, Ultrasound)
- Magnetic (Magnetic particle testing)
- Gravimetric (Chromatography)

Table 1.1 also provides a summary of the above-mentioned techniques in relation to their compatibility with inspected materials and flaw types detected. It is interesting to note

that inspections can also be classified into surface and volume property inspection, based on the location of flaw to be detected and range of probing energy. The most common method of inspection, that needs an explicit mention here, is visual inspection. The source here could be sunlight or a flashlight and is almost always a surface inspection. There are other related methods that use certain “tricks” to improve the measurement resolution of our eye by enhancing the defect properties, such as fluorescent or dye penetrant tests.

1.2.3 Signal analysis

With advances in electronics and computation prowess available in the field, signal analysis for NDT data has, in certain places, outgrown sensor development. The most fundamental classification used is the signal dimension. The objective of any signal analysis is again to enhance the contrast between foreground and background, and to use the scale information to measure or size flaw or material properties.

1.2.4 Emerging technologies

The increase of available computing power, sensor miniaturization, exploitation of new physical phenomena etc, are paving the way for inspection methods and reliability levels that would usher a new era of prognosis and health monitoring (PHM) capabilities. A very brief summary of certain developments in this area is presented in the following paragraphs.

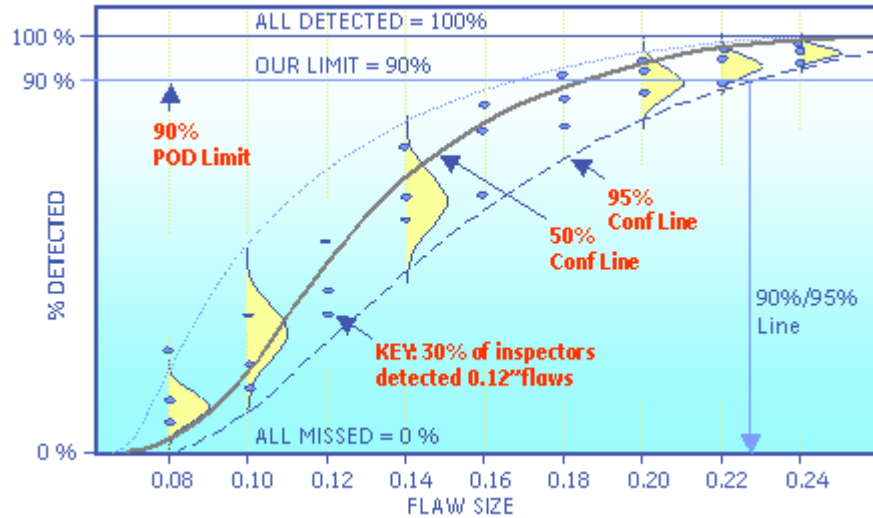


Figure 1.4: Schematic explanation of Probability of Detection (PoD) curve

Computing power is enabling new data visualization and analysis techniques in the field that were previously unthinkable. Apart from being able to raise signal-to-noise ratio for better probability of detection (POD) (see figure 1.4), faster data processing and automated interpretation algorithms are increasing the throughput time for inspection result delivery.

Sensors are benefiting from new methods of manufacturing that are enabling them with higher reliability in harsh environments and lower power consumption. These new methods are also allowing smaller sensor with better properties, such as CMUT sensors that are smaller, embeddable and have better air-coupling capabilities [8].

New sensors and sensing principles are also getting developed and employed in various industries, mainly due to the emergence of new issues and constraints. For example, in the field of radiography, the emergence of digital panel or flexible computer tomography (CT) detectors [9] have radically expanded the possibilities in the area. Other

examples include development of microwave and terahertz based detection technologies [10] [11] [12] to help see defects, such as in space shuttle insulation tiles.

The emergence of inspection methods from being preventive to proactive [4] is transforming the way inspection and sensing needs are being defined today (figure 1.1). PHM with multiple inspection and monitoring sensors is defining new methods for data fusion [13] to help derive new information out of dataset, as opposed to individual and un-correlated sensors.

The future of NDT is definitely going to be governed more and more by emerging needs for convenient and reliable inspection sensors and methods. New issues that would likely arise are transmission and archival of higher bandwidth inspection data and tracking historical inspection information. However, with the emergence of higher computation power and newer methods of data organization, the solutions are in the horizon.

1.3 Ultrasonic investigation methods

1.3.1 Principles

Ultrasound is a pressure wave, similar to the sound we hear everyday, except for the fact that it is produced at a higher frequency – much above the normal hearing range of 20kHz [14]. Higher frequency automatically means smaller wavelength and higher resolving power when used for any measurements. Ultrasound has been a very valuable tool as one of the NDT methods, and can be used on both metallic and non-metallic components. During an ultrasound inspection the ultrasound energy is injected into the material and a receiver listens to the reflected or transmitted energy. Flaws such as cracks or delamination create a high acoustic impedance mismatch triggering the reflection of

the incident wave back to the source. Fundamentally any treatment of such an inspection needs the understanding of energy sources (trans-receivers) and material interactions, which are further described below.

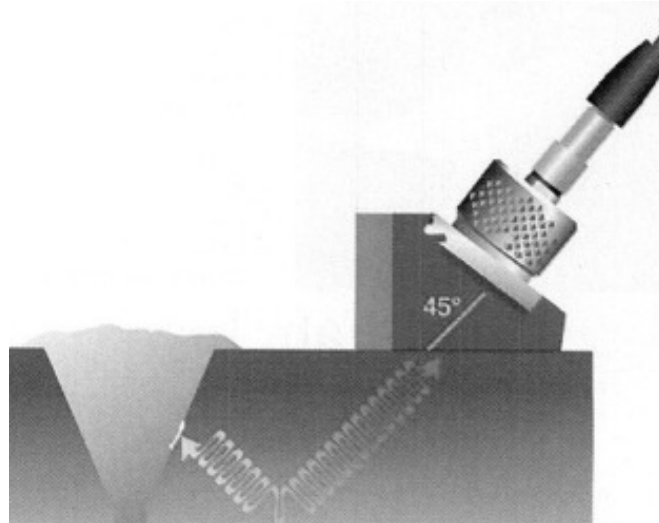


Figure 1.5: Fundamental schematic of ultrasonic inspection method

1.3.2 Energy sources

Signal sources and receivers

Ultrasound energy is typically generated with the use of an oscillating diaphragm or surface. In practice, the transducers contain piezoelectric ceramic materials that oscillate with applied voltage. The most common material used for this purpose is lead-zirconium titanate (PZT). These sources are usually made rugged by covering the transducer surface with a wear resistant coating and the back surface is adequately damped by matching layers of material. An oscillating current generator with adjustable voltage, frequency, etc. is attached to the source and provides adequate control to the energy generated. The sources also have the natural frequency set and measured during the manufacturing process and the selection of a source of a particular frequency is

usually determined by the problem at hand. A thing to keep in mind is that the depth of penetration from the surface is inversely proportional to the frequency of the source. Ultrasound sources are usually available for a wide range of frequencies and sizes ranging from 10 KHz to 10 MHz and 3 mm to 25 mm respectively. It is interesting to note that the energy sources also act as receivers and thus they are usually referred as ultrasonic transducers or trans-receivers. The receivers can be placed in a through-transmission mode or a pulse-echo mode. In through-transmission mode, the source and the receiver are placed in opposite sides of the material under investigation, and the change in the signal as it passes through the medium acts as an indicator of its properties. In the pulse-echo mode, the source and the receiver are placed on the same side of the specimen. Usually the source itself acts as a receiver, shifting from source to receiver mode with a time delay. In practice, due to access restrictions to reach out on both sides of a specimen, such as during wing or fuselage inspection, pulse-echo testing is more commonly used in the industry.

Important contact attributes

The propagation of ultrasound from the source to the medium under investigation is governed by the contact parameters that define the efficiency of energy transfer. These parameters include ratio of acoustic impedance, contact pressure and contact area. Usually to increase the energy transfer from the source into the medium, a layer of water or glycerin like material is used as an intermediate layer. This eliminates any entrapped air bubbles that might lead to severe signal loss. It is important to also have a uniform contact pressure across the contact diameter to reduce any artifacts in the measurements. The amount of energy is related to the diameter of the transducer and thus for higher

energy transfer bigger transducers are used. In many applications the transducer needs to be moved along the surface of the inspected body and it is thus important to ensure the above parameters are held as consistently as possible. Sometimes, as indicated in figure 1.5, specially constructed wedges are used to introduce an angled beam into the material in question.

1.3.3 Energy interaction

An understanding of the interaction of ultrasound with materials is key to flaw detection and measurement. While a lot of advancement in the sensors and signal processing has been happening in the recent years, deeper understanding of the physics of interactions is enabling new inspection methods and measurements that are hard to achieve, such as the Synthetic Aperture Focusing Technique (SAFT).

Acoustic propagation and wave modes

Speed of acoustic wave propagation is governed by the elastic properties of the material, and is used for flaw localization. Defects and features in materials that reflect ultrasound are evaluated by the travel time or “time of flight” (ToF) to compute the distance of the feature in question from the sensor or transducer. The interaction of ultrasound with solids also creates multiple wave modes in the medium. Apart from the longitudinal waves that are incident on the material, shear waves are also supported in solids, which in turn appear as Rayleigh waves on the surface (in superposition with longitudinal waves). Surface waves are useful for detection of surface abnormalities in large area inspections, such as in piping structures.

Energy losses

In this research, particular emphasis is laid upon material characterization through understanding the energy loss in the medium. The energy losses can appear as dissipative losses (actual loss of energy or attenuation of wave amplitude due to frictional heating and other non-linear phenomena at the phase boundaries in the medium) or scattering losses (redistribution of energy through multi-directional reflection of the signal due particles or grain boundaries). Sometimes in field NDE measurements and scan display, attenuation losses are corrected in the “A-scans” or “B-scans” for easier interpretation through the use of pre-calculated ADC curves [15].

Acoustic impedance and flaw detection

The difference in material property results in varying wave speed of ultrasonic waves in different media. The difference in the wave speed also manifests as separation of the incident energy at the phase boundary into reflected and refracted waves, much like electromagnetic waves. The equations governing this phenomenon is mentioned in this chapter (equation 1.1), however – it is interesting to note that the portion of the reflected energy gets larger with increasing impedance mismatch. Features inside the materials such as cracks or voids contain entrapped air, which results in strong reflected waves that are picked up by the transducers and analyzed for detection and sizing. Thus, due to the finite diameter of transducers, larger cracks and voids produce stronger signal on the oscilloscope, and are easier to detect. Typical 90/95 probability of detection (POD) for field cracks using ultrasound is about 200 mils [7].

Material property estimation

Since material property plays a key role in determining the speed of ultrasound, as well as its attenuation and scattering, it is possible to estimate material properties by measuring the effects. In this research and following [2] and [16], it is shown that the dissipation and diffusion rate of incident ultrasound wave is governed by the accumulated damage in the specimen and the specimen geometry. Thus by measuring the values of these diffusion and dissipation rates, we can non-destructively estimate the health of concrete based structures and components.

1.4 Inspection of concrete infrastructure

Cement based infrastructure is a major part of our everyday life. The recent Minnesota bridge collapse [17] highlights the importance of inspection to prevent catastrophic consequences. Such incidents are a great example of why research on non-destructive ultrasound evaluation of heterogeneous materials has so much practical importance.

1.4.1 Cement-based materials

Cement based materials are heterogeneous and consists of two phases – the matrix material and the aggregate material. The aggregate is also known as the filler or binder materials. Typically sand and gravel are used, as the aggregate material while the matrix phase is usually a mixture of cement and water that chemically react to form a cement paste. Listed next are three varieties:

Cement paste is a cured mixture of cement and water in a certain ratio that is fixed by the desired properties of the mixture. In some cases, additives are used in very small volume fractions to improve certain properties such as susceptibility to cracking.

Portland concrete is a cured mixture of coarse aggregate and cement paste.

Mortar is a cured mixture of fine aggregate and cement paste.

Table 1.2: Typical properties of concrete material

| Property | Symbol | Value |
|----------------------|------------|------------------------|
| Compressive strength | σ_0 | 35 MPa |
| Flexural strength | τ_0 | 6 MPa |
| Tensile strength | σ_0 | 3 MPa |
| Young's modulus | E | 28 GPa |
| Poisson's ratio | ν | 0.18 |
| Density | ρ | 1300 kg/m ³ |
| Strain at failure | ϵ | 0.001 |

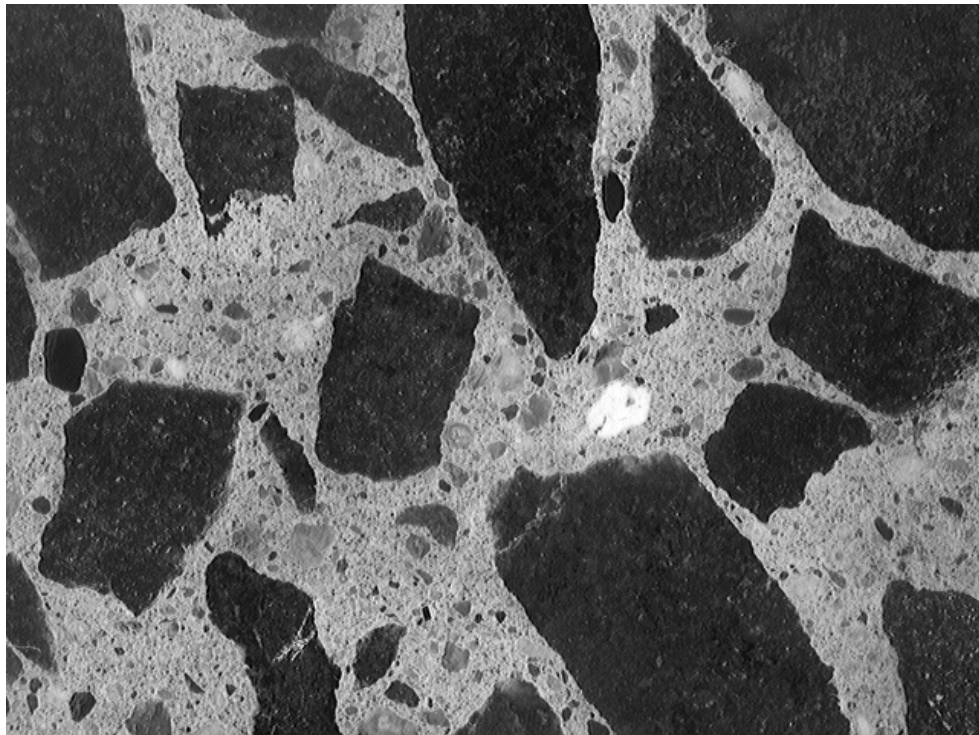


Figure 1.6: Typical cross-section of concrete, illustrating the distribution of both coarse and fine aggregates [18]

Information about the very complex microstructure, elasticity and plasticity properties of cement-based materials is available in a number of monographs. Some important mechanical properties of standard Portland concrete are summarized in table 1.2. It is interesting to note that cement based materials cause ultrasonic waves to attenuate significantly, of typical attenuation values of 25-75 dB/m for ultrasonic waves in the 100-200 kHz range, depending on the material composition [19].

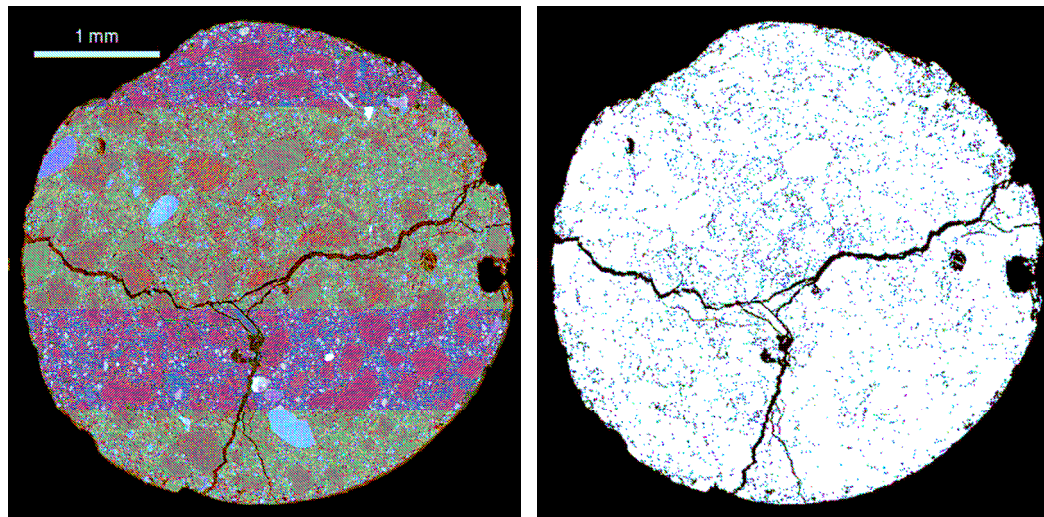
1.4.2 Flaws and failure mechanisms

Damage in cement based materials usually have a relatively small length scale and is often distributed throughout the volume. This damage is of the order of the grain size. Typical examples of such damage include freeze-thaw, intrusion of water and acids, alkali silica reaction (ASR) and even dynamic loading. Due to the fact that the size of the defects are of the same order as the grain size, common ultrasound evaluation methods are rendered less useful since they cannot differentiate between microstructure features (such as aggregate and porosity) and damage. Unfortunately, they all scatter the ultrasonic waves in a very similar fashion.

1.4.3 Common inspection methods

The following paragraphs and section 1.4.4 provide a short review and summary of the common inspection methods for testing concrete and other cement-based materials, and much of this information is available and excerpted from Becker et al [3]. Most of the methods use ultrasound of 100 kHz or less, mainly due to the low scattering seen at these frequencies. These methods treat the cement-based materials as a near homogeneous medium. As mentioned earlier, lower frequencies imply higher wavelength

and lower resolution. The small amount of scattering seen is regarded as grain-noise or structural noise in this context (see Becker et al [2] and Schickert)



(a) X-ray CT slice

(b) Segmented porosity

Figure 1.7: Cracked mortar specimen [2]

Impact-echo is a method where the structure under investigation is struck with a hammer blow, and the response of the structure is measured close to the location of the hammer. A Fourier transform of the measured signal is calculated, and the resonance peaks are observed as indications of change from a perfect structure scenario. This method is relatively empirical, since the correlation of resonance frequencies and structures are known only for simple geometries, and is limited to testing of circular columns.

Pulse-echo method is one of the most common means of testing in the industry as already discussed. In this method, the source and receiver are placed on the same side of the material to be tested, which is favorable in practical application that allow only one sided access to the examined structure. This method is very similar to the use of

ultrasound for medical applications. In this method, signal is reflected due to acoustic impedance of a phase boundary. As an example, considering the acoustic impedance of concrete to be Z_1 and that of air to be Z_2 , the following relation gives the reflective acoustic impedance of the concrete-to-air boundary:

$$R = \frac{(Z_2 - Z_1)}{(Z_2 + Z_1)}$$

(Eq 1.1)

As evident from the relation, a higher mismatch between the acoustic impedance of the two media, such as concrete and air, results in very high reflective energy being directed towards the source. Thus, typical flaws in concrete, such as cracks and air-voids reflect off energy that serve as a measure of the health of the structure. However, due to the heterogeneous nature of concrete, the grain boundaries and other secondary phase materials also reflect and scatter much of the incident energy, resulting in significant noise and loss of signal amplitude. This tends to mask interesting features like holes, layer boundaries or back walls. Several modifications help decrease these distortion effects, namely spatial averaging, large surface area transducer and pulse-compression techniques [20].

Spectral analysis of surface waves (SASW) is a one-sided inspection technique that measures the phase and dispersion of sound signal to estimate the flaw and flaw depth. This method uses a hammer strike to create the wide-spectrum sound source. Since the depth of sound penetration is a function of the frequency, the spectral analysis of the received signal and its comparison provides an estimate of the modulation of sound wave at various depths from the surface. For example, in one application the velocity decreases from 2150-2750 m/s without damage to 1200-2100 m/s [2] with damage. However, flaws

that are located deep within a structure cannot be detected using this method. Suggested improvement of this method could be the use of broadband transducer to replace the hammer strike, which would further enable averaging across multiple measurements due to consistency in the signal source.

Synthetic aperture focusing technique (SAFT) is a measurement technique based on pulse-echo principle, but uses advanced phased array transducers for creating focused beam, and sophisticated algorithms to reconstruct two-dimensional sections along the depth of the inspected volume. This method is based on subsequent focusing of the data measured on an aperture to every point of the reconstructed area through superposition of the time records. The reconstructed image is in terms of impedance differences caused by structural features, such as the back wall and inclusions. Some of the propagation properties of SAFT make it more suitable for inspection of concrete, as compared to conventional A and B-scan techniques, as detailed in [21]. Some extensions to the fundamental algorithm and technique as applied to cement-based materials has been done by the group of [22]. Reconstruction results measured both in laboratory and in the field illustrate that SAFT is already applicable to testing concrete with grain size up to 16 mm and is a promising tool for the inspection of concrete with high resolution.

Split-spectrum processing (SSP) is an improvement on the common pulse-echo method through the use of advanced noise filtering techniques. Essentially, higher frequencies are more scattered in cement-based materials due to their smaller wavelengths. This accounts for a disproportionate amount of signal noise along the frequency spectrum of the received signal. However, the reflected energy from flaws in the structure is insensitive to frequency. By using advanced digital signal processing

techniques, each signal is a certain frequency is filtered by appropriate noise suppression techniques and finally the output signal is reassembled nonlinearly from the individual frequency band signals. The important parameters of this method are number of frequency bands, bandwidth and their covered frequency range, the noise suppression algorithms and the reassembling method. Popovics [23] describes in more details the testing method and its adaptation to concrete. However, though automated SSP algorithms are already in use for metal testing, their application to concrete structures is found to be much more cumbersome.

1.4.4 Summary

A typical form of damage to cement-based materials is the random growth of multiple small cracks in a given region. The methods described briefly in the section above are typically more suitable for damage detection of size much larger than length scale of the scatters in the material. This limits the application, since much early stage damage accumulation and manifestation happen in the form of distributed cracking of the aggregate.

Selleck et al [24] has done direct optical microscopy based observations on freeze-thaw damaged concrete specimens, and they show uniformly distributed micro-cracking. Similar to castings, distributed porosity also deteriorates cement-based materials and leads to increased damage rates. This emphasizes the study of nondestructive evaluation methods for looking at small-distributed cracks is important to truly assess the damage accumulation in cement-based materials, especially in their early stages of damage.

The work by Selleck et al describes experimentally measured properties of the time domain impulse response of different damaged concrete specimens. The microscopic examinations reveal the existence of distributed micro-cracking after repeated and systematic freeze-thaw cycles in a salt pond. In the experiment, a broadband transducer of 500KHz center frequency is used as an exciter and the response is measured in a transmission setup at multiple surface points. The measurements on the received signal include velocity, first to second peak amplitude difference, as well as the peak frequency of the Fourier transformed time signal. It is found that the velocity shows a very small decrease with damage, 3 and 9% for dynamic Young's modulus reduction of 25 and 50% respectively, for example. On the other hand the peak-to-peak amplitude is more sensitive to damage and the decrease by 31 and 84% for the same state of damage. The peak frequency reduces about 44 and 76%. These numbers show that the deviations are large and often in the same range as the differences between different specimens. These effects make practical use of this approach questionable.

CHAPTER 2

LITERATURE SURVEY

2.1 Introduction

Cement based materials provide a challenge for ultrasound diffusion and attenuation measurements due to the strong scattering from randomly distributed aggregates in the medium. Adding on, very high attenuation coefficient and difficult contact on rough surface make the job much more challenging.

2.2 Attenuation measurements

Owino and Jacobs [25] used laser ultrasonic techniques to quantify the frequency-dependent attenuation losses of Rayleigh waves in cement-based materials; these materials are heterogeneous in nature, and this heterogeneity is seen at multiple length scales. As a result, ultrasonic waves that propagate in cement-based materials exhibit a high degree of (material) attenuation losses. Physically, these attenuation losses are a combination of internal friction, such as the work done at material interfaces (ultrasonic absorption) and the scattering losses due to material heterogeneity. The high fidelity, large frequency bandwidth, and absolute, non-contact nature of laser ultrasonics makes this an ideal methodology to measure attenuation in these materials. In this research, they use a dual-probe, heterodyne interferometer to experimentally measure these attenuation losses (as a function of frequency) in three different materials: (1) aluminum; (2) mortar; and (3) granite. The aluminum results (aluminum is homogeneous at the wavelengths used here) are used to demonstrate the fidelity of the laser ultrasonic measurement technique, while the mortar and granite results (both are heterogeneous at these

wavelengths) are used to quantify the attenuation losses present in each material. The attenuation and coherence of the signal as a function of frequency is calculated and examined. The experiments conclude that the attenuation mainly depends on the volume fraction of the aggregates, and not on their size distribution. This attributed is to the low impedance mismatch between the matrix and the aggregate.

Landis et al [24] measure attenuation of longitudinal waves in cement paste (no aggregate), fine mortar (sand aggregate diameter about 1 mm), coarse aggregate (aggregate diameter about 5 mm) and concrete (maximum aggregate diameter about 10 mm). They use the fracture of glass capillary as a highly localized source, and detect the response with a point receiver. With this setup, the attenuation can be consistently determined up to 800 kHz for cement paste, 400 KHz for fine mortar, 300 KHz for coarse mortar and 150 KHz for concrete specimens. It is found that the frequency cut-off values depend on the size of the scatterers, however no linear relationship is found between them. The specimens tested in this experiment are of the order of 30 – 40 mm and the transfer of the results to longer transmission lengths is unclear.

Punurai and Jacobs et al [16] perform quantitative characterization of the capillary porosity and entrained air content in hardened cement paste with ultrasound. Direct measurements of ultrasonic attenuation are used to measure the volume fraction and average size of entrained air voids and to assess variations in intrinsic porosity – as influenced by water-to-cement ratio (w/c) – in hardened cement paste specimens. For the air entrained specimens, an inversion procedure based on a theoretical attenuation model is used to predict the average size and volume fraction of entrained air voids in each specimen, producing results in very good agreement with results obtained by standard

petrographic methods and by gravimetric analysis. In addition, ultrasonic attenuation measurements are related to w/c to quantify the relationship between increasing porosity (with increasing w/c) and ultrasonic wave characteristics.

2.3 Diffuse field measurements

Turner [18] measures the depth of surface-breaking cracks in concrete specimens using an ultrasound diffusion technique. Experiments are carried out on pre-cracked concrete specimens of varying crack depths (0 - 40% of the specimen thickness) with contact transducers placed at the specimen surface with source and receiver separated by the crack. Tone burst excitations over a frequency range of 400-600 KHz are used. At these frequencies, ultrasound is scattered considerably by the heterogeneities in the concrete. In the limit of many scattering events, the evolution of energy may be modeled as a diffusion process. The arrival of the peak diffuse energy at the receiver is delayed due to the presence of crack. This delay is the prime indicator used for determining crack depth. Several data reduction methods are explored and discussed. Numerical and analytical analyses are also used for comparison. The results are in basic agreement with the experiments. In addition, these analyses are used to study the limits of this technique. In particular, it is shown that this technique is applicable to cracks greater than the scattering mean free path, which is estimated at 1 cm for these specimens.

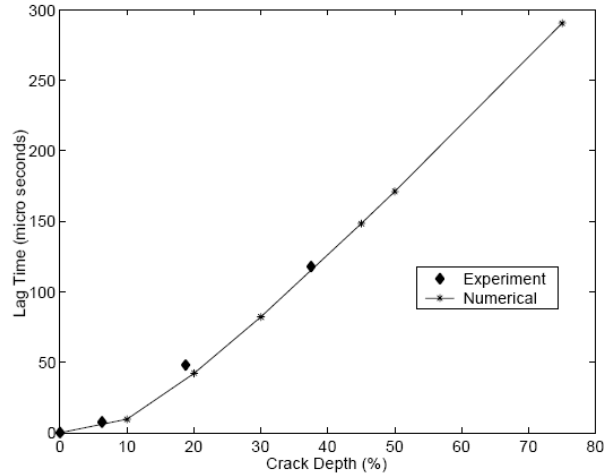


Figure 2.1: Peak energy time difference across the crack and at un-cracked region

(Lag time) vs crack-depth for a separation distance of 6 cm

Aspects of practical implementation are also discussed. The study however is limited to finding correlation of attenuation to crack length, and does not discuss the effects of specimen geometry. However, as shown in figure 2.1, the peak energy time difference is found to be a useful indicator for the presence of cracks in a region.

Schubert [26] mentioned that certain aspects of diffusive ultrasound fields in concrete are still unknown and thus, systematic parameter studies using numerical time-domain simulations of the ultrasonic propagation process could lead to further insights into theoretical and experimental questions. In their paper, the elasto-dynamic finite integration technique (EFIT) is used to simulate a diffusive reverberation measurement at a concrete specimen taking aggregates, pores, and visco-elastic damping explicitly into account. The numerical results for dissipation and diffusivity are compared with theoretical models. Moreover, the influence of air-filled pores in the cement matrix is demonstrated. Schubert concludes that the results of the numerical experiments are plausible and consistent with the assumptions of a diffusive energy transport, and they

reveal a significant impact of porosity on the diffusion coefficient. Due to the fact that micro-structural damage is expected to have similar effects on wave scattering than porosity, the use of high-frequency diffusive ultrasound is suggested to lead to new nondestructive methods for characterizing material properties and damage in concrete structures.

Turner and Anugonda [27] also arrive at the same conclusion through theoretical and experimental measurements of ultrasound diffusion in cement based materials. They use the one dimensional heat-diffusion equation to model the propagation of energy and validate their computation with experimental data across multiple frequency bands.

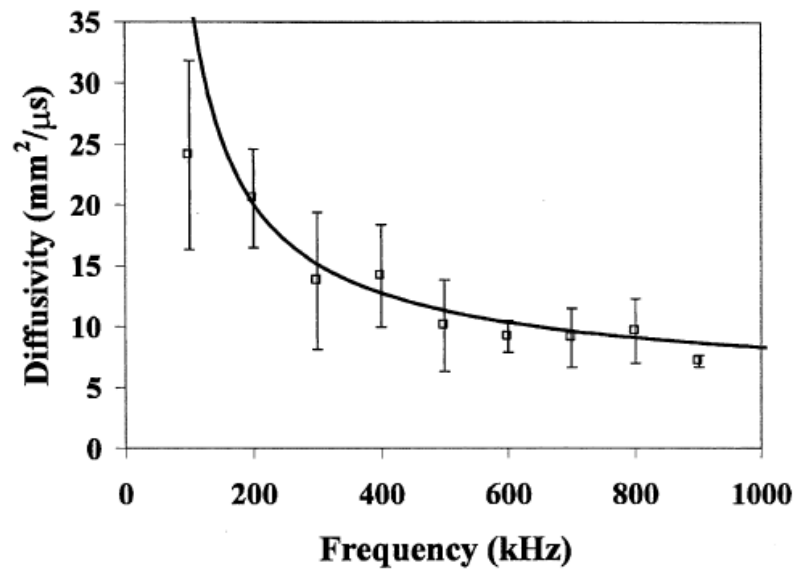


Figure 2.2: Elastic diffusivity as a function of frequency in concrete specimens, solid line indicates theoretical estimate and symbols correspond to experimental data.

2.4 Phase and velocity measurements

Philippidis [28], on the contrary, introduces narrowband pulses at several frequencies into cement based materials such as cement paste, mortar and concrete

allowing direct measurement of longitudinal wave velocities and amplitude for each frequency. It is shown that aggregate content play an important role in wave propagation increasing considerably the wave velocity, while the aggregate size seems to control the attenuation observed. Slight velocity variations observed with frequency are discussed in relation to the degree of inhomogeneity of the materials. The results highlight the w/c influence being mostly evident on paste and mortar while the aggregate content is a decisive parameter in the propagation behavior of mortar and concrete.

Chaix et al [29] uses immersive ultrasonic technique to characterize micro-cracks caused by thermal damage in concrete. The propagation of the longitudinal wave in the heterogeneous media is studied via a homogenization model that integrates the multiple scattering of waves. The model helps determine the phase velocity and the attenuation according to the elements that make the medium on a frequency domain, which ranges from 160 kHz to 1.3 MHz. The analysis of the simulation results show a characteristic behavior of the wave phase velocity through the parameters of locations and shapes of the scatterers associated with a minimum in the frequency domain. The main perspectives for this study were to take into account in a more realistic way the morphology of the scatterers generated by the damage of the concrete in order to aim at a quantitative validation of the real direct problem.

2.5 Diffusion modeling

Jacobs & Qu et al [16] quantifies the dissipation losses in cement paste using diffuse ultrasound, and then relates these results to the corresponding values measured with a coherent ultrasound procedure. The results show a linear dependency on frequency for this energy dissipation (intrinsic absorption), and exhibit a reasonable correlation

between the dissipation losses and the amount of cement paste present in a specimen. In addition, there is good agreement between the air content predicted with diffuse ultrasound, and that directly measured with a standard optical technique.

Becker et al [2] aims to develop a quantitative understanding of the propagation of ultrasonic waves in cement-based materials by examining specimens made of a Portland cement-paste matrix and glass bead “aggregate.” The incident ultrasonic waves are broadband and contain wavelengths on the order of the glass bead scatterers. Experimentally measured ultrasonic waves are interpreted using diffusion theory to quantitatively measure dissipation and diffusion coefficients as functions of frequency and microstructure. These results provide a basic understanding of the effect of some features of the microstructure on the propagation of ultrasonic waves, as well as supplying a first step in the characterization of distributed damage using ultrasonic methodologies. The wave diffusion theory for elastic solids is a statistical method that directly accounts for the statistical character of the crack distribution and the random nature of the dual phase heterogeneous medium. Becker et al appropriately shows the possibility of measuring an approximation of the diffusion and dissipation coefficients through modeling the ultrasound propagation as energy diffusion in an infinitely thin plate. However the specimens used for the experiments have finite radii and height, their adiabatic walls contain the energy for a longer duration of time when compared to the theoretical prediction. The work in this research uses the diffusion approximation for a finite plate and quantitatively illustrates the energy diffusion and compares to results by Becker et al. As is indicated in latter sections, apart from the geometric effects of the specimen, this research also aims to find correlation between specimen damage and the

residual energy characteristics from the measured response signal. This research is an extension of the work by Becker et al where the effect of specimen geometry is studied and experimentally validated to obtain a diffusion curve that fits the experimental observation over the initial and extended diffusion temporal regimes.

CHAPTER 3

THEORETICAL BACKGROUND

Becker [3] and Jacobs [16] provide an excellent introduction to the theoretical background of wave propagation in elastic solids and to the signal processing method used in this study. This chapter and introductory sections of chapter 4 are excerpted from their work. There are a number of authoritative and comprehensive books on wave propagation theory, for example [30] [31]. Digital Signal Processing is covered by [32] [33].

3.1 Wave propagation

3.1.1 Linear elasticity and equation of motion

In linear elasticity, the traction t_i on a plane $n_i x_i$ is given by

$$t_i = \sigma_{ji} n_j \tag{Eq 3.1}$$

where σ_{ji} is the stress tensor.

The balance of linear momentum for a body with volume V and surface S can be expressed as

$$\int_S \sigma_{ki} n_k dS + \int_V \rho f_i dV = \int_V \rho \ddot{u}_i dV \tag{Eq 3.2}$$

with ρ representing the material mass density and f_i the body force. Gauss' theorem applied to Eq. 3.2 leads to

$$\int_V (\sigma_{kl,k} + \rho f_l - \rho \ddot{u}_l) dV = 0 \quad (\text{Eq 3.3})$$

Equation 3.3 has to be fulfilled for any arbitrary volume V of the body and therefore the stress equations of motion becomes

$$\sigma_{kl,k} + \rho f_l = \rho \ddot{u}_l \quad (\text{Eq 3.4})$$

It is often more efficient to have the equations of motion given solely in terms of the displacement, u_i (as opposed to Eq. 3.4, which has terms of stress σ_{ij} and displacement u_i). This can be achieved by applying Hooke's law for a homogeneous, isotropic and linear elastic medium, which is given by

$$\sigma_{ij} = \lambda \varepsilon_{kk} \delta_{ij} + 2\mu \varepsilon_{ij} \quad (\text{Eq 3.5})$$

The strain tensor ε_{ij} is related to the displacement u_i by

$$\varepsilon_{ij} = \frac{1}{2}(u_{i,j} + u_{j,i}) \quad (\text{Eq 3.6})$$

μ and λ are the Lamé constants. Plugging Eq. 3.6 into Eq. 3.5 and subsequently into Eq. 3.4 leads to Lamé-Navier's equations of motion.

$$\mu u_{i,jj} + (\lambda + \mu) u_{j,ji} = \rho \ddot{u}_i \quad (\text{Eq 3.7})$$

$$\mu \nabla \mathbf{u} + (\lambda + \mu) \nabla \nabla \cdot \mathbf{u} = \rho \ddot{\mathbf{u}} \quad (\text{Eq 3.8})$$

Note that in this development, body forces f are neglected. Solving Eq. 3.8, however, is difficult, because it is a coupled partial differential equation (PDE), The Helmholtz decomposition

$$\mathbf{u} = \nabla \varphi + \nabla \times \boldsymbol{\psi} \quad (\text{Eq 3.9})$$

provides a convenient way to uncouple these equations.

Equation 3.9 represents the three components of displacement u with the four functions φ , ψ_1 , ψ_2 and ψ_3 . To guarantee the uniqueness of the solution, an additional constraint

$$\nabla \cdot \boldsymbol{\psi} = 0 \quad (\text{Eq 3.10})$$

is introduced. Substitution of Eq. 3.9 (Helmholtz decomposition) into the displacement equations of motion (Equation 3.8) leads to two uncoupled wave equations expressed in terms of the displacement potentials φ and $\boldsymbol{\psi}$

$$\nabla^2 \varphi = \frac{1}{c_L^2} \ddot{\varphi} \quad , \quad \nabla^2 \boldsymbol{\psi} = \frac{1}{c_T^2} \ddot{\boldsymbol{\psi}} \quad (\text{Eq 3.11})$$

The variable c_L represents the wave speed of the longitudinal wave and c_T the wave speed of the vertically and horizontally polarized (transverse) shear waves

$$c_L^2 = \frac{\lambda + 2\mu}{\rho} \quad , \quad c_T^2 = \frac{\mu}{\rho} \quad (\text{Eq 3.12})$$

It always holds $c_L > c_T$. Both wave speed equations are expressed in terms of material properties density ρ and the Lamé constants μ and λ . A relationship to material properties Young's modulus E and Poisson's ration ν is given by

$$\lambda = \frac{E\nu}{(1+\nu)(1-2\nu)} \quad (\text{Eq 3.13})$$

$$\mu = \frac{E}{2(1+\nu)} \quad (\text{Eq 3.14})$$

3.1.2 Wave phenomenon

Wave phenomena discussed in this section are based on the plane wave assumption i.e. assuming a wave with constant properties (ϵ, σ, u) on a plane perpendicular to its direction of propagation \mathbf{p}

$$\mathbf{u} = f(x \cdot \mathbf{p} - ct)\mathbf{d} \quad (\text{Eq 3.15})$$

Equation 3.15 shows the mathematical representation of a plane wave where \mathbf{d} is the unit vector defining the direction of particle motion, and c is either the longitudinal wave speed c_L or the transverse wave speed c_T . By substituting Eq. 3.15 into Eq. 3.8, one obtains

$$(\mu - \rho c^2)\mathbf{d} + (\lambda + \mu)(\mathbf{p} \cdot \mathbf{d})\mathbf{p} = 0 \quad (\text{Eq 3.16})$$

Since \mathbf{p} and \mathbf{d} are two different unit vectors, it can immediately be seen that the two possible solutions that form the basis of wave propagation are either $\mathbf{d} = \pm \mathbf{p}$ or $\mathbf{p} \cdot \mathbf{d} = 0$:

- $\mathbf{d} = \pm \mathbf{p}$ leads to $\mathbf{p} \cdot \mathbf{d} = \pm 1$ and yields with Eq. 3.16, $c = c_L$ (see Eq. 3.12). Since \mathbf{d} and \mathbf{p} are linearly dependent, this represents a particle movement in the direction of propagation – a longitudinal or P-wave.

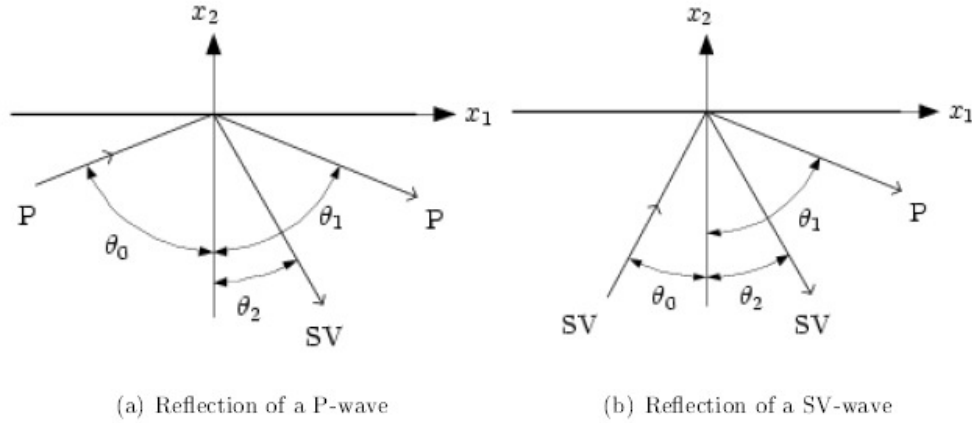


Figure 3.1 Wave reflections

- $\mathbf{p} \cdot \mathbf{d} = 0$ yields with Eq. 3.16, $c = c_T$ (see Eq. 3.12). Now the direction of motion is normal to the direction of propagation, and the wave is called a transverse wave. If a two dimensional plane of propagation is considered (for example, the (x_1, x_2) plane), a wave with an in-plane displacement (in the (x_1, x_2) plane) is called SV-wave (vertically polarized), while a wave with out-of-plane displacement (in the x_3 direction) is called a SH-wave (horizontally polarized).

In a homogeneous isotropic material, transverse and longitudinal wave speeds are independent of frequency – they are nondispersive.

3.1.3 Reflections of P and SV-waves

The wave types derived so far propagate independently in an infinite media. As soon as a finite media in the direction of propagation is considered, reflections and coupling will occur. An incident P-wave (SV-wave), which is reflected at a stress free boundary ($\sigma_{22} = 0$ and $\sigma_{21} = 0$) normally consists of both, a P-wave (SV-wave) and a SV-wave (P-wave).

The effect of a single incident wave-type producing two different waves (after reflection from a boundary) is called mode conversion. The displacement field of a

harmonic wave in the x_1, x_2 plane (propagating in infinite media, plane-strain case) can be expressed as,

$$\mathbf{u}^{(n)} = A_n \mathbf{d}^{(n)} e^{ik_n(x_1 p_1^{(n)} + x_2 p_2^{(n)} - c_n t)} \quad (\text{Eq 3.17})$$

whereas n denotes the wave (longitudinal or transverse), $k_n = \frac{\omega}{c_n}$ is called the wavenumber of wave n and the respective wave speeds are c_n . Using these definitions, and noting that the angular frequency ω is equal for the incident and reflected waves, it is possible to determine the relationship between the angle of the incident and the angles of the reflected waves (see Table 3.1)

Table 3.1: Angle relation for reflections on a stress-free surface

| incident θ_0 | reflected P θ_1 | reflected SV θ_2 |
|---------------------|---|---|
| P | $\theta_1 = \theta_0$ | $\sin \theta_2 = (c_T/c_L) \sin \theta_0$ |
| SV | $\sin \theta_1 = (c_L/c_T) \sin \theta_0$ | $\theta_2 = \theta_0$ |

Exceptions of mode conversion are the normal incidence with $\theta_0 = 0$ – in the case, the waves are reflected as themselves, and if the angle θ_0 is greater than a critical angle,

$$\theta_{cr} = \arcsin \frac{c_T}{c_L} \quad (\text{Eq 3.18})$$

then only a SV-wave is reflected. The P-wave portion of the reflected signal degenerates into a surface wave (Rayleigh wave), traveling along the surface and exponentially decreasing in amplitude with increasing depth.

3.2 Attenuation

Several attenuation mechanisms of ultrasonic waves are briefly introduced and their underlying physics are explained. Further theory is available in [34]. In all experimental setups, the superposition of several attenuation types and mechanisms are measured, but the main interest is normally only on the attenuation due to the material absorption and scattering. Therefore the geometry must be known *a priori* in order to be able to predict the geometric attenuation. The ultrasonic source must be well defined, so the ultrasonic wave field is accurately known. If these conditions are met, the (coupled) sum of material, scattering attenuation can be determined in the measured signal.

Attenuation is usually incorporated in the framework previously discussed by the introduction of a complex wave number, k (equivalent to a complex wave speed and complex material constants). The complex wavenumber k^* is defined as

$$k^* = \frac{\omega}{c_L} = k + \alpha j \quad (\text{Eq 3.19})$$

In the example of a plane, harmonic, one-dimensional wave (derived from Eq. 3.15), the displacement field is given by

$$u(x, t) = e^{j(k^*x - \omega t)} \quad (\text{Eq 3.20})$$

The influence of the attenuation coefficient is more obvious if Eq. 3.20 is written as

$$u(x, t) = e^{-\alpha \omega x} e^{j(kx - \omega t)} \quad \text{for } x \geq 0 \quad (\text{Eq 3.21})$$

Note that non-geometric attenuation is intrinsically linked to wave-velocity dispersion by the Kramers-Kronig relationship that is derived from the causality condition that the output strain cannot precede the input stress in any physical material [35].

This is obvious, for example, if the dispersion relation is modified in accordance to Eq. 3.19, which leads to

$$c_L = \frac{\omega}{k^*} = \frac{\omega}{k + \alpha j\omega} \quad (\text{Eq 3.22})$$

where α denotes the attenuation coefficient and k the real part of the wavenumber.

It is clear that the (now complex) wavespeed depends on the frequency, therefore dispersion is found. This means, waves of different frequencies travel with different velocities.

3.2.1 Viscoelastic media

General elasticity theory assumes that a material stores energy without dissipation during deformation. But many materials (e.g. Polymers, composites like cement-based materials) dissipate part of the stored energy. Such materials are called viscoelastic, because they combine the properties of elastic solid and a viscous liquid. Stress in a viscoelastic material is a function of strain and the derivative of strain over time [30,37]. If these functions are linearly dependent on the strain and their derivatives, the material is called linear viscoelastic.

Viscoelastic material behavior leads to attenuation that is also known as material absorption. The material absorption in viscoelastic materials is commonly assumed to be linear dependent on frequency in the range of ultrasound frequency [37].

3.2.2 Geometric spreading

The spreading of the ultrasound wave attenuates the initial wave amplitude. The attenuation effect is independent of frequency. Geometric attenuation depends on the wave mode and the geometry of the investigated elastic body. Surface (Rayleigh) waves, for example, are attenuated by $1/\sqrt{r}$ with r as propagation distance. Plane longitudinal

wave amplitudes are attenuated by $1/r$, where r is the distance to the (point) source. This attenuation type is intrinsic in the wave equation. In a strict sense, geometric spreading is not counted to attenuation.

3.2.3 Scattering

The scattering attenuation in heterogeneous materials is caused by wave scattering at material (different phases) interfaces, mode conversion between longitudinal and transverse (shear) waves at these interfaces and diffraction effects.

Different domains are distinguished that have different approximations for the frequency dependence of the scattering attenuation coefficient depending on the ratio of wavelength λ to size of the scatterer B .

The attenuation coefficient introduced in equation 3.19 leads to attenuation of the initial wave amplitude with initial amplitude A_0 with distance z .

$$A(\lambda, z, B) = A_0 e^{-\alpha(\lambda, B)z} \quad (\text{Eq 3.23})$$

The coefficient is a function of the wavelength λ and the scatterer size B , It is the sum of the coefficients of the individual attenuation mechanism, absorption α_a and scattering α_s .

$$\alpha(\lambda, B) = \alpha_a(\lambda) + \alpha_s(\lambda, B) \quad (\text{Eq 3.24})$$

The absorption coefficient is defined with a medium-dependent constant C_a

$$\alpha_a(\lambda) = \frac{C_a}{\lambda} \quad (\text{Eq 3.25})$$

The scattering coefficient in Eq. 3.24 depends on the domain [25]. In the Rayleigh domain (wavelength much longer than size of scatterers) the form is found

$$\alpha_s(\lambda, B) = \frac{C_r * B^3}{\lambda^4} \text{ for } \lambda \gg B$$

(Eq 3.26)

In the stochastic domain (wavelength of the order of the size of scatterers) the following functional form is found

$$\alpha_s(\lambda, B) = \frac{C_s * B}{\lambda^2} \text{ for } \lambda \approx B$$

(Eq 3.27)

In the geometric domain (wavelength much smaller than size of scatterers) the following functional form is found.

$$\alpha_d(\lambda, B) = \frac{C_d}{B} \text{ for } \lambda \ll B$$

(Eq 3.28)

3.3 Short-time Fourier transformation (STFT)

A brief summary of the basic properties and formula of the used signal processing methods that exceed the standard discrete Fourier transform (DFT) techniques is given below.

The STFT of a function $s(t)$ is given by

$$S_{stft}(\omega, t) = \frac{1}{2\pi} \int_{-\infty}^{\infty} e^{-i\omega\tau} s(\tau)h(\tau-t)d\tau$$

(Eq 3.29)

where $h(t)$ is a window function. The energy density spectrum of an STFT is called spectrogram and is given by the square magnitude

$$E_d(\omega, t) = |S_{stft}(\omega, t)|^2 \quad (\text{Eq 3.30})$$

This means in words, that the STFT divides a time-domain signal into a series of small overlapping pieces; each of these pieces is windowed and then individually Fourier transformed.

Unfortunately, time-frequency representations (TFR) such as the spectrogram or the STFT suffer from the Heisenberg uncertainty principle. This restricts a TFR by making it impossible to simultaneously have perfect resolution in both time and frequency. Time and frequency resolutions are connected by the resolution inequality, respectively

$$\sigma_t^2 \sigma_\omega^2 \geq 0.25 \quad (\text{Eq 3.31})$$

Whereas σ_t and σ_ω are the standard deviations for time and frequency. For example, the product $\sigma_t^2 \sigma_\omega^2$ is equal to 0.2635 for a spectrogram that uses a Hanning window. A Gaussian window function satisfies the limiting case of Eq 3.28 with $\sigma_t^2 \sigma_\omega^2 = 0.25$, but the current application aims to alter the shape of the time signal as little as possible while avoiding discontinuities across the boundaries of the windowed signal. As a compromise, the Hanning window is chosen. The time-frequency resolution in a spectrogram is solely controlled by the window size and type. In contrast to the Wavelet time-frequency representations, the resolution is independent of frequency. Choosing a narrow window provides good resolution in time, but bad frequency resolution, whereas a wide window leads to better frequency resolution and worse time resolution.

CHAPTER 4

ULTRASOUND DIFFUSION APPROXIMATION

4.1 Introduction

Ultrasound wave field passing through a heterogeneous medium is scattered multiple times by scatterers in a medium, and can be field can be interpreted as a sum of a coherent ballistic field and an incoherent diffuse field (see [36]). The diffused part of the wave is strongly scattered by the media and is spatially incoherent, as well as incoherent with the source signal in time. The phase of this wave field is (approximately) randomized.

The ballistic part is on the other hand, is spatially coherent, as well as being coherent in time with the source signal. This part is either scattered in the forward direction or not scattered at all. Effective media theories and coherent potential approximation theories model the ballistic portion of the signal - where the amplitudes are significantly larger than the amplitude of the diffused part. In such instances the diffuse field contribution is neglected or ignored. Thereby, the effect of the attenuation caused by dissipation (actual energy loss) and scattering (spatial redirection) cannot be distinguished by these methods. Typically these ballistic theories lead to useful results for either small volume fraction of scatterers or long wavelengths compared to scatterer size (that is, low frequency), but breakdown in the strong scattering regimes. This regime is the focus of this research.

4.2 Diffusion approximation

The diffusion approximation was first developed in optics for randomly distributed scatterers (e.g. for colloid suspensions). Though the length scales of scatterers and wavelengths, impedance mismatches and wave speed differ strongly between applications in ultrasound acoustics and optics, the developed approximation provides a general model applicable to all types of waves (e.g. sound waves, elastic waves, electromagnetic waves). The advantage of studying the diffusion process in ultrasonics is the capability to directly measure the wave field instead of the field intensity, as it is done in optics.

If the phase information of diffuse ultrasound field is neglected (this is a reasonable assumption when the scattered wave has lost its temporal and spatial coherence after many scattering events), the diffusion approximation can be used to describe the propagation of strongly scattered waves over a long distance. A long distance in this context means travel paths that are long compared to scattering mean path (the mean distance between successive scattering events).

More complex transport equations have to be applied for shorter distances; these equations also serve as a starting point for the derivation of diffusion approximations (for theoretical coverage see [37]). It is a difficult task to exactly determine a travel distance that is sufficiently long, or the minimum number of scattering events that are needed for the diffusion approximation to hold. For instance, in the experimental setup of Becker et al [2] (also used in this research), the diffusion approximation is shown to be valid for distance at least 5-10 times the scattering mean path, but experiments and simulations with different configurations and experimental setups lead to ambiguous results. Most

research of the diffusion approximation is conducted in optics and fluid acoustics, but the transfer of the results from fluid acoustics to an elastic wave propagation is not a straightforward process. The main difficulty in this transfer is the additional wave modes (shear and longitudinal bulk waves) and coupling between these modes that occur in a solid but not in a fluid.

In the diffusion approximation, an energy velocity v_e – which characterized the propagation of the averaged energy density – can be identified (see section 4.3.4), that replaces the phase and group velocity known from classical wave propagation if the wave propagation becomes diffused.

4.3 Basic equation

The ultrasound diffusion approximation can be derived with either a random walk model (similar to the derivation of the heat transfer equation), or by statistical considerations of the Green's function approach and finding expressions for limiting cases. The formal derivation is available in [1]. Less theoretical and formal explanations are available in [37] and by Weaver [38]. Randomly distributed scatterers in elastic solid are assumed; a periodic distribution leads to resonance effects that are not included in the diffusion model. All scattering is assumed to be linearly elastic, that is no change in frequency from incident to reflected and transmitted waves takes place and no energy is lost by scattering.

The process of ultrasound diffusion in a body B is described by the second order parabolic partial differential equation (PDE). This PDE describes the time evolution of the spectral energy density (energy per frequency per volume).

$$\frac{\partial \langle E(x,t,f) \rangle}{\partial t} - D \Delta \langle E(x,t,f) \rangle + \sigma \langle E(x,t,f) \rangle = P(x,t,f) \quad \forall x \in B$$

(Eq 4.1)

$\langle E(x,t,f) \rangle$ denotes the spectral energy density (at time t and frequency f) at the point specified by the vector x , average over configurations of the random media. $P(x,t,f)$ is the spectral source energy density, D denoted the frequency-dependent diffusion coefficient and $\sigma > 0$ is the dissipation rate. The body is assumed to be isotropic, hence the diffusion coefficient does not depend on direction.

The operator $\langle \cdot \rangle$ is the expected value with respect to the different configurations of glass beads in the media (in a statistical sense, each configuration is one realization of the random media). Hence equation 4.1 predicts the ultrasonic spectral energy density in an average sense.

Equation 4.1 is similar to the well know heat transfer equations, but with an additional dissipation term – this result is reasonable, because this is based on energy considerations. The dissipation term does not change the basic structure of the solution and does not complicate the solution procedure. Therefore, the applicable approach is to determine specific solutions are similar. Heat transfer theory and solution of common problems are covered in [1].

For a solution of the partial differential equation 4.1, boundary conditions and initial conditions are needed. In the experimental setups considered in this research, almost no energy is transmitted form the elastic body (specimen) to the surrounding air because of high impedance mismatch for shear and longitudinal waves. Thus by energy considerations, boundary conditions are chosen analog to insulation conditions in heat

transfer. The gradient on the body surface δB has to be zero, which means no ultrasonic flux in the outwards direction in possible.

$$\nabla \langle E(x, t, f) \rangle = 0 \quad \forall x \in \partial B \quad (\text{Eq 4.2})$$

Initially zero ultrasound energy in the body leads to the initial conditions

$$\langle E(x, t, f) \rangle = 0 \quad \text{for } t = 0 \quad (\text{Eq 4.3})$$

4.3.1 Definitions

Some terms, commonly used in literature, are explained briefly in ([39], [40] and [41]).

- The transport free mean path l^* is the mean distance traveled before the propagation distance is fully randomized.
- The scattering free mean path l_s is the mean distance traveled before the wave is scattered.
- The energy velocity v_e is the average transport velocity of the ultrasonic energy, defined as the ration of energy flux to energy density [41].

4.3.2 Identification of the coefficients

The phenomenological coefficients in equation 4.1 have different physical meanings. Note that they generally depend on the frequency $\omega = 2\pi f$ of the diffuse ultrasound.

$\sigma(f)$ is the energy dissipation in the units of $\frac{1}{\text{time}}$. It must be positive. Dissipation

can be due to transformation of ultrasonic energy (kinetic and potential energy) to

heat, surface losses or by non-linear effects, which lead to the excitation of harmonics. Because elastic scattering is energy conserving, it does not influence the dissipation. The dissipation can be represented alternately as absorption (dissipation) time $\tau_0 = \sigma^{-1}$, after that 100% of initial energy decreases to 63% if only dissipation takes place [39].

$D(f)$ denotes the diffusion coefficient, which has units of $\frac{\text{length}^2}{\text{time}}$. D depends on the material microstructure. The higher D is, the faster the diffusion takes place. The lower D is, the slower the ultrasound energy is transported away from the energy source. If the diffusion approximation is derived with the random walk approach, the parameter D is identified as $D = \frac{1}{3} v_e l^*$ with v_e and l^* defined corresponding to section 3.2.1 (see [40]). This representation can be useful if one is interested in the energy velocity v_e , that replaces the well-known group and phase velocity in a strongly scattering media with diffuse field [41].

4.3.3 Special solutions of the diffusion equation

Multiple special case solutions of the (heat) diffusion equation is found in [1], and some of them relevant to this research have been discussed by Becker et al [2, 3]. In the following section, for reason of simplicity and understanding, the frequency dependence of the coefficients $\sigma(f)$, $D(f)$ and the spectral energy density $\langle E \rangle$ is omitted.

One-dimensional bar

Equation 4.1 is solved with for a one-dimensional bar with impulse excitation $P(x,t) = P_0\delta(t)\delta(x)$. The thickness of the bar is t , and is assumed to be much less than the length of the bar, L . In this case, the problem is treated as one-dimensional energy diffusion, neglecting the wave propagation perpendicular to the length of the bar (x axis). The simplified form of the PDE is thus as shown below:

$$\frac{\partial \langle E(x,t) \rangle}{\partial t} - D \frac{\partial^2 \langle E(x,t) \rangle}{\partial x^2} + \sigma \langle E(x,t) \rangle = P(x,t)$$

(Eq 4.4)

with boundary conditions defined by

$$\frac{\partial \langle E(x,t) \rangle}{\partial x} = 0 \text{ at } x = 0$$

(Eq 4.5)

The solution of this equation is given by

$$\langle E(r,t,f) \rangle = \frac{1}{4} \frac{P_0 e^{\left(\frac{1}{4Dt}\right)} e^{(-\sigma t)}}{\sqrt{\pi Dt}}$$

(Eq 4.6)

The advantage of working with this solution is the linear form of the logarithm of this solution is easy to work with, especially for linear regression and finding values of coefficients.

Two-dimensional plate

Similar to a one-dimensional plate, the PDE in equation 4.1 is solved with the following boundary conditions.

$$\frac{\partial \langle E(x,t) \rangle}{\partial x} = 0 \text{ at } x = 0 \text{ and}$$

(Eq 4.7)

$$\frac{\partial \langle E(y,t) \rangle}{\partial y} = 0 \text{ at } y = 0$$

(Eq 4.8)

Here again, the plate thickness is assumed to be negligible compared to the length and width dimensions of the plate, which are infinitely long. A closed form solution is obtained from this PDE, which is shown below.

$$\langle E(r,t,f) \rangle = \frac{1}{4} \frac{P_0 e^{\left(\frac{1-x^2+y^2}{4Dt}\right)} e^{(-\sigma t)}}{\pi Dt}$$

(Eq 4.8)

In this equation, we can rewrite $x^2 + y^2$ as r^2 to show that this solution is radial symmetric. Becker et al [2] uses this solution to approximate the energy diffusion process in circular specimen of different thicknesses b and varying volume fraction of glass beads. It is anticipated that the dissipation losses are only due to the matrix phase and not the glass media. Becker et al mentions that the dissipation in equation 4.1 has to depend on the amount of matrix paste in the specimen.

Circular disc of radius R

To solve the diffusion equation for a thin disc of finite radius R , equation 4.1 is first expressed in cylindrical coordinate system. The Laplacian differential operator in cylindrical coordinate system is expressed as:

$$\Delta E = \frac{1}{\rho} \frac{\partial}{\partial \rho} \left(\rho \frac{\partial E}{\partial \rho} \right) + \frac{1}{\rho^2} \frac{\partial^2 E}{\partial \phi^2} + \frac{\partial^2 E}{\partial z^2}$$

(Eq 4.9)

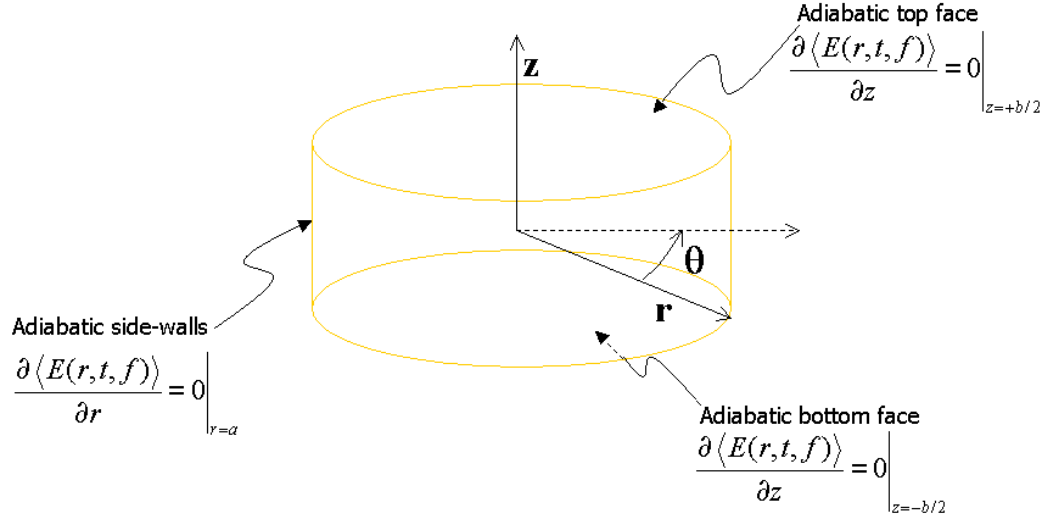


Figure 4.1: Cylindrical coordinate system and boundary conditions on circular disc

As shown in [1], equation 4.1 is rewritten with the cylindrical Laplacian operator to arrive at a non-linear and radial symmetric PDE in the new coordinates of r and z .

$$\frac{\partial \langle E(r,t,z) \rangle}{\partial t} - D \left(\frac{1}{r} \frac{\partial}{\partial r} \left(r \frac{\partial \langle E(r,t,z) \rangle}{\partial r} \right) \right) + \frac{\partial^2 \langle E(r,t,z) \rangle}{\partial z^2} + \sigma \langle E(r,t,z) \rangle = P(r,t,z) \quad (\text{Eq 4.10})$$

In this case, the height of the cylinder is negligible compared to the radius, so that there is no variation of flux along z direction. The boundary condition is defined as adiabatic conditions on the radial periphery of the disc.

$$\frac{\partial \langle E(r,t,z) \rangle}{\partial r} = 0 \text{ at } r = R \quad (\text{Eq 4.11})$$

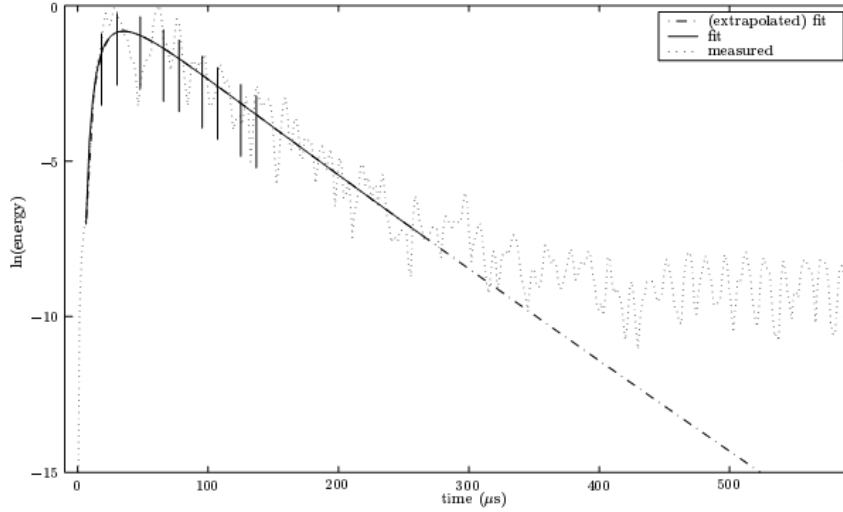
and that the solution for $\langle E(r,t,z) \rangle$ has to be finite at $r=0$. The analytical solution to this equation is an infinite series involving Bessel functions.

$$\langle E(r, t, f) \rangle = \frac{P_0}{\pi R^2} \left(1 + \sum_n \frac{e^{(-Dt\alpha_n^2)} J_0(r\alpha_n)}{J_0(R\alpha_n)^2 + J_1(R\alpha_n)^2} \right) e^{(-\sigma t)} \quad (\text{Eq 4.12})$$

where, J_0 and J_1 denote the Bessel functions of the first kind and first order, and α_n are the positive roots of the equation

$$J_1(R\alpha) = 0 \quad (\text{Eq 4.13})$$

Although equation 4.12 is more suitable to be used for the experiments on circular discs, the complex analytical form makes it difficult to apply curve fitting to derive the diffusion coefficients from the experimental data. Becker et al uses equation 4.8, solution for two-dimensional plate, for curve fitting on experimental. Due to the simplicity of the equation, particularly its linear form after taking logarithmic on both sides, the curve fitting process as well as the error estimation is more practical and solvable. Becker's research characterizes cement-based materials with diffused ultrasound, and quantitatively measures dissipation and diffusion coefficients as functions of frequency and microstructure. As shown in figure 4.2, the diffusion coefficient of the material is obtained from the slope of the plot of spectral energy density with time.



(b) $f_c = 0.6$ MHz

Figure 4.2: Curve fit for 3mm loose specimen with expected deviation as bars [2]

4.3.4 Comparison of diffusion model for infinite and finite discs

While equation 4.8 is useful to measure the value of the diffusion and dissipation coefficient, it does not serve as an approximation to the actual diffusion process in a finite disc. The discs used by Becker et al in [2] have a diameter d to height h ratio of approximately 7. Since equation 4.8 is a limiting case of $d \gg h$, the predicted value of $\langle E(r, t, z) \rangle$ is seen to fall off much more rapidly than when is observed in the experiment. It is assumed that due to the finite size of the plate, most of the energy is contained in the body as time progresses, unable to diffuse to higher radius as predicted by equation 4.12. Thus, as illustrated in the figure 4.3, the increasing deviation between the predicted and actual energy dissipation in the disc can be attributed to its finite size and adiabatic boundary.

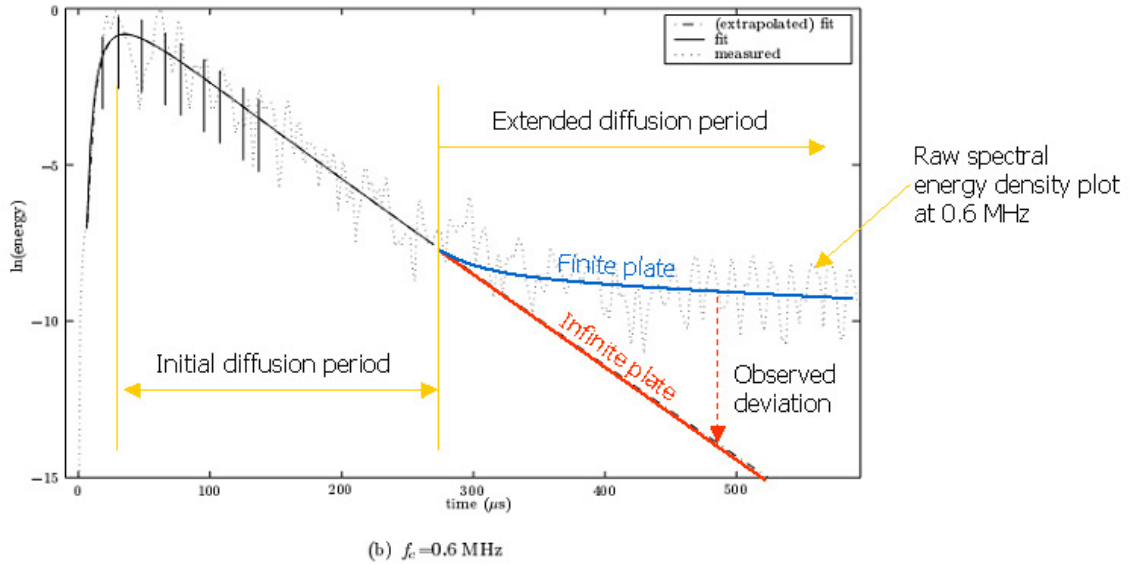


Figure 4.3: Predicted and observed variation of spectral energy density with time

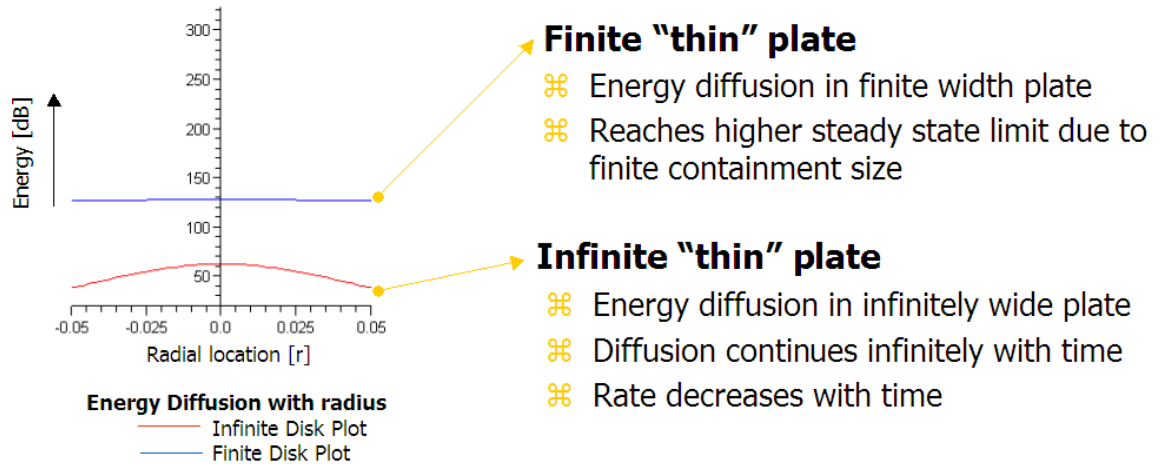


Figure 4.4: Theoretical plot showing the higher residual energy in a finite disc, as compared to an infinite plate of same negligible thickness

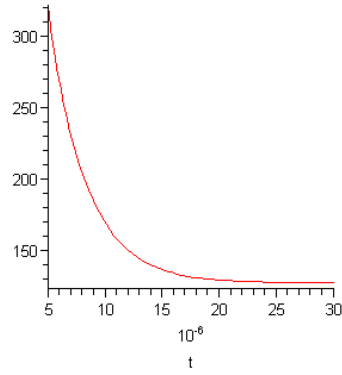


Figure 4.5: Theoretical estimate of decay of spectral energy density with time

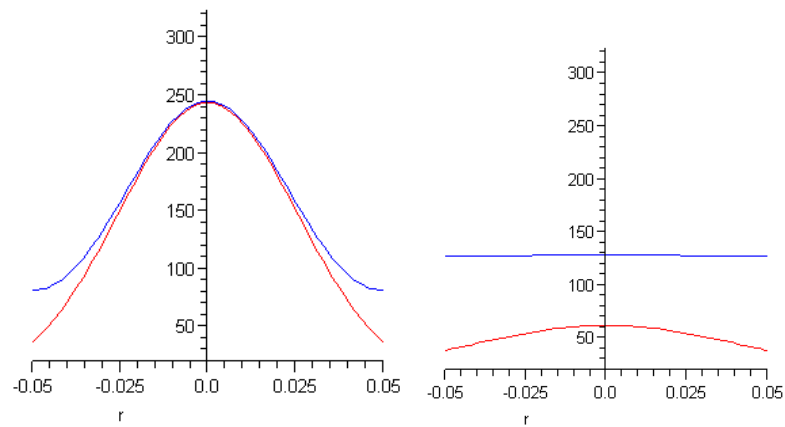


Figure 4.6: Comparative estimates of spectral energy density at $t=5 \times 10^{-6}$ s (left) and at $t=30 \times 10^{-6}$ s (right) for assumed value of R (Infinite disc – red. Finite disc – blue)

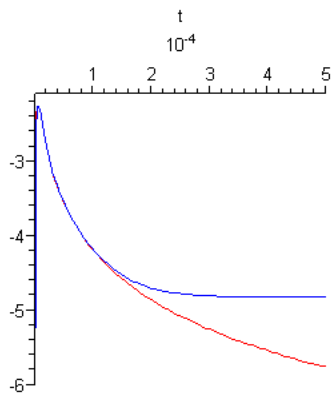


Figure 4.7: Theoretical estimate of decay of $\ln \langle E(r, t, z) \rangle$ with time for infinite disc (red) and semi-infinite disc (blue)

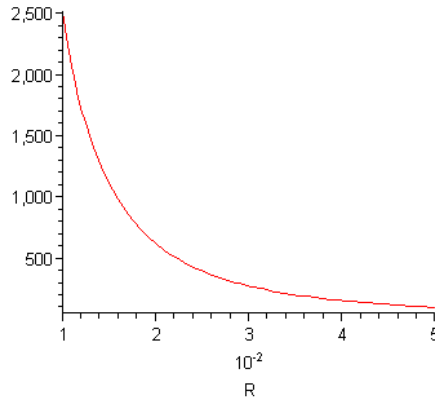


Figure 4.8: Theoretical estimate of residual spectral energy density at near steady-state time ($t=5 \times 10^{-2}$ s) vs. radius of disc

The energy decay in a finite plate or disc is more gradual due to the finite dimensions and adiabatic boundaries. As observed from equation 4.12, this is indeed exhibited in plots indicating the change of $\langle E(r, t, z) \rangle$ with time as in figure 4.5 and 4.6. In these plots, the red line shows the initial energy with time in an infinitely wide disc, while the blue line indicates the same for a finite disc of radius R .

4.4 Effects of Specimen Geometry on Ultrasound Diffusion

Due to the finite size of the discs used in experiments, ultrasound energy is contained within the body for a longer period of time, as compared to [2]. Though the energy content of the disc in reality would eventually decay to zero, due to leaks and other mechanisms, a theoretical study of perfectly adiabatic case is useful to compare the residual energy values to material properties. As a particular example, the input energy sees multiple phenomena inside the material during propagation. The residual energy is thus a combined effect of the multiple scattering, dissipative and diffusive processes.

In this research the relationship between the residual spectral energy density and specimen geometry is studied, with added interest to attribute the differences in the residual spectral energy density values in materials of similar geometry to the varying material properties of the heterogeneous materials.

CHAPTER 5

EXPERIMENTAL PROCEDURE AND SIGNAL ANALYSIS

Although most of the data used in this research are from Becker et al [2, 3], a brief explanation of the experimental setup is provided for better understanding of the process, input and noise parameters. The intention is also to use this setup to collect new data, gain familiarity with the system and validate the signal acquisition process. This also helps in drawing logical inferences from comparison of the results with relation to the infinite and finite disc approximations.

5.1 Signal generation and amplification

The objective of efficient signal generation and amplification is to provide a pulse or monotone sine-burst signal to the cement specimen, and be able to receive the response across the thickness of the specimen, with a off-center probe kept 30 mm radially away from the epicenter of the specimen. The specimens have multiple glass bead scatterers, which have high acoustic impedance mismatch, and causes sufficient scattering and dissipative losses.

5.1.1 Function generator

In this research only monotone sine functions are generated using WaveTek Model 81 function generator, used along-with ENI 240L RF high-power amplifier that provides a peak-to-peak voltage of 200V to the source transducer. The signal type, frequency, amplitude, number of cycles (burst) and repetition time of the generated signal can be selected.

5.1.2 Pulse generator

A Panametrics 500 PR impulse generator is used to provide source signal for the experiments that require an impulse source. When set to high mode, this device generates pulses of 210V and when set to low amplitude of 110V. The manufacturers specification of pulse bandwidth is 25MHz. The pulse repetition frequency (PRF) can be varied between 500-5000 pulses per second. In the experiments, a PRF value of 1 kHz is used. A damping parameter (D) can be set and is called the damping factor of the pulse. This determines the duration of the decay from peak to 0V. The impulse generator generates a +5V rectangular SYNC signal, which is used to trigger the signal acquisition in the oscilloscope.

5.2 Received signal amplification

As mentioned earlier, the high attenuation of ultrasound in cement-based specimens used for the experiments requires amplification of the input energy, as well as of the received signal. Following setup explained by Becker et al [2, 3], a low power amplifier integrated into the Panametrics impulse generator is used. One of the major drawbacks of this is the crosstalk introduced in the received signal due to high-amplitude pulse generation. This is somewhat avoided by clipping the front portion of the signal manually while analyzing the data, since both the pulse and SYNC signals are available and captured through the oscilloscope, apart from the output signal. Becker et al also mentions about an automated process for doing the same by clipping finite range of signal around 0 ms, since the crosstalk happens before any real signal arrives.

5.3 Source/receiver selection

Several piezoelectric transducers have been tested in [2] for their effectiveness by with respect to their bandwidth, flatness of the frequency response, absolute frequency range and their active surface size. Based on the available literature on the transducers and experiments by Becker et al, the following observations are listed in [3].

1. Ultrason KC50-2 and LC50-2 (effective diameter 12.5mm)

“Nominal frequency of the KC50-2 and LC50-2 transducers is 2 MHz. The K type is a narrow band transducer, whereas the L type is a broadband type. Based on the given information by the manufacturer [42], the sensitivity (ratio of ultrasonic output power to electric input power) of the K transducer at the center frequency is 6.3 times higher than those of the L type (-24 dB versus -40 dB sensitivity).”

2. Digital Waveform (DW) B1025 (effective diameter 8 mm)

“This broadband transducer is mainly designed for acoustic emission measurements. It has a significant backing and a relatively small effective surface area.”

3. Pad transducer: modified DW B1025 (2mm square pad)

“The DW B1025 transducer is modified to obtain a point-like detector when the broadband response. A thin foil pad is put between the measurement point and transducer surface to approximate a point-like transducer. This results in a broadband efficiency curve. Corresponding to the wave propagation theory in layers, the pad reflections can be neglected if the pad has an approximate thickness $t < \lambda/8$ (in this case the pad just acts as an acoustic delay). The

longitudinal wave speed of the plastic foils is known to be roughly 2700 m/s, the thickness t is 0.14 mm. Therefore, the pad can be neglected up to a frequency of $f_{\max} = 8 \frac{c_L}{t} = 2.4 \text{ MHz}$, which covers the entire bandwidth considered in this research. The small contact pad area leads to low signal amplitudes and difficulties in proper alignment. To enable consistent alignment, a special template design (see Becker [3]) fixes the position of the receiver on the surface and keeps the transducer orientation perpendicular to the surface – this ensures that the transducer edge does not come in contact with the specimen. It is important for consistent measurements that the pad is always carefully centered on the transducer surface after every transducer movement. Attempts to glue the pad to the transducer surface with Phenyl Salicylate were not successful. This glue is reversible under heat, but its strength is sufficient if the transducer is frequently moved.”

4. Pin-transducer (Valper-Fisher)

“Pin-transducers are commonly used in applications where a small transducer contact areas (point-like detection) is required. The response of these pin-transducers are examined for their suitability in this research, but these experiments shows a poor response in important parameters for this research. Their main disadvantage is the strong ringing (very narrow-band efficiency) and their strong dependence on obtaining perfect perpendicular orientation to the specimen surface. Pin-transducers are not used in this research for these reasons.”

A broadband source provides the capability of producing pulse like signals with small ringing effect, as compared to any other narrowband source. It also provides a suitable means to cover a large frequency range for experiments. The LC50-2 is chosen as a suitable source since it provides high efficiency and higher bandwidth relative to the DW B1025 transducer, which is favorable for measurements with these high-attenuating materials.

On the detection side, the point-like DW B1025 transducer is used for the measurements of the diffusion approximation, because of the high sensitivity, small footprint and broadband pickup.

5.4 Source/receiver configuration

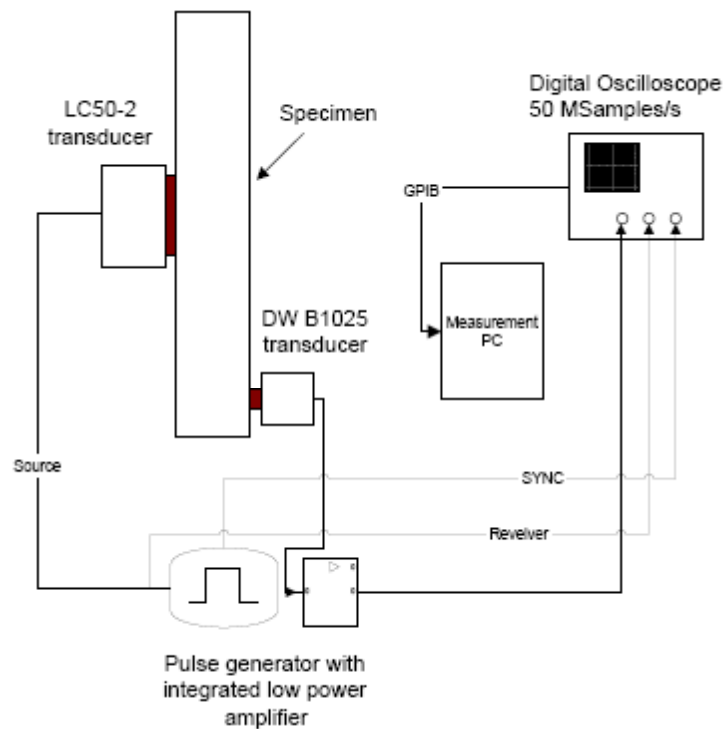


Figure 5.1: Experimental setup design by Becker et al [2]

The objective of the experiments by Becker et al [2] was to experimentally obtain the diffusion and dissipation coefficients for the concrete specimens. Therefore, to avoid the effect of the ballistic portion of the signal on the receiver in through-transmission mode, it is placed approx 30mm from the center of the specimen, where the source is located. Multiple measurements are taken around the specimen as stated, with this source-receiver distance being kept as constant as possible. A schematic of the experimental setup as found in [2] is shown in figure 5.1 and is self-explanatory in showing the relative positions of the transducers. Although, theoretically there is some contribution of the ballistic beam on the receiver, we consider it to be negligibly small to be noticed in this research.

5.5 Waveform acquisition

A four channel digital Tektronix TDS 420 or TDS 420A oscilloscope with extended memory is used in this research. Three channels are used for sampling and recording the excitation, the SYNC and received pulse signals. This model provides a sampling rate of upto 200 MHz, which is required to measure the short pulses generated by the impulse generator. Also, a 10 MHz passive low-pass filter is used to suppress high frequency noise. The cut-off frequency is well above the range of all used transducers of 0 – 5 MHz. The oscilloscope provides capability to directly store waveforms as Matlab data files, which are easily transferred for further processing.

5.5.1 Signal-to-noise ratio (SNR) and averaging

Since most of the data in this research is originally captured by Becker et al as shown in [2], it is important to note that the measurements are taken at 30mm offset from the center of the specimens to avoid the ballistic portion of the wave-front. However, this

also means that the signals have low amplitudes and suffer from low signal-to-noise-ratio (SNR). To help improve the SNR, the averaging function in the oscilloscope is used and every stored waveform is taken as an average of around 700 individual signals. This averaging decreases the noise power levels by 26 dB – 30 dB, which is very important in the measurement of small diffuse ultrasound signals.

5.5.2 Sampling rate and record length

As explained by Becker et al [2] – “to obey the sampling theorem, the sampling rate must exceed at least twice the highest frequency in the specimens analog signal to prevent frequency aliasing [33]. The measured signals are filtered with a 10 MHz analog low pass filter and specimens with a frequency f_s of 50 MHz. Because this research is mostly interested in the incoherent field (as well as the coherent field), the long “tails” of the scattered waves has been recorded. Therefore scopes with special memory extension are used, which allow one to specimen up to $n = 60000$ points, although the data handling gets more cumbersome. This record length and the sampling rate selected correspond to a time period of 1.2 ms, including the pre-trigger. Note that the signal before the trigger event is needed to determine the noise level of the measurements – typically the recorded signal time period before the trigger is about 10% of the full length.” During the initial experiments in this research, the same sampling rate is used for consistence in the measurements and analysis.

5.6 Cement-based aggregate specimens

5.6.1 Description

The data analyzed in this research is based on the specimens designed and developed by Becker et al [2]. To quote his report – “a summary of the cement-based specimens is given in Table 5.1. Cement based specimen are made with two sizes of glass beads that are mixed with cement paste and cast in circular molds. The cement paste is a mixture of Portland type I cement and water with a water/cement ratio of 0.4, the water has a *NaOH* concentration of 0.4 mol/l. 1.03% NaO_2 equivalent of lithium is added to the mixture – the lithium is added to prevent cracking because of the alkali-silica reaction (ASR). The paste specimen has no lithium added. All specimens besides the paste specimen are made from one cement-paste batch. The embedded glass beads are made of borosilicate glass. Similar glass beads are used in research in optical monitoring of cracking and damage due to alkali-silica reaction at the glass/paste interface [43]. All specimens have the same circular shape but different thickness. It is important for later interpretation and discussion of the measurements, that all specimens (besides the paste specimen) have the same absolute amount of cement paste matrix material. The volume fraction is calculated by dividing the glass volume, which is determined by the weight of the beads and the glass density, by the specimen volume, which equals the product of the circular area and the average thickness.

The surfaces of the cement-based specimens are well polished. All specimens have a circular shape with a diameter of about 76 mm and a thickness of 14 to 16 mm. Unfortunately some specimens have thickness variations from one edge to the other of as

much as 2 mm – Table 6.1 shows their minimum and maximum thickness values. The specimens are aged for at least 30 days, before experiments are carried out initially.

The glass beads represent the scattering aggregates in real cement-based materials, like sand or gravel, but with a simplified spherical shape. The mechanical properties of the glass beads and the cement paste are summarized in Table 5.1. The impedance mismatch of glass balls and cement paste is similar to that of real cement-based materials, if one assumes a perfect interface.”

5.6.2 Impedance mismatch

Following the laws of physics, and as mentioned in Chapter 1, an incident ultrasound wave is separated into a reflected and transmitted wave at the interface between the media with different impedances. In this application, this means that some energy of the incident wave is reflected at the glass interface and the other part is transmitted.

$$Z_1 = Z_{paste} = 6.848 \times 10^6 \text{ kg/m}^2\text{s}$$

$$Z_2 = Z_{cement} = 1.248 \times 10^6 \text{ kg/m}^2\text{s}$$

The values of the reflection and transmission coefficients can be easily calculated from the following relationships.

$$R = \frac{Z_2 - Z_1}{Z_2 + Z_1} \quad -1 < R < 1 \tag{Eq 5.1}$$

$$T = \frac{2Z_2}{Z_2 + Z_1} \quad 0 < T < 2 \tag{Eq 5.2}$$

For the given Z_1 and Z_2 , the coefficients for the paste/glass combination are calculated.

$$R = 0.29$$

$$T = 1.29$$

Thus, we note from the values above that ultrasound waves travel through both the materials. The glass beads are sparse, and generally have no contact with each other. Hence each wave has to travel a significant distance in the paste. Becker et al mentions in [2] that the “bulk wave speeds in glass are higher than in the paste matrix, which leads to two contrary effects in case of an increase in scattering. On one hand, the average speed increases if there are more scatterers in the travel path, because the mean travel path length in glass is higher, but on the other hand more wave energy is scattered out of the forward direction that leads to longer travel paths for these out-of-direction scattered portions.”

5.6.3 Microscopic examination of the specimen

Table 5.1: Results of microscopic examination of the specimens

| Sample Type | Observation |
|-------------|--|
| Paste | No cracks |
| 1 mm loose | Almost no cracks |
| 1 mm medium | Almost no cracks |
| 1 mm dense | Some cracks beginning to form, lots of air bubbles |
| 3 mm loose | Very long cracks between beads, far less than 3D |
| 3 mm dense | Lots of cracks, always between beads |

The presence of beads in the cement specimens is known to cause some cracking in them. The paste specimen on the other hand (because of lithium addition), should have

only very limited cracking. Optical microscopy examination of the specimens provides a comprehensive picture of the actual damage accumulation in them. A summary of the results is provided in table 5.1. The paste specimen shows no visible cracking at all. A typical picture of a crack that connects the aggregates (beads) in a 3 mm specimen is shown in figure 5.2. A picture of a 1 mm bead specimen with smaller cracks is presented in figure 5.3. Thus, in line with expectations, the specimens with larger and increasing volume fraction of the aggregates show progressively more damage accumulation in the form of cracking.

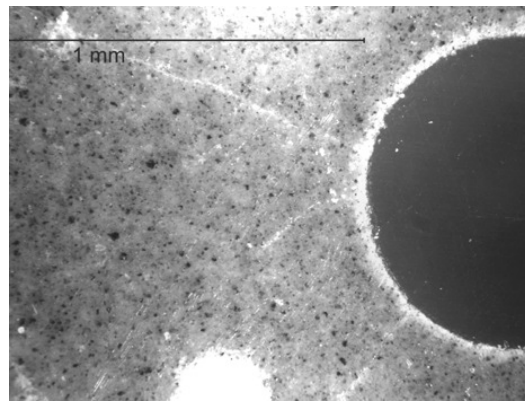


Figure 5.2: Matrix/bead interface cracks in 3 mm dense specimen

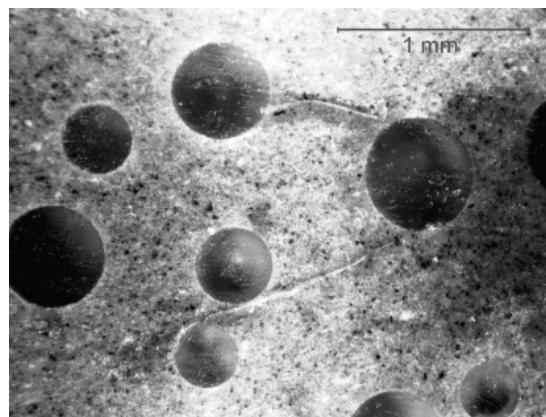


Figure 5.3: Surface cracks in 1 mm medium specimen

CHAPTER 6

EXPERIMENTAL RESULTS

6.1 Introduction

As discussed in Section 4.3.4, due to the finite size of the discs used in experiments, ultrasound energy is contained within the body for a longer period of time, as compared to an infinitely wide plate. Though the energy content of the disc in reality would eventually decay to zero, due to leaks and other mechanisms, a theoretical study of perfectly adiabatic case is useful to compare the residual energy values to material properties. As a particular example, the input energy sees multiple phenomenon inside the material during propagation. The residual energy is thus a combined effect of the multiple scattering, dissipative and diffusive processes. The basic set of experimental data acquired by Becker et al in [2, 3] is used in this research for a fair comparison of the finite and infinite disc's energy evolution hypothesis. A summary of the data processing techniques and important observations are given in the following sections.

6.2 Signal processing and data analysis

A snapshot of the cement based aggregate specimens used in this research and their properties are shown in table 6.1. The number of experimental waveforms acquired for each of these specimens is graphically shown in figure 6.1. All the acquired waveforms have a specimen rate of 50 MHz and have around 60000 points per acquisition, as explained in section 5.5.2. A typical snapshot of the ultrasound response is shown in figure 6.2. Since the rate of diffusion is quite different across the various specimens, and even some of the experimental attributes change from one acquisition to

another, it is important to pre-process the data to allow final comparisons, averaging and trend analysis between the various datasets.

Table 6.1: Details of specimens used in the experiments

| Sample | Min Thick | Max Thick | Mean Th | Bead dia | Volume Fraction |
|-------------|-----------|-----------|-----------|-----------|-----------------|
| | <i>mm</i> | <i>mm</i> | <i>mm</i> | <i>mm</i> | % |
| Paste | 15.5 | 16.5 | 16 | 0 | 0 |
| 1 mm loose | 12.7 | 13.1 | 12.9 | 1 | 22 |
| 1 mm medium | 14.3 | 15.5 | 14.9 | 1 | 32 |
| 1 mm dense | 15.5 | 16 | 15.75 | 1 | 41 |
| 3 mm loose | 12 | 12.9 | 12.45 | 3 | 22 |
| 3 mm medium | 14.1 | 16.1 | 15.1 | 3 | 32 |
| 3 mm dense | 16.5 | 17.5 | 17 | 3 | 41 |

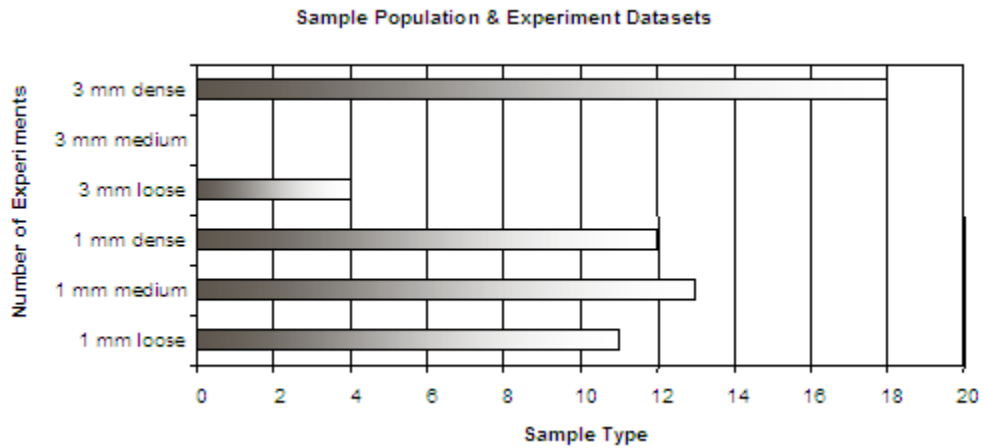


Figure 6.1: Number of waveforms analyzed for various specimens

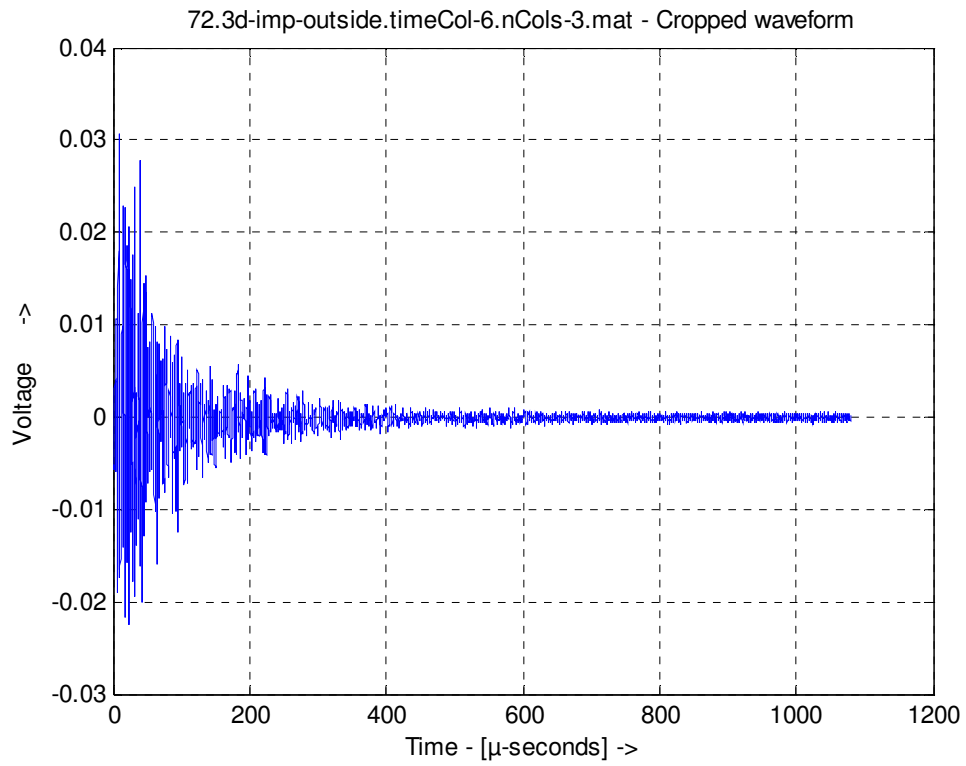
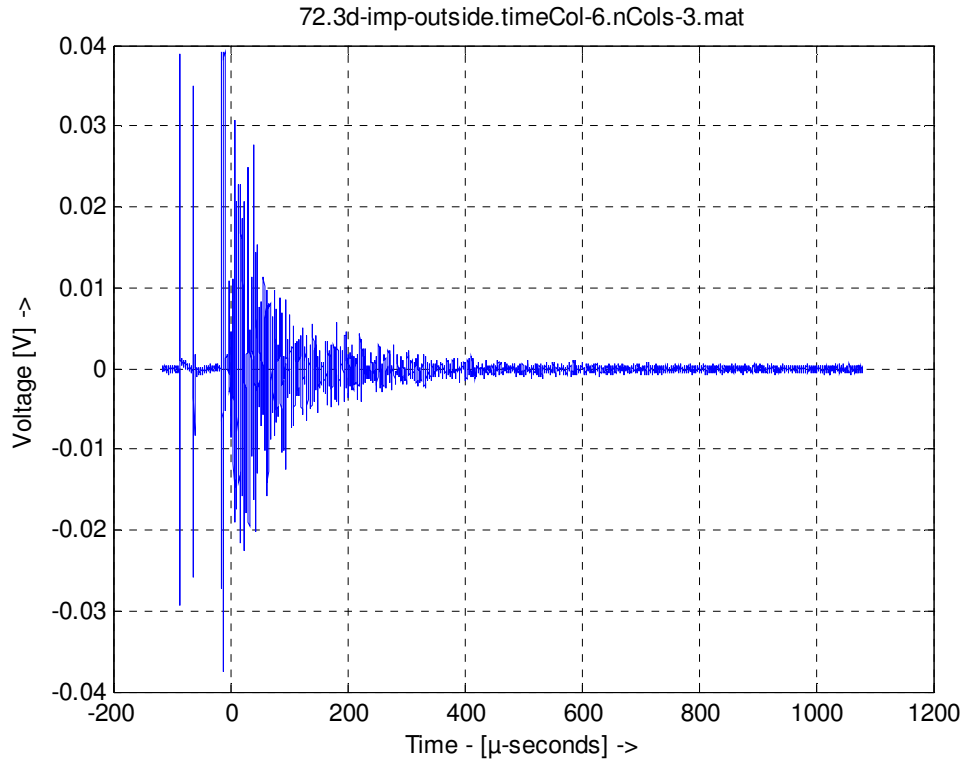


Figure 6.2: Typical response waveform – raw and cropped (1 mm dense specimen)

All the measurements are taken 30 mm off the epicenter on the other side of the specimen (away from the source). As mentioned in Becker et al [2, 3], adequate separation of the ballistic component of the signal is ideally obtained by taking off-center measurements around the specimen, and subtracting the same from the ballistic signal. However, this required a large number of detection points and all averaged signals needs to be measured in a consistent fashion. Transducer coupling introduces inconsistencies that make this approach difficult to apply.

6.2.1 Signal pre-processing

As discussed in section 5.5.2, all the waveform data obtained through experiments is an average of roughly 700 individual waveforms. This automatically removes some of the random noise elements associated with single measurements. However, to be able to compare the waveforms across various specimens, they need to be adequately registered with respect to their time coordinate. Becker et al clips the initial $1.5 \mu s$ of the signal relative to the pulse trigger time $t = 0$ to avoid crosstalk. He uses the beginning of the rest of the waveform to find the diffusion coefficient D , and latter part of the signal to compute the dissipation coefficient from the slope of the energy evolution curve at various frequencies. Since the focus of this research is to primarily look at the dissipation effects, all the individual waveforms are individually cropped starting from their time of maximum wave amplitude, to be able to better register the waveforms with one another. An example of raw and cropped waveforms is shown in figure 6.2. Some of the raw data (cement paste specimen) shows very fast dissipation, and Becker et al has used higher pulse repetition frequency during the experiments. For this reason, this data is cropped

from the right so as to avoid the effect of a second input pulse creep into the analysis and results.

6.2.2 Spectral energy density

Most of the steps followed for determining the spectral energy density $\langle E(r, t, f) \rangle$ are followed from Becker et al [3]. Although a detailed explanation of the steps and parameters is given in his doctoral dissertation, a brief outline is provided below as a reference.

The spectral energy density or spectrogram is the frequency spectrum of the average energy for a frequency band (centered around f_c), and plotted in time domain to show the evolution of the energy with time. Physically, it shows how the energy content within a frequency band around f_c changes with time. Mathematically, a Hanning window is used to average the waveform to obtain a Fourier spectrum around f_c . The width of this window is related to the frequency resolution of the spectrogram. The time signal is also artificially divided into block of $\Delta t = 500$ points, which acts as a threshold for the temporal resolution of the spectrogram. By following the parameters detailed by Becker et al, we obtain a sufficient time and frequency resolution for efficient comparison of the energy content of the signal across various frequencies, as well as adequately follow its evolution with time. Figure 6.3 shows typical plots for spectral energy density (in green) for 1 mm dense beads specimen at six different frequencies. For ease of visual representation and parameter estimation, the logarithmic of spectral energy density is used throughout this research – represented by $\ln \langle E(r, t, f) \rangle$.

6.2.3 Spectral energy density evolution

The evolution of the spectral energy density provides a good estimate of the material dissipation coefficient for the specimens. For this purpose, Becker et al [2] fits a log-linear approximation to the initial portion of the falling spectral energy density values and reads the dissipation coefficients from the slope of the straight line thus obtained. The focus of this research however is to look at the extended portion of the spectral energy density values and look at the effect of finite containment of this energy. For this reason, a cubic fit is applied to the spectral energy density values along the entire time axis to obtain an approximation of an “extended” dissipation curve.

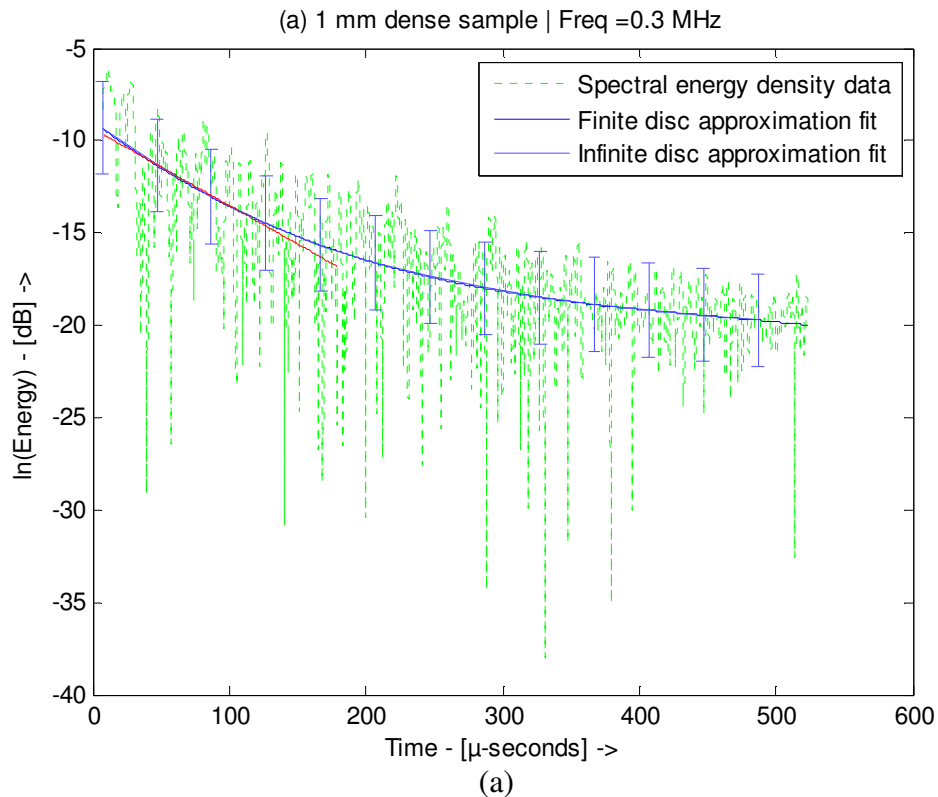
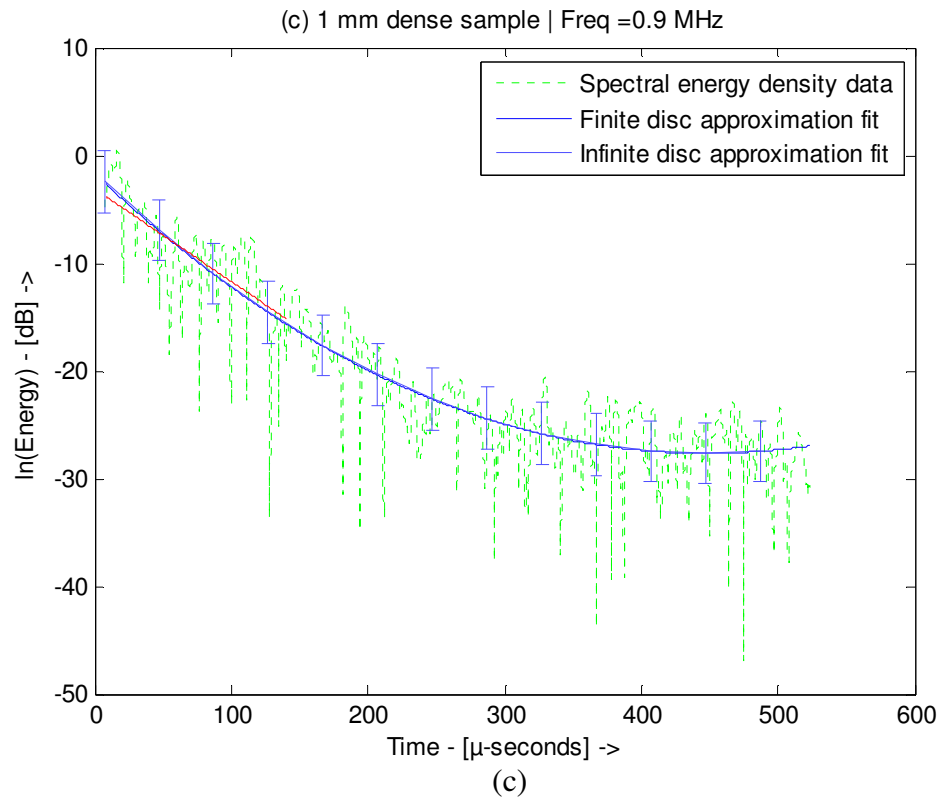
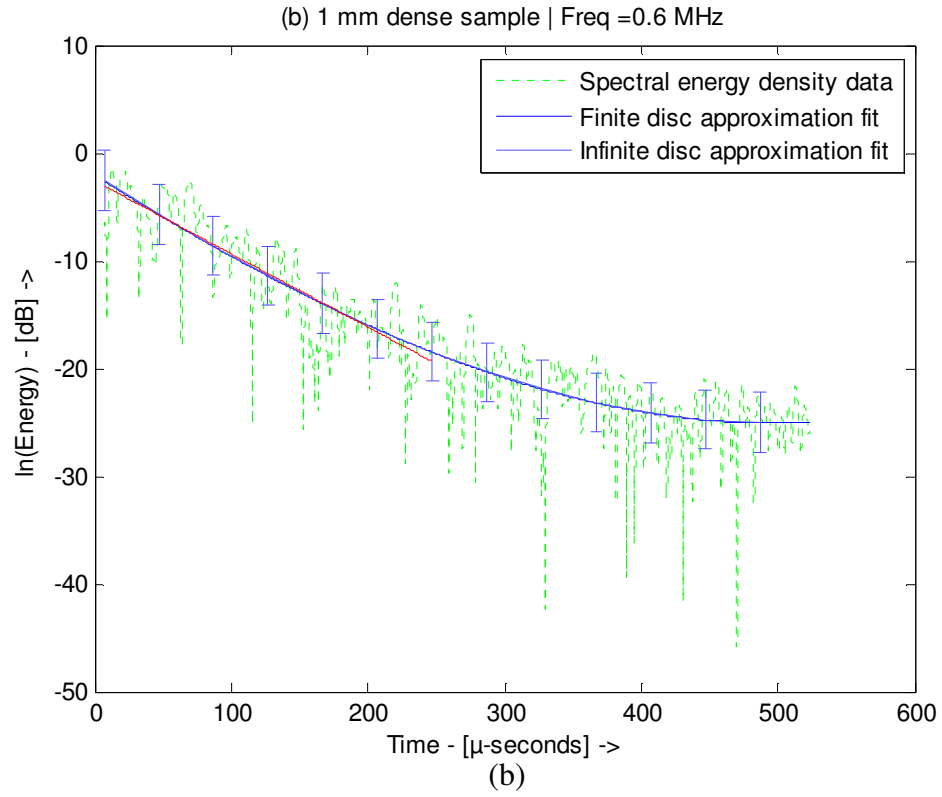
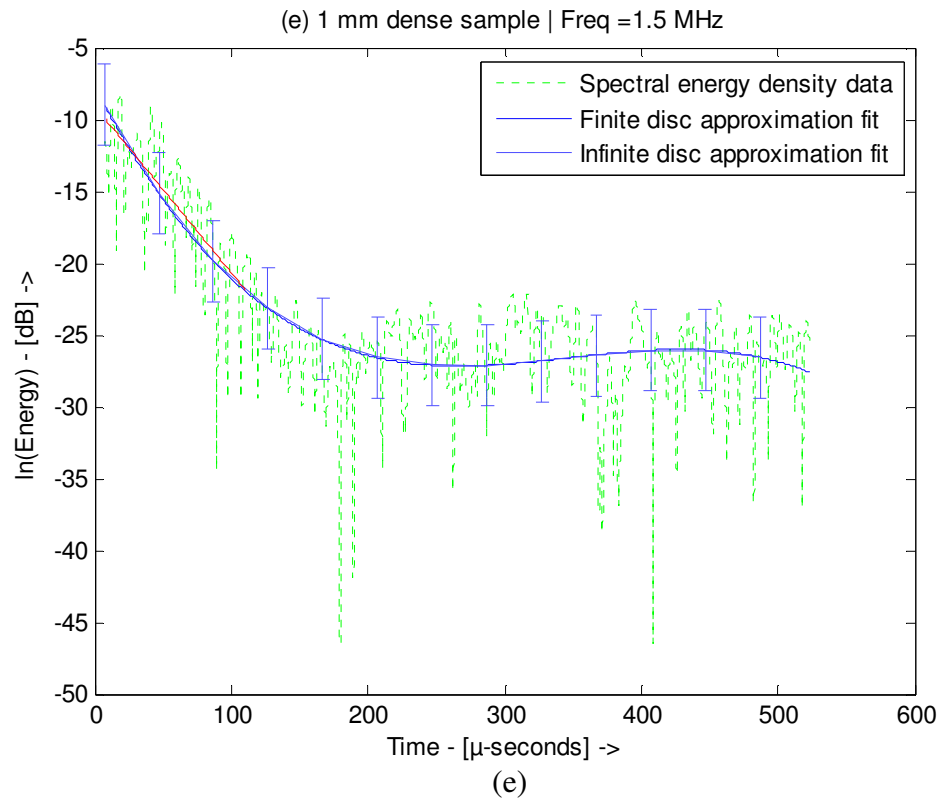
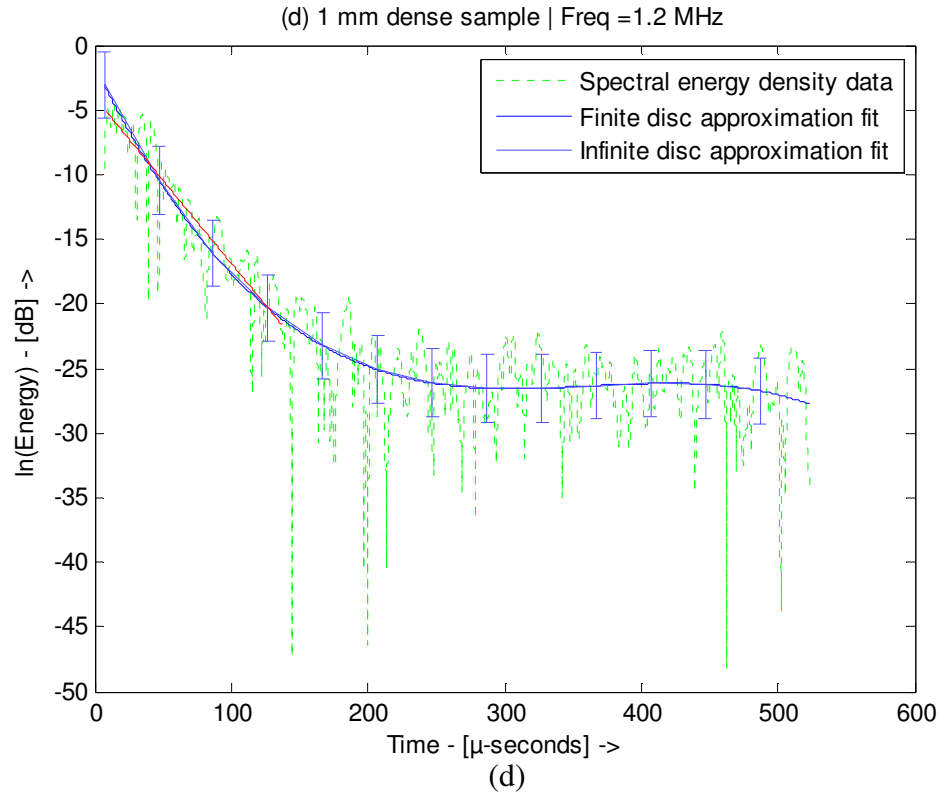
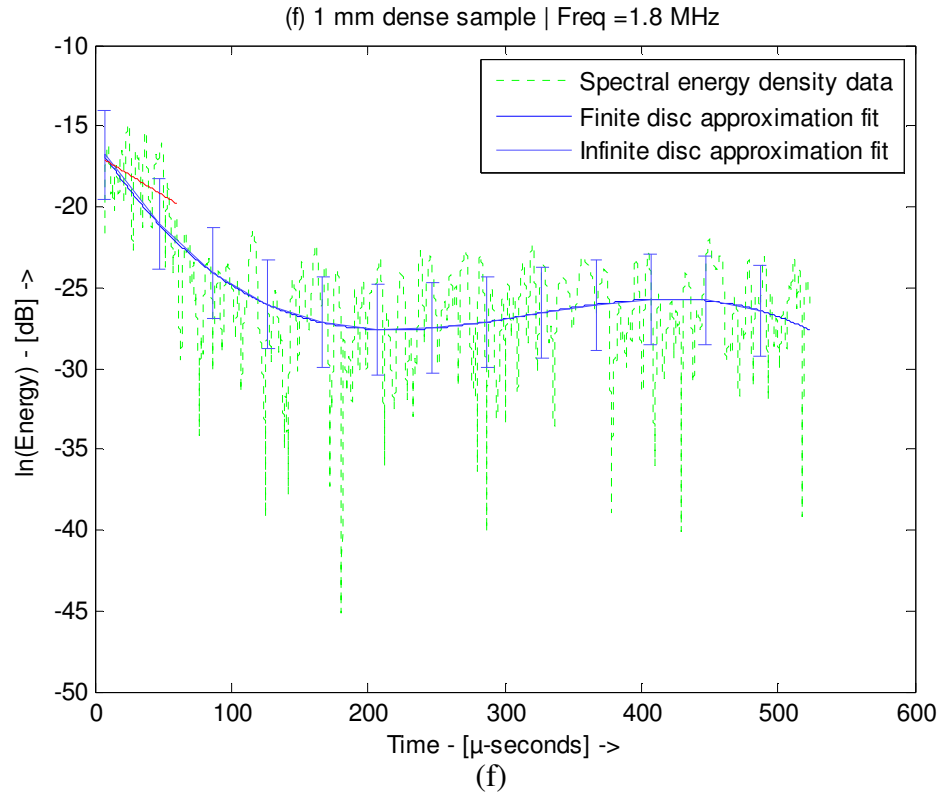


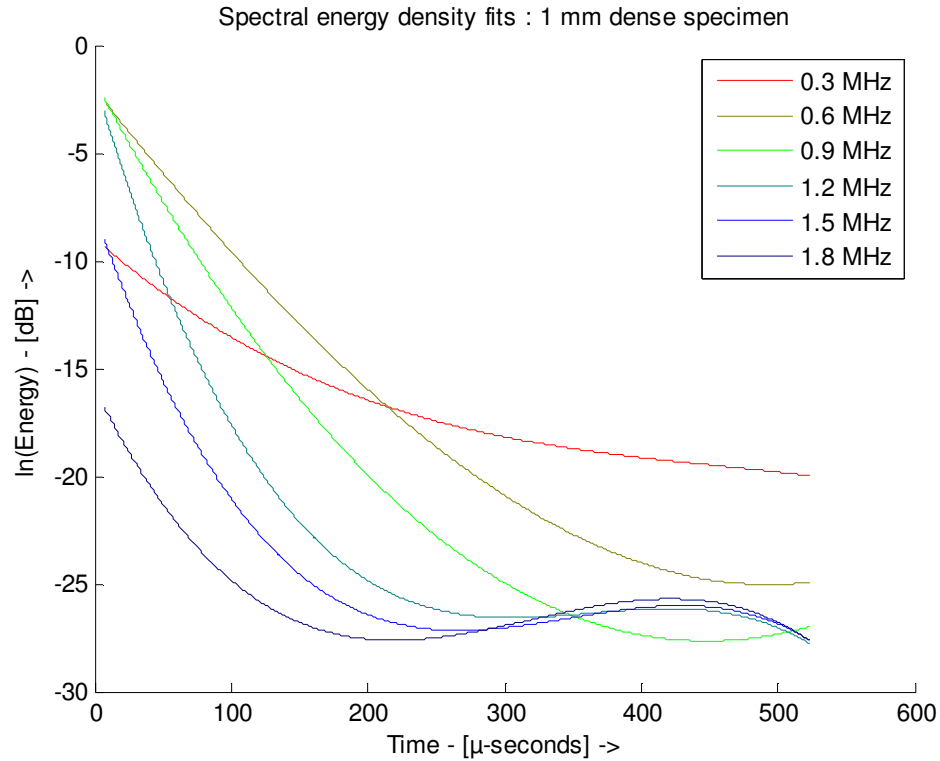
Figure 6.3 (a) to (f): Spectral energy density (green dots) and diffusion approximation fits using finite (blue line) and infinite (red line) disc approximations for 1mm dense specimen at various frequencies.







It is to be noted here that a quadratic fit could have been sufficient for this purpose, however the spectral energy density does show an expected rise and fall at extended time periods and a cubic fit is more adept at modeling the same. For this reasons, a cubic fit is chosen to model the spectral energy density evolution data. One of the assumptions used in this process is that a cubic fit is sufficient approximation for the solution for finite plate (equation 4.12). The solution to the diffusion equation along the radius of the disc follows a Bessel function, and in this research the solution is modeled to a maximum of the third root of $J_1(\alpha r) = 0$, which can be sufficiently approximated by the cubic-spline, thus validating our assumption. Typical example of fits for 1mm dense specimen along with confidence bands at various frequencies is shown in figure 6.3.



Summary of diffusion approximation fits for finite disc approximation

Figure 6.4: Summary of diffusion approximation fits with finite disc approximation for 1mm dense specimen

6.3 Observations

This objective of this thesis is to study the relationship between the residual spectral energy density and specimen geometry. As evident from the theoretical plots shown in section 4.3.4, the finite size of the discs used in the experiment creates a finite containment for the initial energy input. Thus, theoretically, after a steady dissipation rate in the beginning the decay should slow down and approach a steady value. While the data acquired through experiments is sufficient to validate this effect – unfortunately, however, the range of available specimen geometries is not sufficient to establish a

relationship between the two. Indicative trends listed in the sections below could be arenas for future research in establishing such trends and relationships.

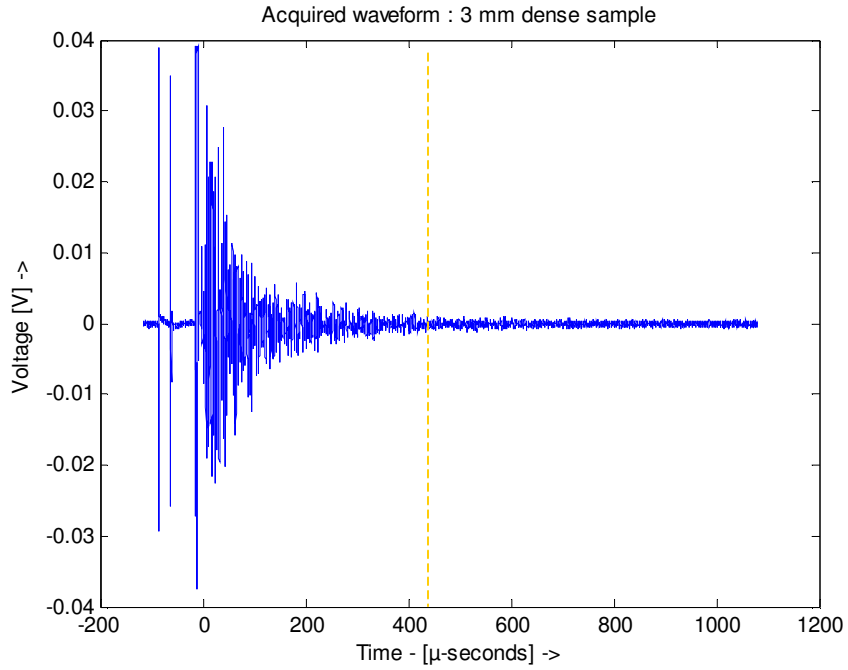
6.3.1 Model quality and comparison of fits

Listed below are few observations based on the curve-fitting process on the spectral energy density data.

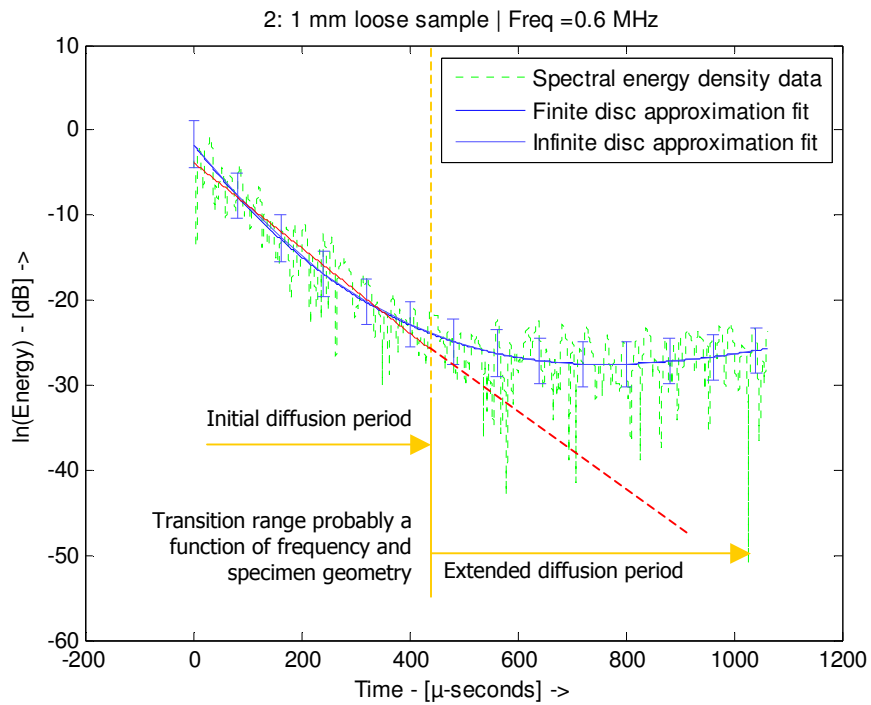
1. A close look at the fitted data shows the existence of an initial dissipation period. The dissipation coefficient here is log-linear with time and the fit agrees to a large extent with results from Becker et al [2]. This is likely the period when the energy is still continuing to diffuse in the disc, and the effect of geometry is unnoticed. The rate of dissipation is faster at higher frequencies.
2. After the initial diffusion period, the fitted curve approaches a slower decay or steady-state value, in good agreement to the hypothesis proposed in section 4.3.4. However, as opposed to frequency dependence as in point 1 above, the rate of diffusion seems to lie in very close range for the different frequency values. The residual energy lies within a short range of value for every specimen, and seems to be independent of the frequency considered.
3. Based on observations in point 1 and 2, there seems to be two distinct phases for the diffusion process in a finite disc. (1) The initial diffusion period (IDP), where the effect of specimen boundary can be neglected, and (2) the extended diffusion period (EDP), where the specimen boundary limits energy propagation outside the specimen, and contains the energy inside the boundary. It is during the IDP that Becker et al's plots agree with this research. However, as evident from figure 6.5

(a), this is not the case during the EDP and there is considerable and increasing difference between Becker et al and this research.

4. The transition point from IDP to EDP is rather fuzzy and can be noticed from the change in the slope of the fit, as in figure 6.5 (b). In this research, to mark the end of Becker et al's fit, an automated slope threshold based algorithm is used which terminates log-linear fit for the data when the slope reaches a specific limit. This seems to work quite well for the dataset considered.
5. Plots also show that curve-fit for $f_c = 0.3$ MHz behaves quite differently compared to the rest of the fits. The dissipation rate is significantly and consistently lower for a ± 150 kHz band around 300 kHz, and rather intuitive – since dissipation rates are lower and lower frequencies.
6. The plots also show initial minima in the spectral energy density values, followed by maxima, in agreement with that theoretical Bessel function solution for the diffusion equation for a circular disc with finite radius and height. We hypothesize that the initial minima might be directly correlated to the dissipation rates, while the time period between minima and following maxima might be related to the specimen geometry or volume. While we do find the minima to be related to the dissipation rates, due to the small range of specimen thickness and volume, we are unable to confirm our hypothesis for the maxima.



(a)



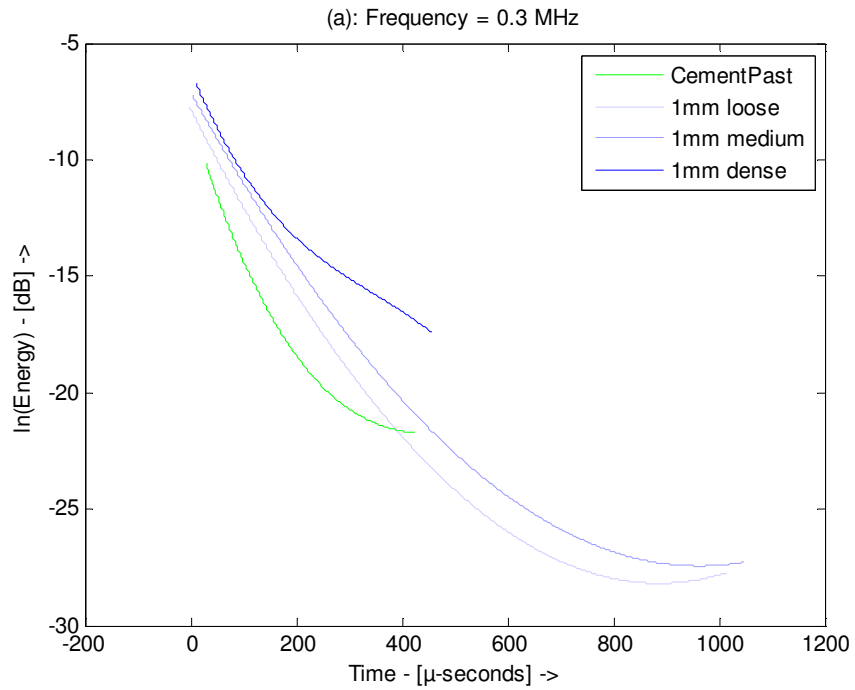
(b)

Figure 6.5: (a) Initial and extended diffusion periods schematically shown on waveform with (b) associated spectral energy density fit showing change in slope during transition

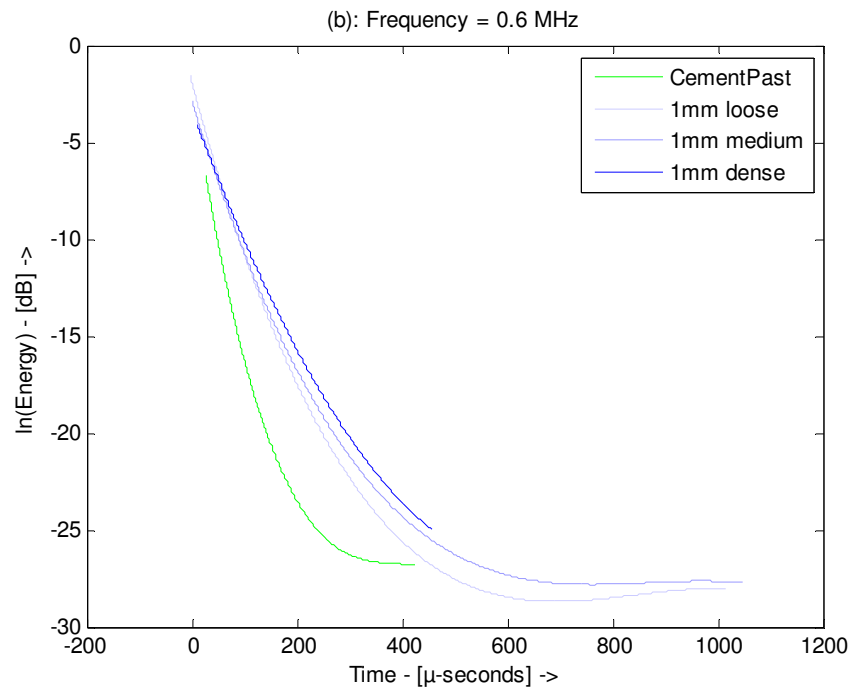
6.3.2 Specimen averaged models

The multiple waveforms and fits that are generated from the data are also averaged for every specimen type. Although this averaging should have been ideally performed in the time domain of the waveforms, the difficulty in properly registering the waveforms with each other could have caused sufficient errors in the process. Thus this averaging is done in the time-domain of the regressed log-energy signal, which is already segmented into six frequency bands. This helps to compare properties of the fit in relation to the specimen damage level or geometry. Few observations from this fit shown in the plots in figure 6.6 are listed below.

1. It is known that the cement paste has the least amount of damage (Table 5.1), followed by 1 mm loose, medium, and dense; and 3 mm loose and dense. The specimens show slower average dissipation rates for higher damage accumulation, which also agrees to observation by Becker et al in [2]. However this difference is more evident at 0.6 MHz-0.9 MHz range, than at 1.2 MHz and beyond.
2. 3 mm loose and dense specimens, however, does not conform well to the trend observed in 1 above.
3. Over the averaged data, the first minima of the energy seem to have a direct correlation with the dissipation rates. However, we as mentioned in section 5.3.1 point 6, the time period Δt_{Bessel} , between first minima and following maxima, might be correlated to the specimen geometry or volume, and is hard to tell from the range of the specimen geometries considered in this research.
4. It is also noticed that time period, Δt_{Bessel} is shorter at higher frequencies for all the specimens, probably due to faster diffusion rates at such frequencies.

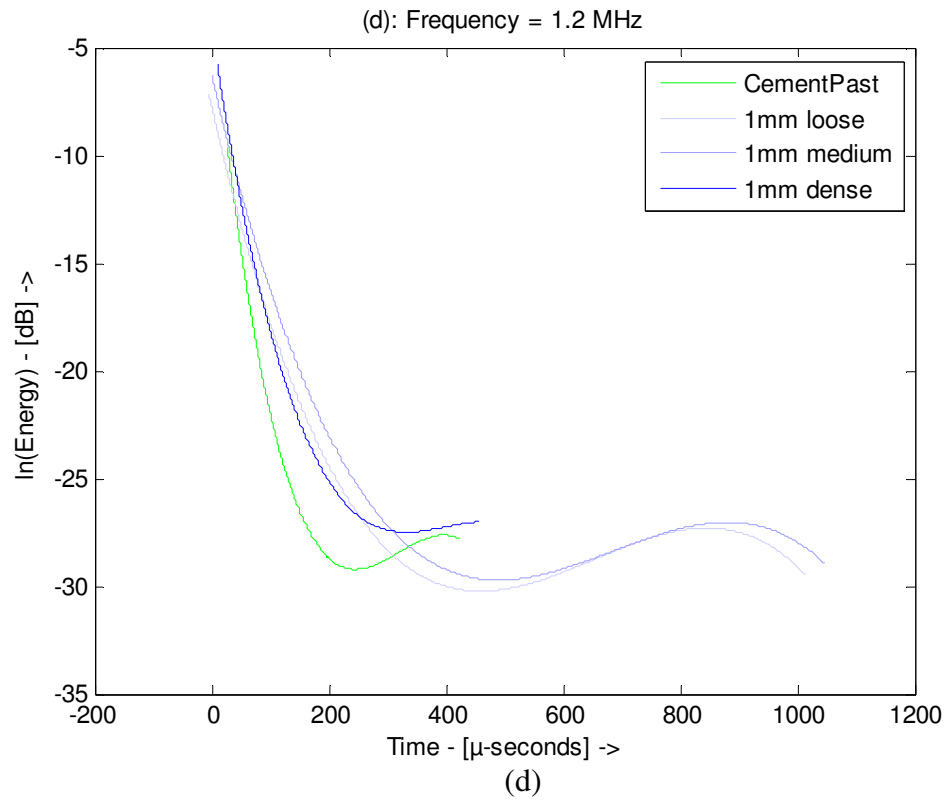
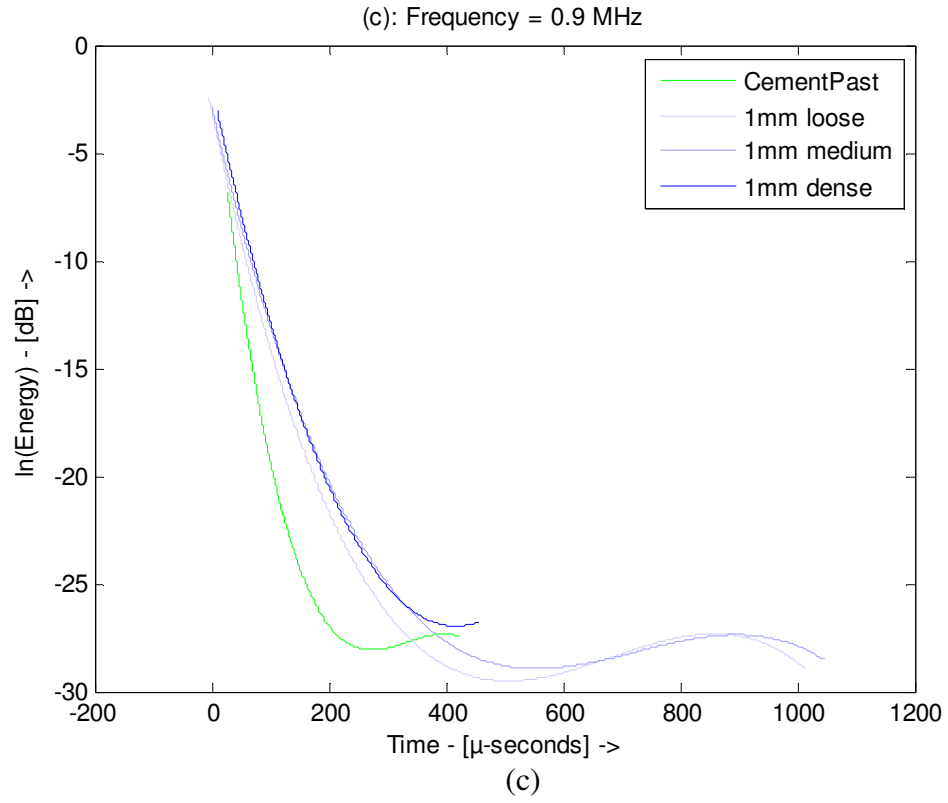


(a)

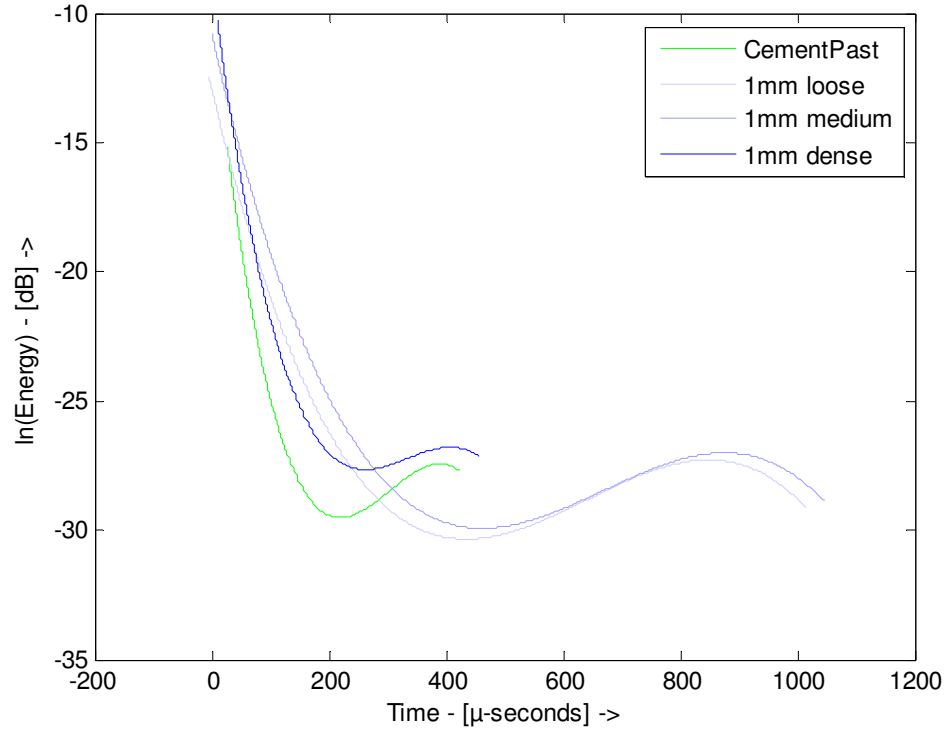


(b)

Figure 6.6: Plots showing comparative dissipation curve fits for specimens with different levels of damage. Plots (a) to (f) are for cement paste and 1 mm bead specimens. Plots (g) to (l) are for cement paste and 3 mm bead specimens. Plots (m) to (r) are for cement paste, 1mm and 3mm bead specimens shown together.

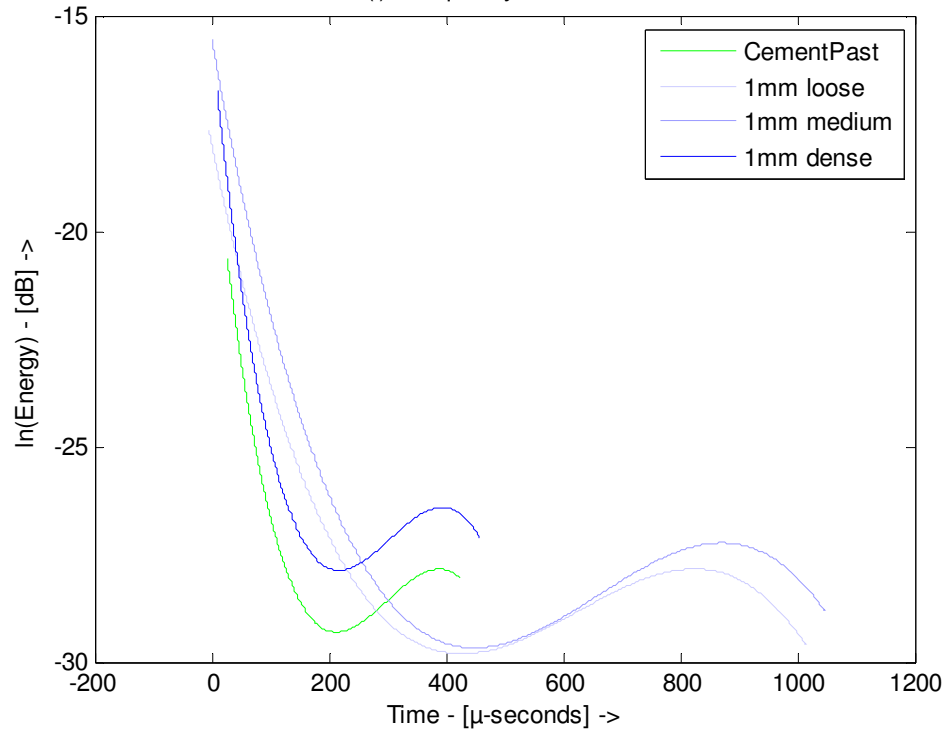


(e): Frequency = 1.5 MHz

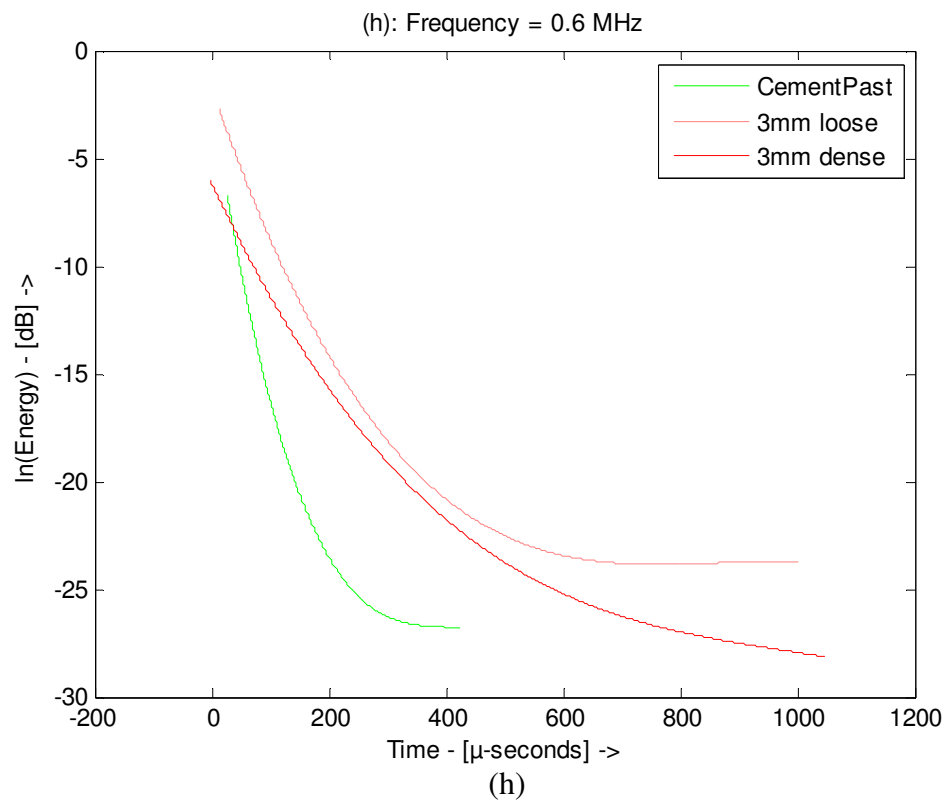
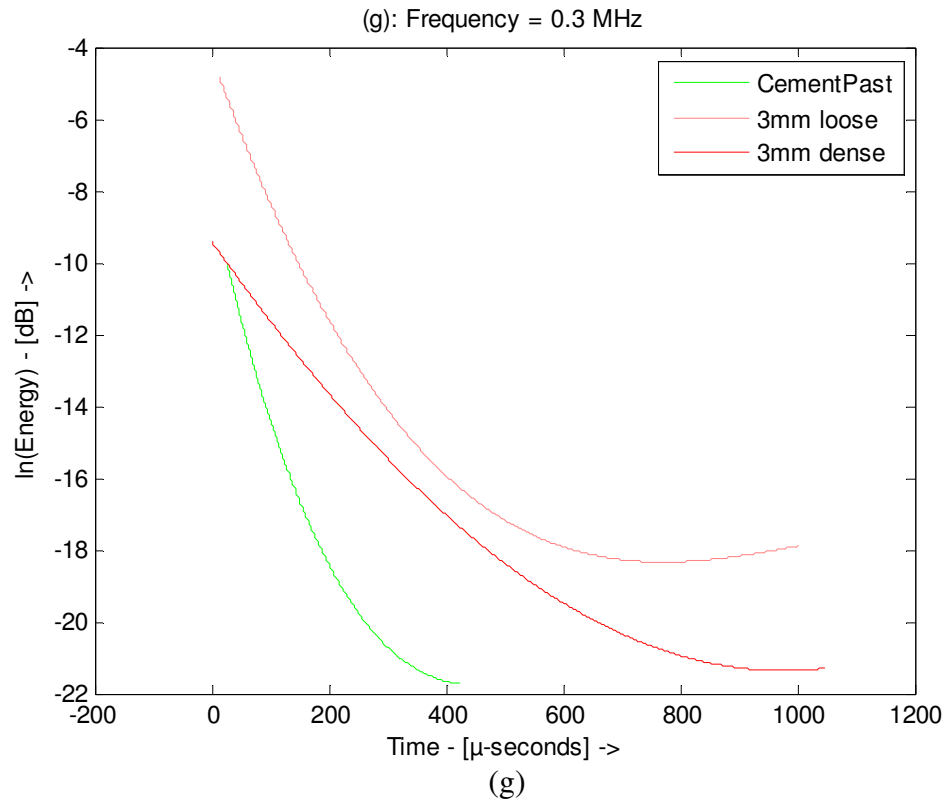


(e)

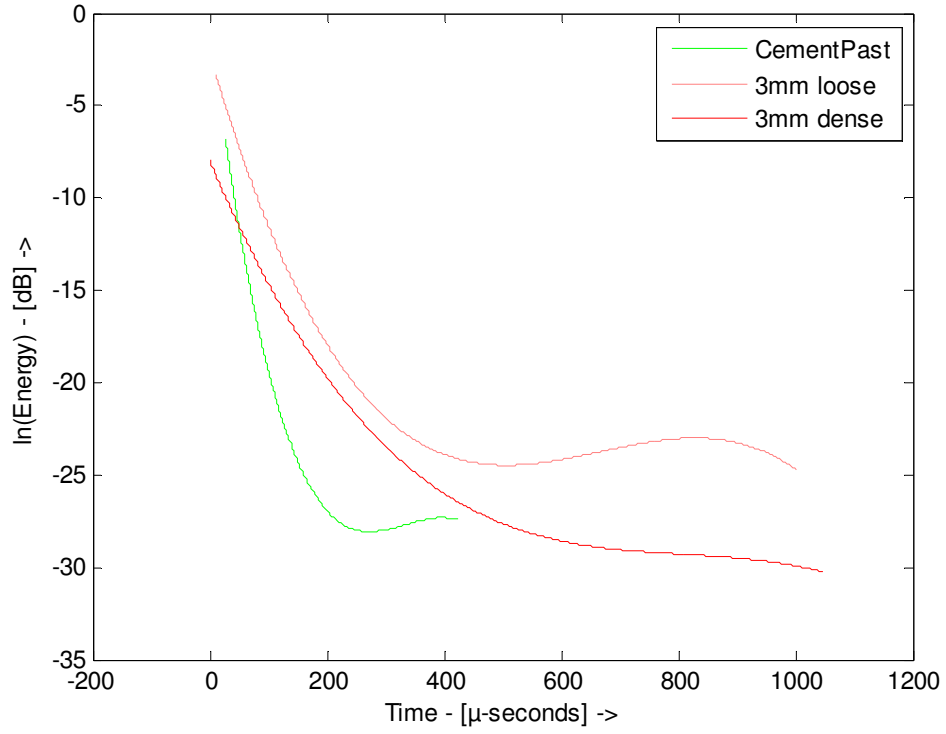
(f): Frequency = 1.8 MHz



(f)

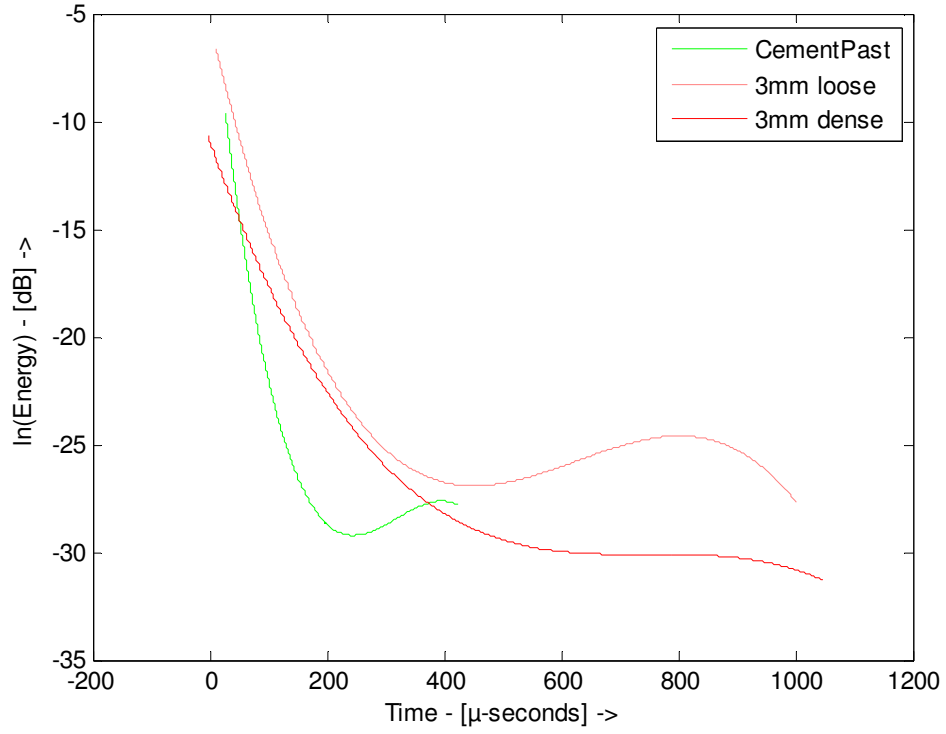


(i): Frequency = 0.9 MHz

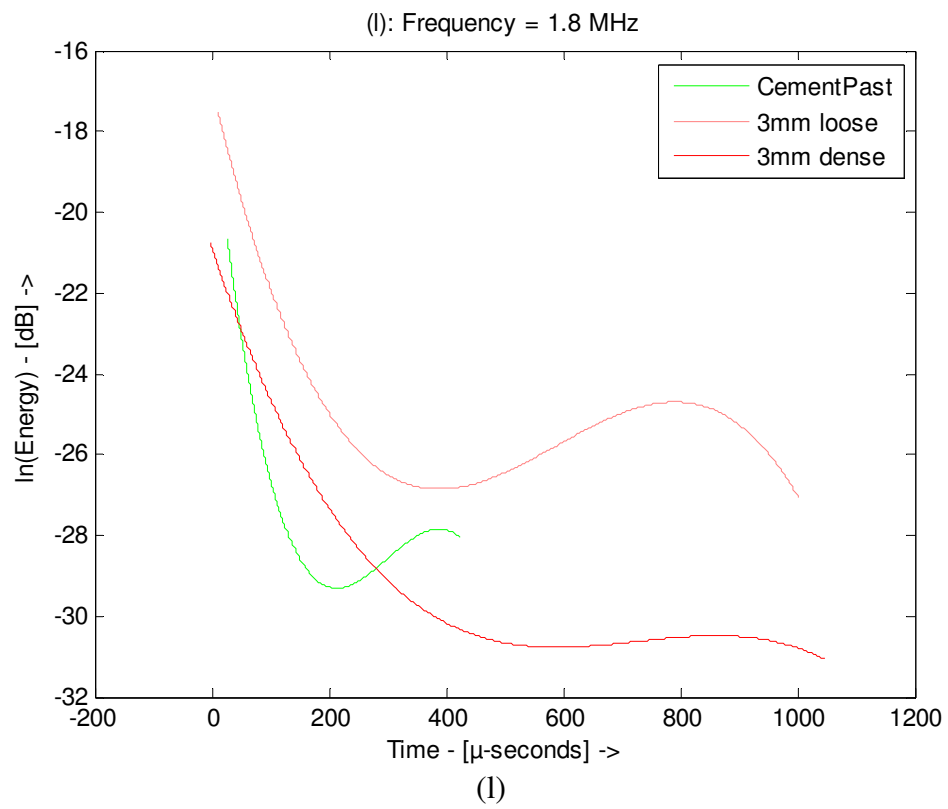
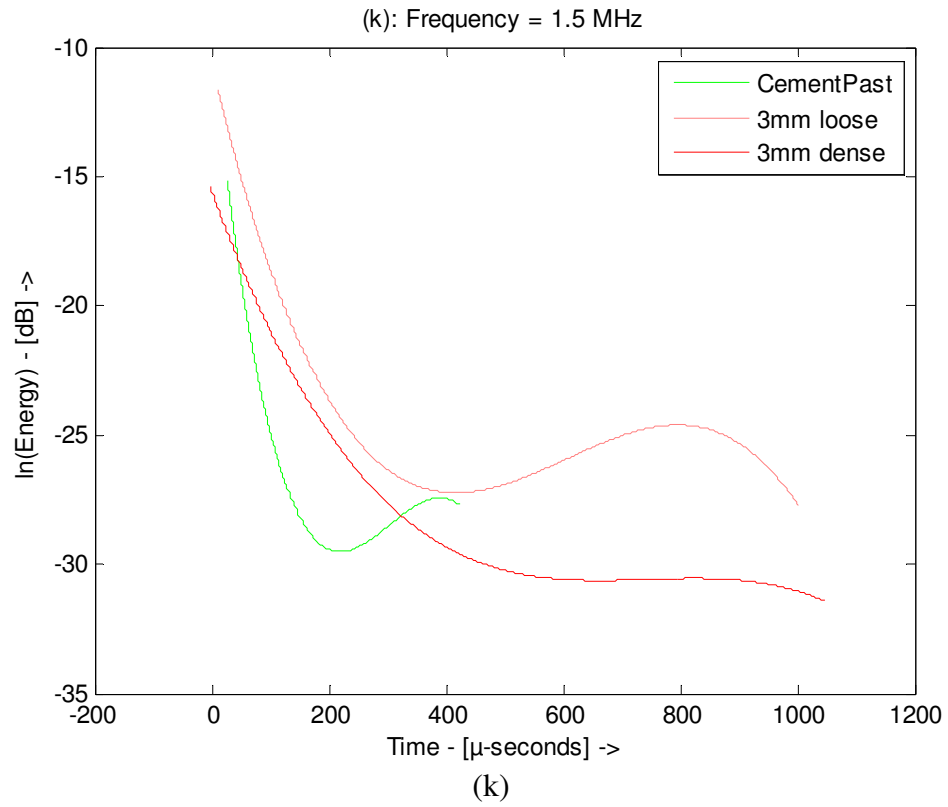


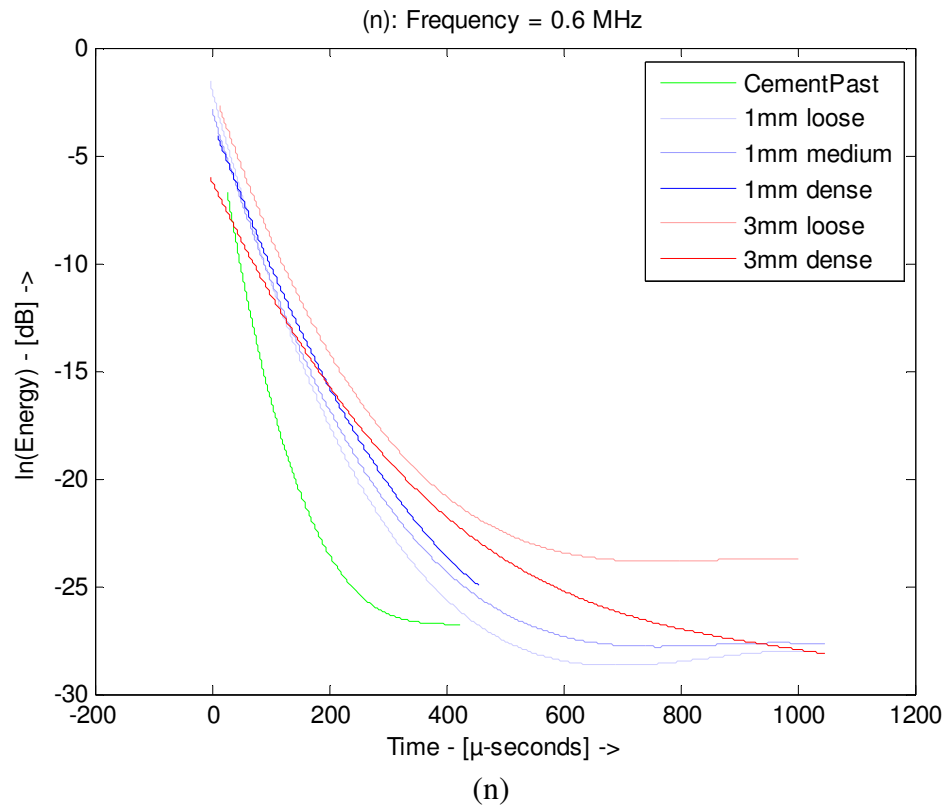
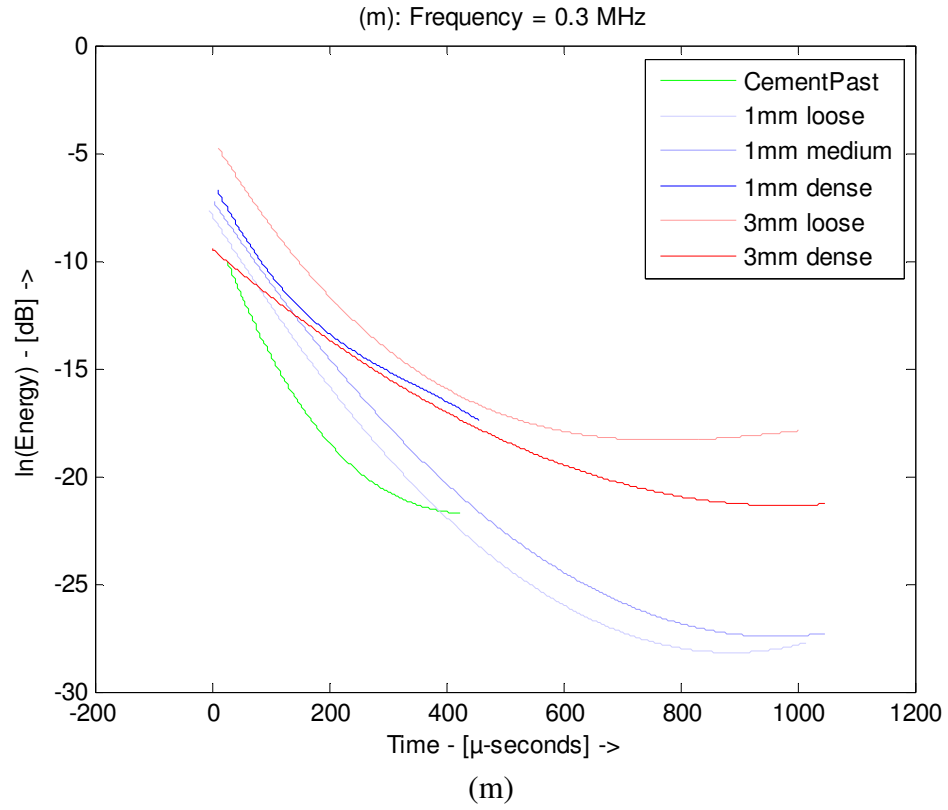
(i)

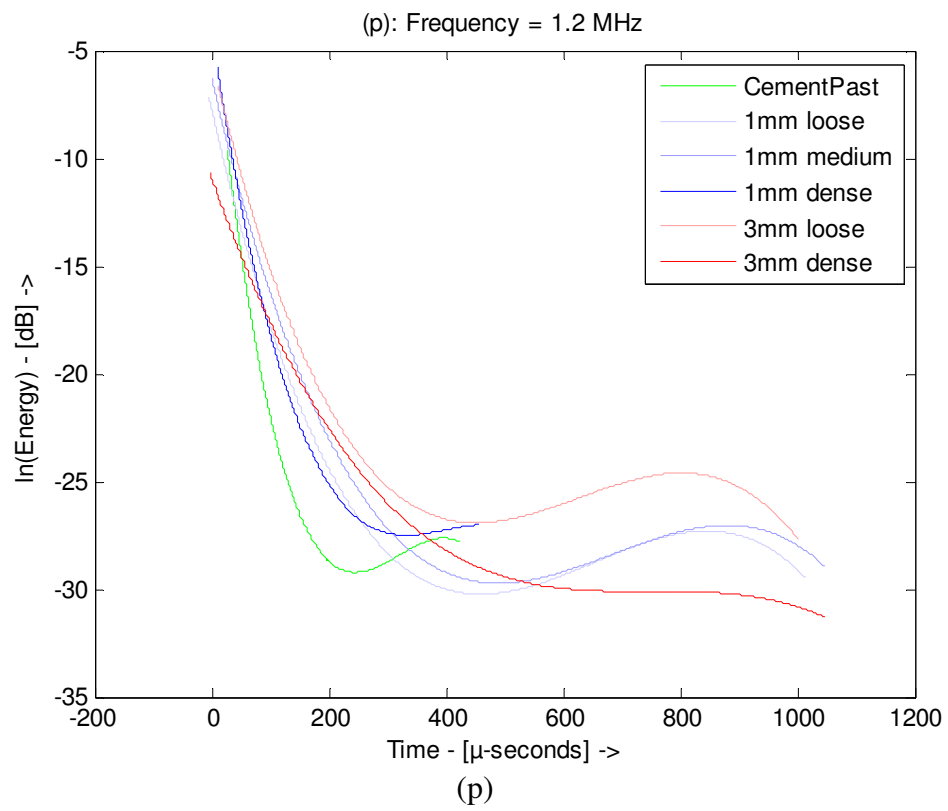
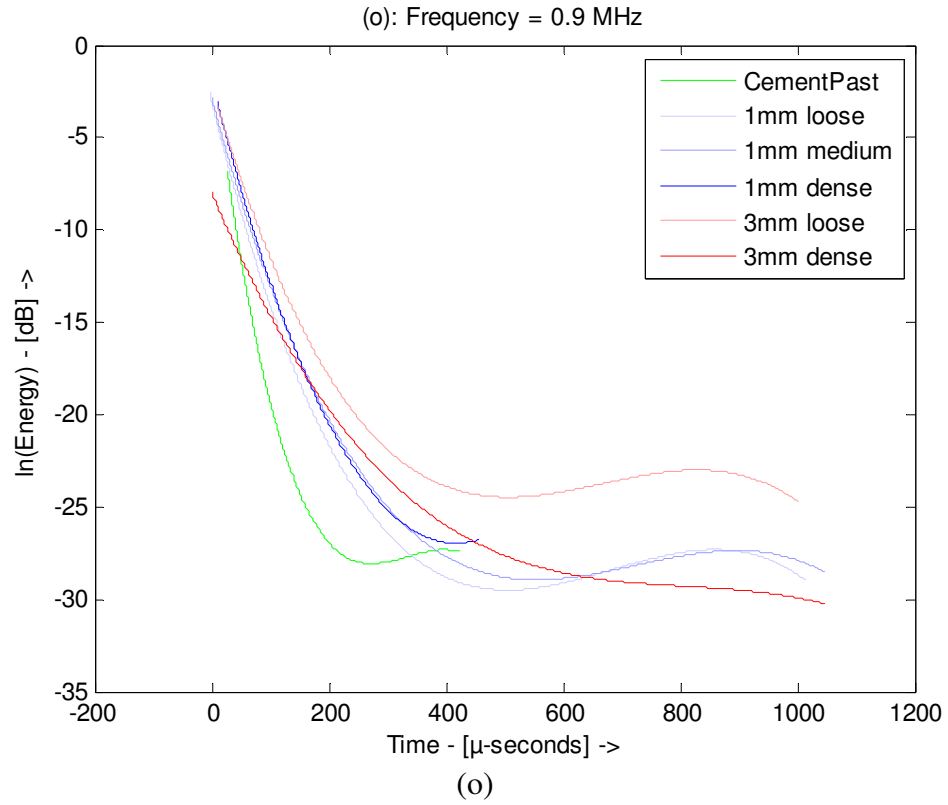
(j): Frequency = 1.2 MHz



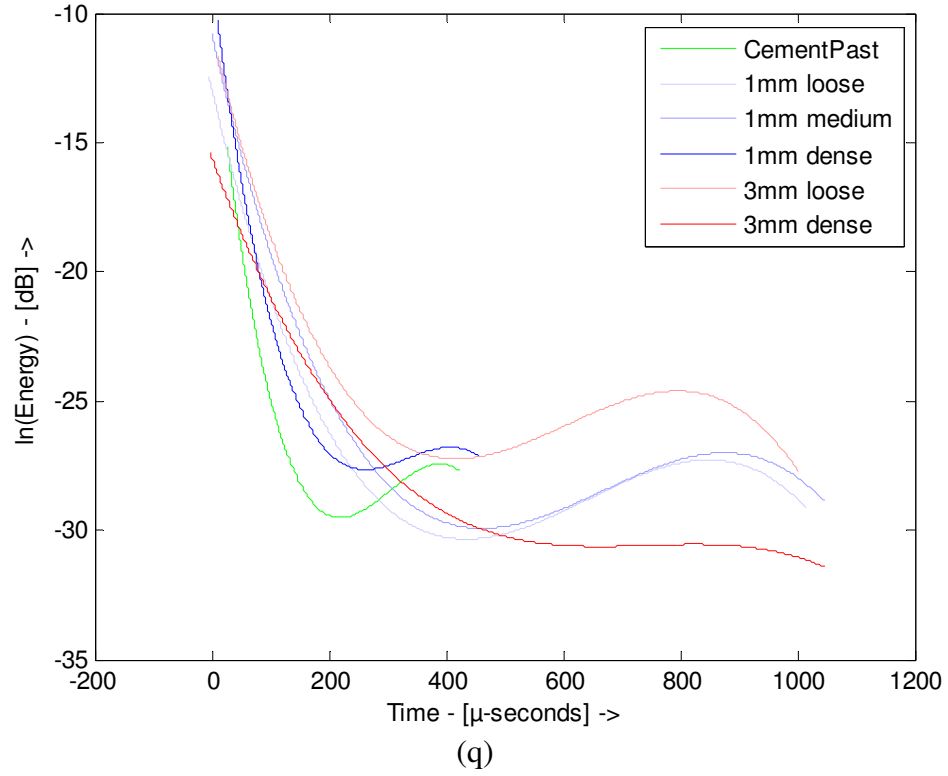
(j)



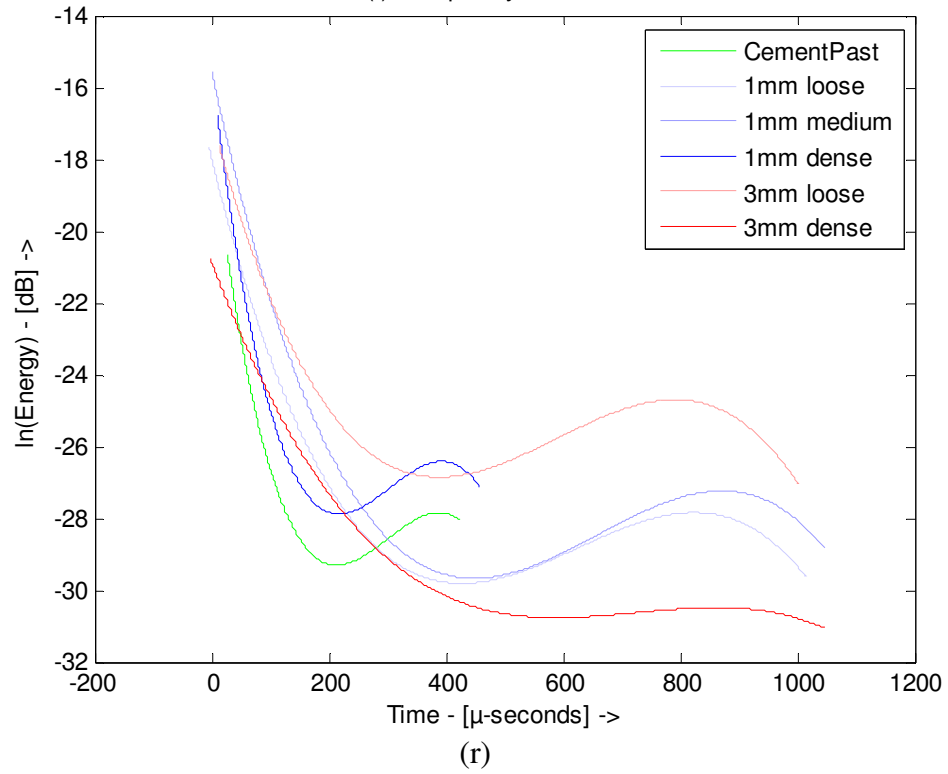




(q): Frequency = 1.5 MHz



(r): Frequency = 1.8 MHz



6.3.3 Geometry and material trends

The average values of derived parameters from the spectral energy density curves are correlated to specimen geometry and damage levels. Observations on the variation of these parameters with specimen geometry and aggregate properties are summarized in the following points. It is also observed that the dissipation rate at 0.3 MHz is much lower than at higher frequencies, and would largely dominate the any trend based observations, since the rest of the curves seem to converge to a narrow band of energy. An example of this effect can be seen in figure 6.8 (1 mm loose specimen).

1. Figure 6.9 shows the variation of average minimum energy, $\overline{E(f)_{\min}}$, with specimen thickness. $\overline{E(f)_{\min}}$ is the average of the first energy minima values at the various frequencies. It is observed that $\overline{E(f)_{\min}}$ shows a negative correlation with specimen thickness, or volume (since the radius is same for all specimens). This agrees with theory, since average residual energy should decrease with increasing thickness or volume – energy gets distributed into a larger space. It is interesting to note that $\overline{E(f)_{\min}}$ shows a rather strong correlation in the short range of specimen thickness.
2. Figure 6.10 shows the extent of time required by the specimens to reach the energy minima. This duration shows positive correlation with volume fraction of the aggregates, probably due to decreased diffusion rates. More number of aggregated create more phase boundaries, thereby slowing down the diffusion process.

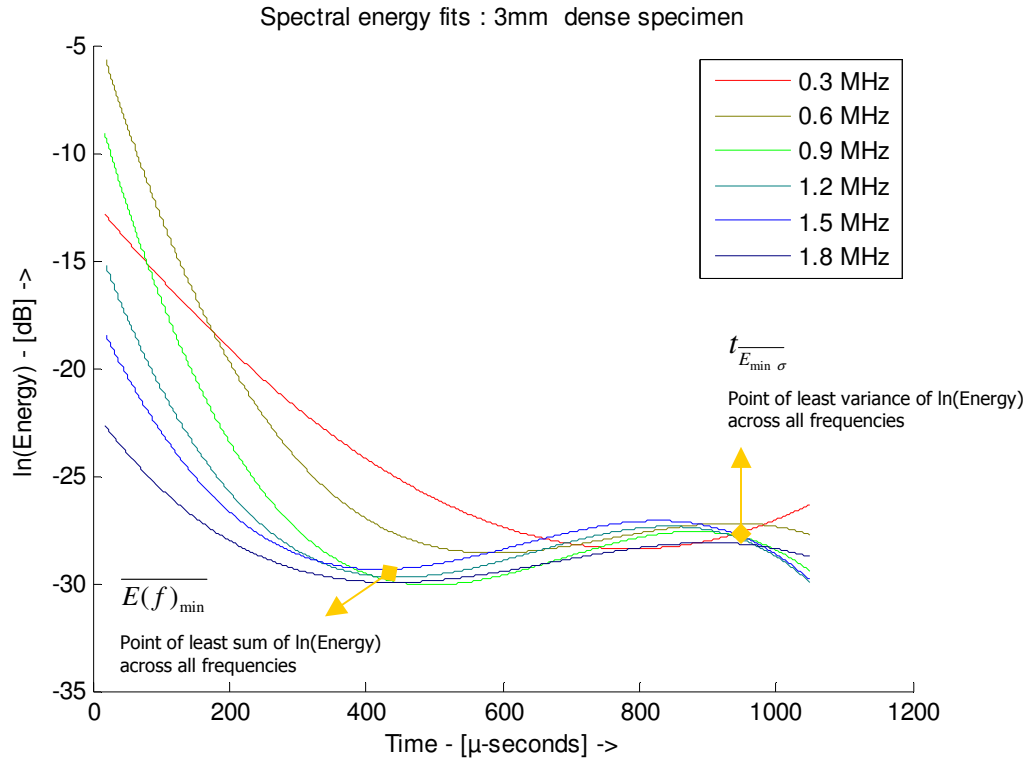


Figure 6.7: 3mm dense plot graphically depicting $t_{E_{min} \sigma}$

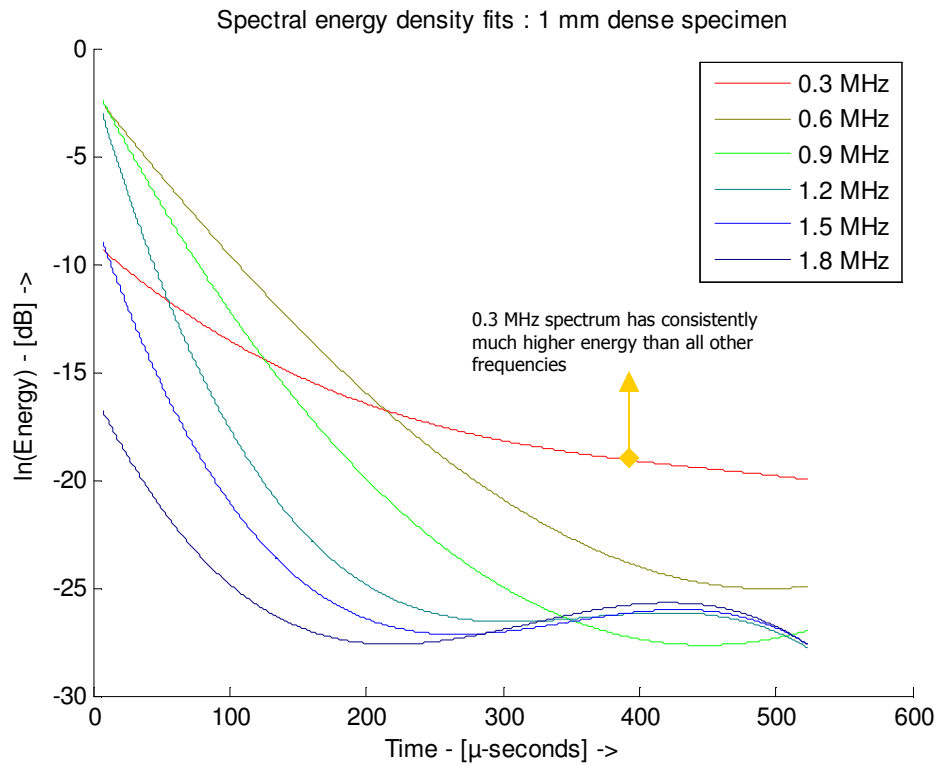


Figure 6.8: 1mm dense plot showing similarity in behavior

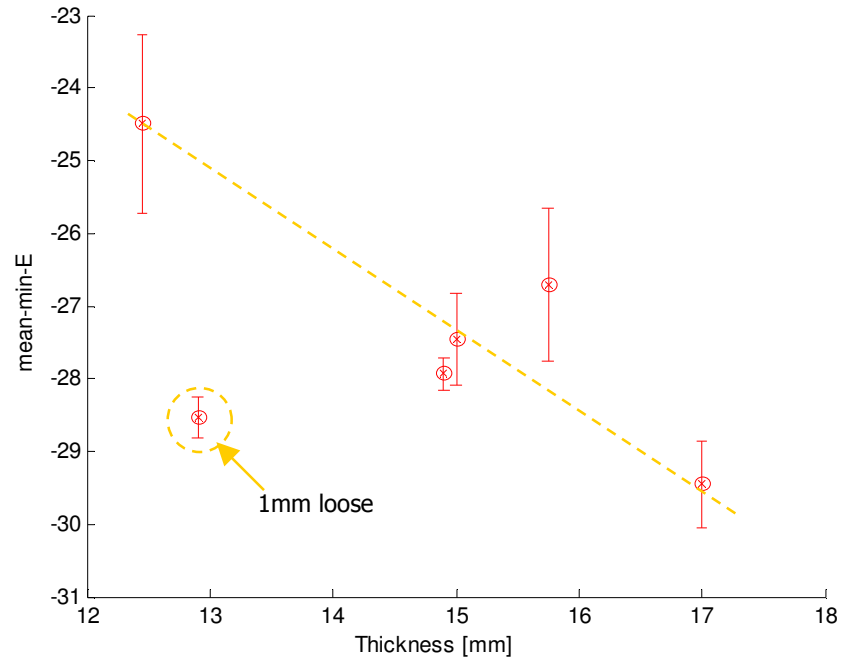


Figure 6.9: Plot showing variation of $\overline{E(f)_{\min}}$ with specimen thickness

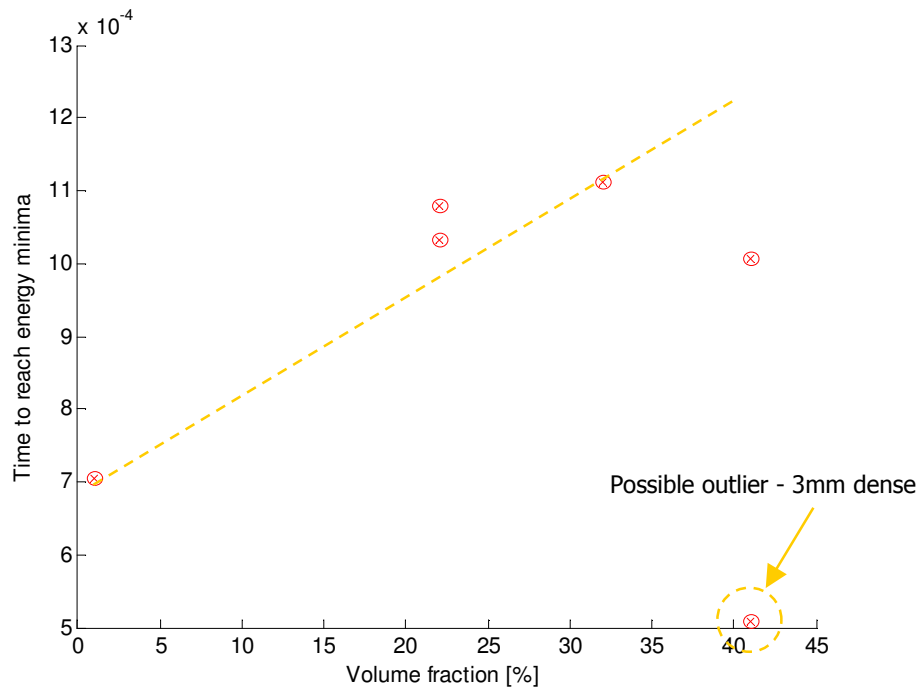


Figure 6.10: Plot showing time to reach energy minima against volume fraction

6.4 Summary

It is clearly seen from the plots and observations in this chapter that the spectral energy density evolution with time agrees with the theory and hypothesis discussed in section 4.3.4 and 4.3.5. The energy shows distinct phases for the diffusion process in a finite disc, *viz.*, an initial diffusion period, where the effect of specimen boundary can be neglected, and an extended diffusion period, where the specimen boundary limits energy propagation outside the specimen, and contains the energy inside the boundary at a steady level. Further, the first minima of the spectral energy density show positive correlation with the dissipation rate, but it is difficult to find the same for the following maxima and its hypothesized relation to the specimen geometry. Finally, though the proposed model in this research is a better fit to the entire duration of waveform acquisition, as compared to Becker et al [2], and accounts for the geometry of the specimens – it does not seem to provide any extra information on the damage condition of the specimens. However, it needs to be seen if the minima or residual energy level measurement provide a substantial benefit over slope measurements, which can be complicated, and thus cumbersome in field inspections.

CHAPTER 7

CONCLUSIONS AND OUTLOOK

This research looks at the process of ultrasound diffusion in cement-based aggregates to better model the dissipation of energy inside the material, and also understands the effects of specimen geometry on the energy decay mechanism. Following the literature, a new and more accurate solution to the diffusion equation is proposed, and the model predicts that the energy decay process is severely affected by the finite geometry of the specimens under consideration. As shown by Becker et al [2, 3], an infinite disc model for the diffusion equation can be used to predict dissipation in finite disc only for an initial time period where the effect of geometry is relatively unperceived by the propagating diffusion front. Beyond that, as shown in this research, the energy decay process slows down and remains almost steady for an infinitely long period of time. While in theory the boundary of the discs in question are considered to be perfectly adiabatic, in reality slow leakage would gradually bring down the energy content within the disc to zero. Experimental data acquired for specimens with slightly different thicknesses, and relatively varied aggregate content are used to practically evaluate and test the hypothesis. It is found that the energy dissipation from experimental data very well follows the Bessel curve, which is a solution to the diffusion equation for finite disc. Experimental data is observed to have fewer than three minima-maxima points, and a cubic spline is fit to the spectral energy density data as an approximation of the more complicated Bessel function in the given time period.

Results from the experiment concur well with the hypothesis described in section 4.3.4. Detailed analysis of the experimental results, as given section 6.2 show curve fits to the acquired data that extends and explains the behavior of the dissipation process well beyond the limit in [2]. It is also seen that regardless of the high dissipation rate at higher frequencies, the model is able to predict the behavior even in the extended diffusion period. A comparison of the spectral energy density curves across the various specimens clearly show the influence of the specimen damage condition on the diffusion rates, and well agrees with [2].

The model used in this research could be expanded upon further in future work to estimate the diffusion and dissipation coefficients, accounting for the finite specimen geometries. This more accurate model would better predict the behavior of the ultrasound energy inside the specimen under investigation, thereby helping better accounting for any difference to specimen material condition. The limited types of specimens in this research could also be overcome through specimens with varying thicknesses as well as diameters. This would provide a more concrete evaluation for a wider range of parameters.

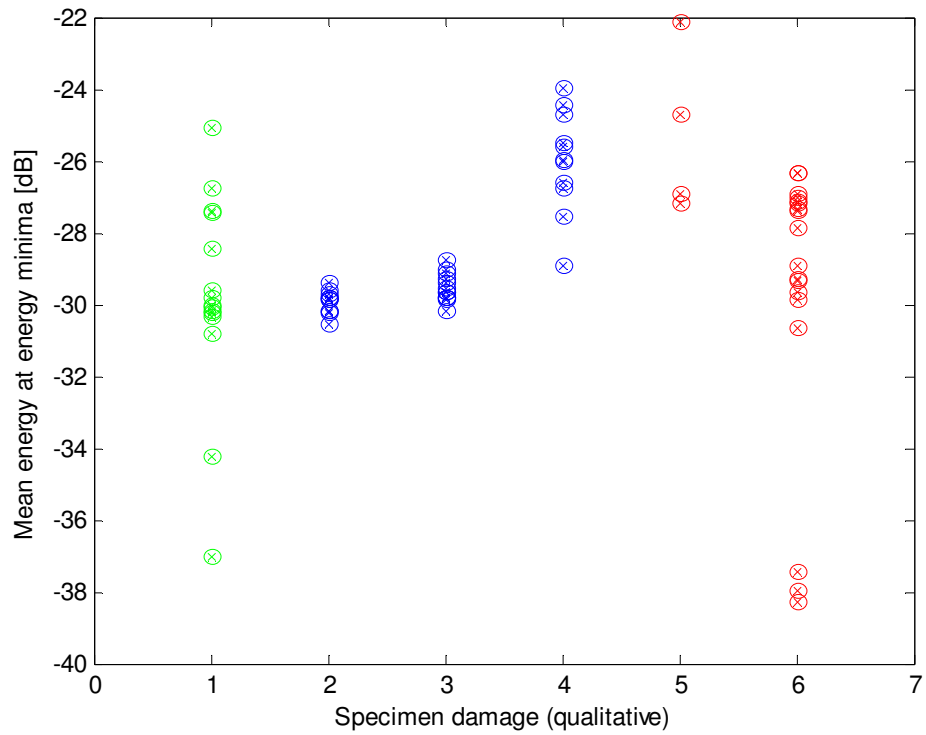


Figure 7.3: Scatter plot showing energy value at lowest variation zone

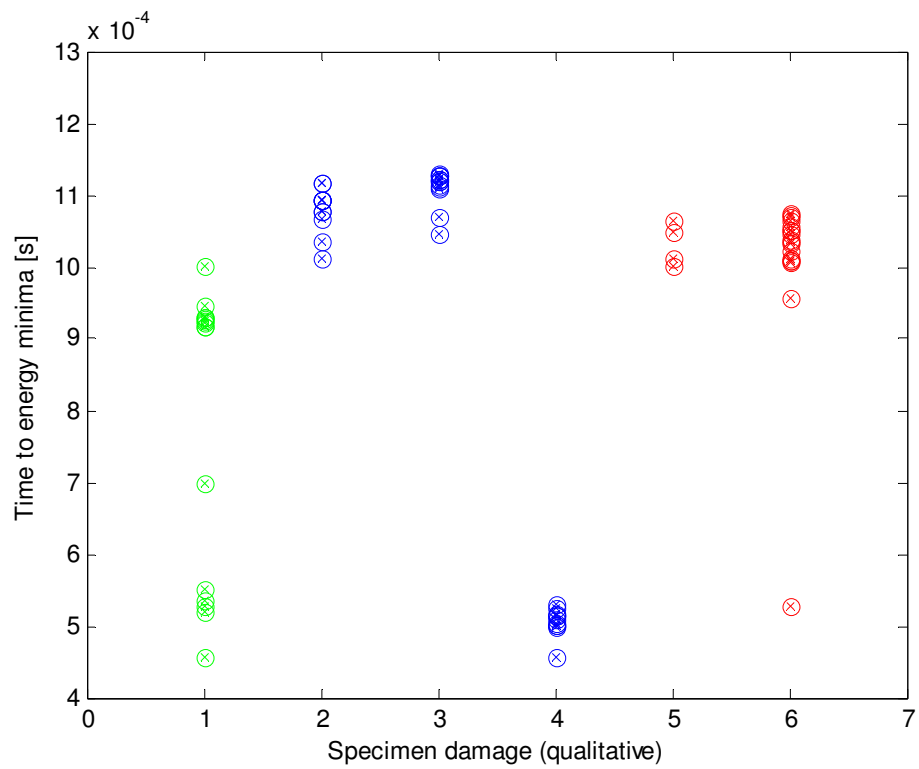


Figure 7.4: Scatter plot showing time to reach energy point to tightest scatter

In this research few observations are made on the average trends of dissipation curve properties against specimen geometry. These trends seem to have some variations, and a wider range of specimen properties could help make more definitive observations. Figure 7.1 to 7.4 show scatter plots of few dissipation curve properties, already discussed section 6.3.3. Different specimens are shown in green, blue and red, indicating different damage accumulation (green – good, cement paste; blue – medium, 1mm glass beads; red – bad, 3mm glass beads) for better visual understanding of the scatter and implicit trends, if any. Future research could be aimed at refining the scatter through tighter control of the input conditions and specimen material properties. Also, understanding second order input and output parameter combinations, such as specific spectral energy density, etc could lead to useful measures of damage accumulation.

In summary, this research and any future research in similar direction is going to greatly benefit the inspection of cement-based infrastructures. Since diffusion provides an average volume measure of the object or structure under investigation, relating the diffusion parameters to damage condition could lead to faster and reliable inspection methods. Insitu or embedded probes and sensors could further advance this method to someday provide continuous and reliable measure of damage level, providing triggers for maintenance and repair, and fully avoid any catastrophic failures or serious consequences.

REFERENCES

1. H. S. Carslaw, J.C.J., *Conduction of Heat in Solids*. 2nd ed ed. 1986: Oxford University Press, USA. 520
2. Becker, J., L.J. Jacobs, and J. Qu, *Characterization of cement-based materials using diffuse ultrasound*. Journal of Engineering Mechanics, 2003. **129**(12): p. 1478-1484.
3. Becker, J., *Investigation of the Microstructure of Heterogeneous Materials using Ultrasonic Waves*, in *School of Civil and Environmental Engineering*. 2002, Georgia Institute of Technology: Atlanta, GA, USA.
4. Mobley, R.K., *An Introduction to Predictive Maintenance*. Materials & Mechanical. 2002: Elsevier Butterworth-Heinemann. 1-437.
5. McIntire, P. and D. Ensminger, *Nondestructive testing handbook, vol 7*. Applied Mechanics Reviews, 1991. **44**(11 pt 1): p. 182.
6. Smith, E.H., *Mechanical Engineers Reference Book*. 12th ed ed. 1998: Butterworth-Heinemann. 1248.
7. AMMTIAC, *TechSolutions: Nondestructive Testing*. AMMTIAC Quarterly, 2006. **1**(2).
8. Ergun, A.S., et al. *Fabrication and characterization of 1-dimensional and 2-dimensional Capacitive Micromachined Ultrasonic Transducer (CMUT) arrays for 2-dimensional and volumetric ultrasonic imaging*. 2002. Biloxi, MI, USA: IEEE.
9. Yorkston, J., *Recent developments in digital radiography detectors*. Nuclear Instruments and Methods in Physics Research, Section A: Accelerators, Spectrometers, Detectors and Associated Equipment, 2007. **580**(2): p. 974-985.
10. Anastasi, R.F., et al. *Terahertz NDE application for corrosion detection and evaluation under shuttle tiles*. 2007. San Diego, CA, United States: SPIE, Bellingham WA, WA 98227-0010, United States.
11. Salvade, A., et al. *A numerical evaluation of an optimal setup for a microwave axial tomograph aimed at the inspection of wood*. 2007. Krakow, Poland: IEEE.
12. Yan, Z.-K., H.-J. Zhang, and Y.-B. Ying, *Research progress of terahertz wave technology in quality measurement of food and agricultural products*. Guang Pu Xue Yu Guang Pu Fen Xi/Spectroscopy and Spectral Analysis, 2007. **27**(11): p. 2228-2234.
13. Liu, Z., et al., *Survey: State of the art in NDE data fusion techniques*. IEEE Transactions on Instrumentation and Measurement, 2007. **56**(6): p. 2435-2451.
14. Johnston, H., *Basic application of ultrasonic inspection in industry*. Industrial Heating, 2007. **74**(8): p. 85-8.
15. Hak-Joon, K., L.W. Schmerr, Jr., and A. Sedov. *Transferring distance-amplitude correction curves using ultrasonic modeling*. 2004. Green Bay, WI, USA: AIP.
16. Jacobs, L.J., et al., *Characterization of dissipation losses in cement paste with diffuse ultrasound*. Mechanics Research Communications, 2007. **34**(3): p. 289-94.
17. Wikipedia.com. *I-35W Mississippi River bridge collapse*. August 1, 2007 [cited; Available from: http://en.wikipedia.org/wiki/I-35W_Mississippi_River_bridge.
18. Murtagh, F., et al., *Grading of construction aggregate through machine vision: Results and prospects*. Computers in Industry, 2005. **56**(8-9): p. 905-17.

19. Kozlov, V.N., V.G. Shevaldykin, and N.N. Yakovlev, *Experimental determination of the attenuation of an ultrasonic wave in concrete*. Soviet Journal of Nondestructive Testing (English translation of Defektoskopiya), 1988: p. 132-140.
20. Pollakowski, M. and H. Ermert, *Chirp signal matching and signal power optimization in pulse-echo mode ultrasonic nondestructive testing*. IEEE Transactions on Ultrasonics, Ferroelectrics and Frequency Control, 1994. **41**(5): p. 655-9.
21. Schickert, M., M. Krause, and W. Muller, *Ultrasonic imaging of concrete elements using reconstruction by synthetic aperture focusing technique*. Journal of Materials in Civil Engineering, 2003. **15**(3): p. 235-246.
22. Maierhofer, C., et al., *Complementary application of radar, impact-echo, and ultrasonics for testing concrete structures and metallic tendon ducts*. Transportation Research Record, 2004(1892): p. 170-177.
23. Popovics, S., et al., *High-frequency ultrasound technique for testing concrete*. ACI Materials Journal, 2000. **97**(1): p. 58-65.
24. Selleck, S.F., et al., *Ultrasonic investigation of concrete with distributed damage*. ACI Materials Journal, 1998. **95**(1): p. 27-36.
25. Owino, J.O. and L.J. Jacobs, *Attenuation measurements in cement-based materials using laser ultrasonics*. Journal of Engineering Mechanics, 1999. **125**(6): p. 637-647.
26. Schubert, F. and B. Koehler. *Numerical time-domain simulation of diffusive ultrasound in concrete*. 2004. Granada, Spain: Elsevier.
27. Anugonda, P., J.S. Wiehn, and J.A. Turner, *Diffusion of ultrasound in concrete*. Ultrasonics, 2001. **39**(6): p. 429-35.
28. Philippidis, T.P. and D.G. Aggelis, *Experimental study of wave dispersion and attenuation in concrete*. Ultrasonics, 2005. **43**(7): p. 584-95.
29. Chaix, J.-F., V. Garnier, and G. Corneloup, *Ultrasonic wave propagation in heterogeneous solid media: Theoretical analysis and experimental validation*. Ultrasonics, 2006. **44**(2): p. 200-210.
30. J.D.Achenbach, *Wave propagation in elastic solids*. 1975: North-Holland.
31. K.F.Graff, *Wave motion in elastic solids*. 2975: Dover publications.
32. Cohen, L., *Time-frequency analysis*. 1995: Prentice Hall.
33. R.W.Schafer, A.V.O.a., *Discrete-time signal processing*. 1999: Prentice Hall.
34. L.Gaul, *The influence of damping on waves and vibrations*. Mechanical Systems and Signal Processing, 1999. **13**(1): p. 1-30.
35. Molyneux, J.B. and D.R. Schmitt, *Compressional-wave velocities in attenuating media: a laboratory physical model study*. Geophysics, 2000. **65**(4): p. 1162-1167.
36. Cowan, M.L., et al., *Group velocity of acoustic waves in strongly scattering media: Dependence on the volume fraction of scatterers*. Physical Review E (Statistical Physics, Plasmas, Fluids, and Related Interdisciplinary Topics), 1998. **58**(5): p. 6626-36.
37. Sheng, P., *Introduction to Wave Scattering, Localization and Mesoscopic Phenomena*. 2nd ed ed. Vol. 1. 2006: Springer. 333.

38. Weaver, R., *Ultrasonics in an aluminum foam*. Ultrasonics, 1998. **36**(1-5): p. 435-442.
39. Page, J.H., et al., *Classical wave propagation in strongly scattering media*. Physica A:, 1997. **241**(1-2): p. 64-71.
40. Page, J.H., et al., *Experimental test of the diffusion approximation for multiply scattered sound*. Physical Review E (Statistical Physics, Plasmas, Fluids, and Related Interdisciplinary Topics), 1995. **52**(3): p. 3106-14.
41. Schriemer, H.P., et al., *Energy velocity of diffusing waves in strongly scattering media*. Physical Review Letters, 1997. **79**(17): p. 3166-9.
42. Ultrasonics Laboratories Inc., *Ultrasonics Transducer Catalog*. 2002: 1020 E. Boal Avenue, Boalsburg, PA 16827 USA.
43. K.E.Kurtis, C.L.C., and P.J.M.Monteiro., *The surface chemistry of the alkali-silica reaction: A critical evaluation and x-ray microscopy*. RILEM Concrete Science and Engineering, special issue on Alkali-Aggregate Reaction, 2002.